

**Czech Technical University in Prague**  
**Faculty of Electrical Engineering**

# **Doctoral Thesis**

*February 2023*

*Salman Hasn*

Czech Technical University in Prague  
Faculty of Electrical Engineering  
Department of Microelectronics

# **Inspection of Complex Objects Utilizing Energy-Sensitive X-ray Imaging**

**Doctoral Thesis**

**Salman Hasn**

Prague, February 2023

Ph.D. Programme: P2612 Electrical Engineering and Information Technology  
Branch of Study: 2612V015 Electronics

**Supervisor:** Ing. Daniel Vavřík, Ph.D.

**Supervisor-Specialist:** Dr. rer. nat. Martin Peter Pichotka.

# Declaration

I declare that the work presented in this dissertation thesis is my work, and the achieved results are the findings of my research monitored and directed by my supervisors. All used sources of information are acknowledged in the attached list of references. I do not have a compelling reason against the use of the thesis within the meaning of Section 60 of the Act No.121 / 2000 Coll., on copyright, rights related to copyright and amending some laws (Copyright Act)

In Prague, February 2023

Salman Hasn

## Acknowledgements

I would like to express my deepest appreciation to all those who have supported me while working on this dissertation. Many thanks to my supervisors Ing. Daniel Vavřík, Ph.D. and Dr. Martin Peter Pichotka for their guidance and unlimited support.

I am also grateful to my colleagues Dr. Jan Žemlička and Dr. Jan Dudák, who helped me use the imaging equipment, for their advice, evaluations, and criticism. I appreciate my former colleague Dr. Karla Denaly Palma Alejandro, who was responsible for my training from the beginning and taught me the basics of X-ray imaging with photon counting detectors.

I would like to pay my special regards to Doc. Ing. Ivan Štekl.,CSc and Dr. Karel Smolek for their support during my work at the Institute of Experimental and Applied Physics.

I wish to thank Prof. Miroslav Husák, who opened the door for the cooperation between the Faculty of Electrical Engineering and the Institute of Experimental and Applied Physics. As I would like to thank Doc. Ing. Karel Dušek from Faculty of Electrical Engineering for providing us materials for the study.

I would like also to thank Dr. Jan Jakůbek, who was the first person I contacted to do this Ph.D. thesis. He then recommended me to contact Dr. Carlos Granja, whom I would also like to thank for his support.

Last but not least, words cannot express my gratitude to my family and friends who stand by me in good and difficult times.

# Abstract

X-ray computed tomography (CT) is extensively used for non-destructive industrial analysis to study the internal structure of materials and complex objects. In the microelectronics industry, X-ray computed tomography has proven useful for quality analysis and defect detection. However, inspecting electronic devices with standard CT is challenging due to the presence of many metals neighboring light materials causing various types of artifacts that affect the quality of computed tomography.

This thesis presents new techniques and data processing approaches in the field of energy-sensitive computed tomography, which are used to characterize materials and to study defects in electronic devices. Energy-sensitive computed tomography utilizes energy information from the projection data obtained by energy-sensitive methods. Several standard CT techniques were also tested and compared with the newly presented techniques. The results showed that the standard techniques are inefficient when the scanned samples, electronic components, have high metal content.

The work also addresses the spectroscopic performance of photon counting detectors in computed tomography after correcting the threshold mismatch between pixels. This new correction methods have helped to increase the energy resolution and improve the ability of the detector to discriminate materials with similar attenuation properties. Such correction is useful for applications that require high resolution at high energy spectra where the mismatch between pixels increases due to the invalidity of standard calibration methods.

The thesis mainly focuses on the inspection of epoxy underfill process for electronic devices by implementing data fusion of multiple computed tomography scans as an alternative method to reduce artifacts. To this end, the work presents a methodology of performing successful computed tomography that enable the inspection of light materials (epoxy) for samples with high metal that cannot be achieved using standard CT techniques. In addition, the work presents the first results of the epoxy underfill inspection for real samples from the industrial field, placing the X-ray inspection as an option for defect detection in the microelectronics industry.

## Key words

Photon counting detectors, multi-bin X-ray imaging, epoxy underfill process, defect inspection, metal artifact reduction, data fusion of multipositional computed tomography.

## Abstrakt (in Czech)

Rentgenová výpočetní tomografie se hojně využívá pro nedestruktivní průmyslovou analýzu a pro studium vnitřní struktury materiálů a předmětů. V mikroelektronickém průmyslu se rentgenová výpočetní tomografie osvědčila pro analýzu kvality a detekci vad. Kontrola elektronických zařízení pomocí rentgenové výpočetní tomografie je však náročná díky přítomnosti mnoha kovů, a také s ohledem na vznik různých typů artefaktů, ovlivňujících kvalitu výpočetní tomografie.

Tato práce představuje nové techniky a přístupy ke zpracování dat v oblasti energeticky citlivé výpočetní tomografie, které se používají k charakterizaci materiálů a ke studiu defektů v elektronických zařízeních. Energeticky citlivá výpočetní tomografie využívá informace o energiích z projekčních dat, získaných energeticky citlivými metodami. Bylo také testováno několik standardních CT technik, které byly porovnány s nově představenými metodami. Výsledky ukázaly, že standardní techniky jsou nevhodné, pokud mají skenované vzorky, elektronické součástky, vysoký obsah kovů.

Práce se také zabývá spektroskopickou odezvou detektorů, počítajících fotony, po korekci prahového nesouladu mezi pixely, a s jejich využitím ve výpočetní tomografii. Tato nová metoda korekce pomohla zvýšit energetické rozlišení a zlepšit schopnost detektoru rozlišovat materiály s podobnými útlumovými vlastnostmi. Taková korekce je užitečná především pro aplikace, které vyžadují vysoké rozlišení s vysokoenergetickými spektry, kde se nesoulad mezi pixely zvyšuje v důsledku neplatnosti standardních kalibračních metod.

Předložená práce se zaměřuje především na kontrolu technologie podlepení pro elektronická zařízení pomocí implementace fúze dat z více tomografických skenů, sloužící jako alternativní metoda pro potlačení artefaktů. Závěrem, práce představuje metodiku úspěšného nasazení výpočetní tomografie, která umožňuje kontrolu lehkých materiálů (epoxid) u vzorků s vysokým obsahem kovu, kterou nelze realizovat pomocí standardních CT technik. Kromě toho práce prezentuje první výsledky kontroly epoxidových podlepení pro reálné vzorky z průmyslu, čímž ukazuje rentgenovou kontrolu jako možnou volbu pro detekci defektů v mikroelektronickém průmyslu.

## Klíčová slova

Detektor počítající fotony, vícekanálové rentgenové zobrazování, spodní výplň epoxidem, kontrola defektů, nedestruktivní defeskopie, redukce artefaktů od kovů.

## Table of Contents

1	Introduction to X-ray computed tomography .....	17
1.1	Generation of X-rays .....	17
1.2	Interactions of X-rays with matter .....	18
1.2.1	Photoelectric effect .....	18
1.2.2	Compton scattering .....	18
1.2.3	Pair production.....	19
1.2.4	Rayleigh scattering.....	19
1.3	Beer-Lambert law of attenuation.....	20
1.4	X-ray spectrum and filtration .....	21
1.5	X-ray transmission radiography .....	21
1.6	X-ray Computed tomography.....	22
1.7	CT reconstruction algorithms.....	23
1.7.1	Filtered back projection algorithm.....	24
1.7.2	Iterative methods of statistical approach.....	26
1.8	Artifacts .....	26
1.9	Energy sensitive imaging .....	28
1.10	X-ray tubes .....	28
1.10.1	X-ray tubes with side window .....	28
1.10.2	X-ray tubes with transmission target .....	29
2	Recent advances in digital X-ray imaging detectors.....	30
2.1	Energy-Integrating detectors .....	30
2.1.1	Charge couple device .....	30
2.1.2	Flat panel detectors .....	31
2.2	Photon counting detectors .....	34
2.2.1	X-ray detection mechanism with PCDs.....	35
2.2.2	Common sensor materials for PCDs.....	36
2.2.3	Characteristics and challenges of PCDs .....	36
2.2.4	Medipix based detectors .....	37
2.2.5	Medipix for X-ray Imaging.....	39
2.3	Detector response correction.....	40

2.3.1	Flat field correction.....	40
2.3.2	Beam hardening correction.....	41
2.4	The experimental setups used in this work .....	42
3	Improvement of Timepix energy resolution correcting threshold variations .....	44
3.1	Timepix detector and classical equalization procedure.....	44
3.2	Threshold calibration.....	46
3.3	Principles of the new calibration methods .....	46
3.4	Energy-threshold per pixel calibration based on the matching method .....	47
3.4.1	Calculation of the gain and offset factors .....	47
3.4.2	Assessment of stability of the proposed method.....	49
3.5	Energy-threshold per pixel calibration using multiple mono-energetic sources.....	51
3.6	Comparison of the calibration results and application to imaging data .....	52
3.7	Conclusion remarks.....	53
4	Material decomposition based on multi-bin X-ray imaging.....	55
4.1	Basics of spectral imaging.....	55
4.2	Multi-bin X-ray imaging based on Timepix detectors .....	55
4.3	Materials and experimental setup.....	57
4.4	Dataset and results.....	58
4.5	Conclusion remarks.....	60
5	Inspection of epoxy underfill utilizing X-ray imaging techniques .....	61
5.1	Ball grid array packaging .....	61
5.2	Epoxy underfill technique .....	62
5.3	Standards for evaluating the underfilling process .....	63
5.4	Nondestructive techniques to control the quality of the underfill process .....	63
5.5	Epoxy underfill defects for power supply devices .....	63
5.5.1	Computed tomography parameters .....	65
5.6	Measurement strategy .....	66
5.7	CT improvement by reducing noise in the projection data .....	67
5.7.1	Improving the contrast-to-noise ratio.....	67
5.8	Metal artifact reduction utilizing different X-ray techniques.....	72
5.8.1	Techniques and approaches established in CT for metal artifacts reduction.....	72



5.8.2	Metal artifacts correction (MAR) algorithms .....	73
5.8.3	Correction of metal artifacts using sMARt from VGSTUDIO MAX .....	74
5.9	Dual Energy Computed Tomography as a tool to reduce metal artifacts .....	77
5.9.1	Rotary laminography (tilted or oblique CT) .....	78
5.10	Conclusion remarks .....	83
6	Epoxy inspection utilizing data fusion of multipositional computed tomography .....	84
6.1	Radiographic simulator aRTist.....	84
6.1.1	The source/spectrum module .....	84
6.1.2	The detector module .....	86
6.1.3	The geometrical model .....	86
6.2	Radiographic simulation to evaluate workpiece orientation .....	87
6.2.1	Phantom description.....	87
6.2.2	Simulation strategy and parameters .....	88
6.2.3	Evaluation of T1 orientation .....	89
6.2.4	T2 orientation.....	97
6.3	Concluding remarks .....	99
7	Experimental part.....	101
7.1	Samples description and preparation.....	101
7.2	Preparation of samples and tilt stands .....	101
7.3	Measurements strategy.....	102
7.3.1	Experimental results vs simulation .....	102
7.3.2	CT Reconstruction enhancement using DFMCT.....	104
7.4	Fused volumes of the scanned samples.....	107
7.5	Experimental results and segmented-fused volumes .....	108
7.5.1	Samples without excess epoxy resin (negligible amount of epoxy resin) .....	109
7.5.2	Samples with excess epoxy defects: .....	111
7.6	Discussion and interpretation about the excess epoxy defects.....	117
8	Conclusions.....	120
	Author's publications.....	122
	Citations .....	123
	References.....	124



# Abbreviations

AD	analog-to-digital
aRTist	analytical RT inspection and simulation tool
ARTs	algebraic reconstruction techniques
ASIC	application-specific integrated circuit
Avg	average
BGA	ball grid array
CAD	computer-aided design
CCD	charge couple devices
CERN	European Organization for Nuclear Research (from French Conseil Européen pour la Recherche Nucléaire)
CL	computed laminography
CMOS	complementary metal-oxide semiconductor
CNR	contrast to noise ratio
CT	computed tomography
DAC	digital to analog convertor
DECT	dual-energy computed tomography
DFMCT	data fusion of multipositional computed tomography
DQE	Detective quantum efficiency
EIDs	energy integrating detectors
FBP	filtered back projection
FDK	Feldkamp-Davis-Kress
FOV	field-of-view
FPDs	flat-panel detectors
FWHM	full width at half maximum
HE	high energy
IC	integrated circuits

iCT	international computed tomography conference
IEAP	Institute of Experimental and Applied Physics, Czech Technical University in Prague
I <sub>THL</sub>	Intensity threshold
LE	low energy
MAR	metal artifact reduction
Max	maximum
ML-EM	maximum likelihood expectation maximization
MOS	metal-oxide-semiconductor
MTF	modulation transfer function
NDT	non-destructive testing
NMAR	normalized metal artifact removal
PCBs	polychlorinated biphenyls
PCDs	photon counting detectors
ROI	region of interest
SAM	scanning acoustic microscopy
SD	standard deviation
STL	standard telegraph level
T1	orientation tilt 1
T2	orientation tilt 2
TFT	thin-film-transistor
THL	threshold
TOA	time of arrival
TOT	time over threshold
TPL	traversal-path length
TSV	through-silicon-via

## Introduction

The discovery of X-rays by Wilhelm Conrad Roentgen at the end of the 19th century formed a starting point in the history of internal body examination. For the first time, the invisible became visible, thanks to X-ray photons, which, in combination with a photographic plate, were able to penetrate matter and transmit information about the internal structure. The very first X-ray photograph was made by Roentgen in 1895 for his wife's hand. Later, the new discovery was heavily used in medicine by physicians to locate bullets in wounded soldiers. Until 1913, however, the use of X-rays for industrial applications was very limited because there were no X-ray tubes that could produce X-rays with sufficient penetrating power for industrial purposes [1].

Today, after more than a century, X-ray imaging modalities for industrial purposes have undergone significant progress thanks to developments in X-ray generation and detection mechanisms, as well as modern computers that enable the use of advanced methodology. Computed tomography (CT) is one of the most widely used X-ray inspection techniques in the industrial and medical fields. An object can be scanned with X-rays then reconstructed in 3D from a series of 2D images taken from different directions using a reconstruction algorithm.

Using CT, the internal structure of objects can be visualized without invasive procedures. Current CT technologies are capable of detecting failures and defects that are difficult to detect using conventional non-destructive methods [2]. X-ray computed tomography is ideal for examining complex objects that contain many materials with high or low atomic numbers. It is also possible to distinguish between different materials (material decomposition) by taking advantage of the fact that the X-ray attenuation coefficients depend on the atomic number of the composite elements of the scanned object.

Most X-ray imaging systems use X-ray sources that produce photons of wide energy spectra called polychromatic beams. Despite their present, monochromatic X-ray spectra are limited in use since they are produced only by synchrotrons under a high cost. When a polychromatic X-ray beam penetrates an object, the low-energy photons are attenuated more readily than the high-energy photons. This effect is called beam hardening, it propagates from the X-ray projections to the CT reconstruction of the scanned objects causing the appearance of artifacts [3]. Such artifacts are referred to as beam hardening artifacts, and in special cases related to the presence of metal parts, as metal artifacts. The metal and beam hardening artifacts degrade the quality of CT leading to misinterpretation of the obtained results.

The arise of photon counting detection technology has partially helped to solve the above mentioned problem by enabling energy sensitive imaging. Photon counting detectors (PCDs) can exploit the energy information of detected photons, allowing spectral information about matter to be recorded. These detectors offer high spatial resolution with suppressed noise and high dynamic range, making them ideal for spectral or multi-bin imaging [4]. Thanks to the advanced features of PCDs, images with different contrast of the same object can be acquired using different energy bins of the same X-ray spectrum. However, PCDs are inadequate when high-energy spectra are

needed because detection efficiency is limited since silicon is the most commonly used sensor material. High-Z sensor materials, which offer higher detection efficiency, are limited by polarization phenomena that make the sensor unstable over time and degrade the quality of the registered images [5].

Integrating detectors, such flat panels, commonly used for industrial applications, are a good option for imaging large objects with highly attenuated materials that require high energy spectra. When combined with advanced approaches such as data fusion, integrating detectors offer improved CT with lower artifacts for high energy applications.

This thesis addresses the efficiency of photon counting detectors of type Timepix for energy-sensitive imaging and their application for material decomposition in X-ray computed tomography. Timepix chips are developed by CERN in a framework of big collaboration involving several institutes and universities around the world [6]. To this end, a new correction method is presented to correct the mismatch between the pixels of the Timepix chip, which increases the energy resolution of these detectors. In addition, large area detectors are used to resolve electronic device materials using multi-bin X-ray computed tomography.

The thesis successfully demonstrates a data fusion of multipositional computed tomography (DFMCT) method to correct for metal artifacts in the inspection of complex objects that require the use of high-energy photons with integrating detectors. The dissertation presents a working method based on radiographic simulation to eliminate the CT artifacts caused by a pattern of highly attenuating material, such as ball grid arrays (BGA). The main focus is on the results of the investigation of the underfill process for real BGA samples that have excess epoxy defects on the surface of the integrated circuit and other components of the PCB.

The work on this Ph.D dissertation was carried out at the Institute of Experimental and Applied Physics of the Czech Technical University in Prague (IEAP), which provides a CT laboratory suitable for the targeted work.

# Dissertation objective

The main objective of this dissertation is to develop new methods and data processing techniques for the inspection of objects of various components using X-ray computed tomography. Specifically, the objectives of the thesis are:

- Increasing the energy resolution of photon-counting detectors, type Timepix, to improve material separation using this type of detectors
- Evaluation of multi-bin X-ray imaging for material decomposition using the large area photon counting detectors
- Development of advanced methods to reduce metal artifacts when investigating objects containing patterns of highly attenuated material.
  - Studying the effect of sample orientation on the resulting metal artifacts using X-ray simulations
  - Proposing to data fusion of multi-position computed tomography (DFMCT) as an alternative method for metal artifact removal
  - Performing DFMCT on real BGA samples to investigate the success of the underfill process.

# Thesis outline

**Chapter 1** provides a general overview of X-rays and their interaction with matter as an introduction to the description of transmission X-ray radiography and tomography. In addition, the reconstruction algorithms and the artifacts produced by computed tomography are discussed. Also mentioned are the types of X-ray tubes used for industrial computed tomography.

**Chapter 2** describes recent advances in digital X-ray detectors. The performance and limitations of both energy integrating detectors and photon-counting detectors are discussed. In addition to the X-ray setups used in this work, the operating principles of the photon-counting detector of type Timepix are presented.

In **Chapter 3**, the classical equalization and calibration methods for optimizing the Timepix detectors are presented. Then, the new calibration methods developed in this thesis to increase the energy resolution of the Timepix detectors are presented. These methods are based on pixel mismatch correction using calibration lines of monochromatic sources.

**Chapter 4** presents material separation using PCDs. For this purpose, multi-bin X-ray imaging was tested to separate different components of a tracking device. A final spectral (color) volume was obtained by RGB color coding of reconstructed volumes at different energy bins.

**Chapter 5** introduces the underfilling technology for BGAs and the associated defects. It summarizes the inspection techniques available to investigate defects associated with underfilling. It also describes the problem of performing conventional CT on BGA samples. The chapter presents our attempt to eliminate the metal artifacts between BGAs using various X-ray imaging techniques, such as dual-energy CT and laminography.

**Chapter 6** presents an X-ray simulation on a phantom similar to the studied BGA samples. The goal of the simulations was to determine the best orientation for BGA samples that would produce fewer metal artifacts. In this chapter, we also performed a data fusion of the multi-positional CT approach on selected reconstructed volumes of the phantom in different mounting positions.

**Chapter 7** shows the results of applying DFMCT to real BGA samples to study the epoxy underfill process. The experiments use the simulated results from the previous chapter. Based on the results, we were able to establish a correlation between the occurrence of excess epoxy defects and the success of the underfill process.

**The author's publication list** is at the end of the thesis, where parts of the work have been presented at international conferences and published in impacted journals.



# 1 Introduction to X-ray computed tomography

The following sections give a brief overview of the physical background of the generation of X-rays and their interactions with matter. It also discusses X-ray radiography and computed tomography and related concepts such as the reconstruction algorithms and the artifacts produced during reconstruction. The types of X-ray tubes used in transmission tomography are also presented.

## 1.1 Generation of X-rays

X-ray photons, usually produced by X-ray tubes, are electromagnetic radiation with wavelengths in the range of (0.01-10) nm, this corresponds to an energy range of 100 keV down to 100 eV. An X-ray tube is a vacuum tube with a cathode and an anode, the anode usually being made of tungsten or molybdenum. X-ray photons are emitted when an electron accelerated by high voltage strikes the anode, the target. The maximum photon energy is limited by the energy of the electron beam and is equal to the accelerating voltage times the electron charge [7]. An 80 kV tube cannot produce photons with energies greater than 80 keV. Two main physical effects occur during the generation of X-rays, resulting in to Bremsstrahlung and characteristic X-rays. Bremsstrahlung photons contribute to the continuous part of the spectrum and are produced when electrons are scattered by the strong electric field near the high-Z nuclei. While the characteristic photons are produced when the accelerated electrons knock out the electrons from the inner shells, electrons from higher shells fill the empty places that have lower energies. This process produces an emission spectrum of X-rays at some discrete energies called spectral lines. They can be seen in the X-ray spectrum as various deflections of the characteristic lines, Figure 1.

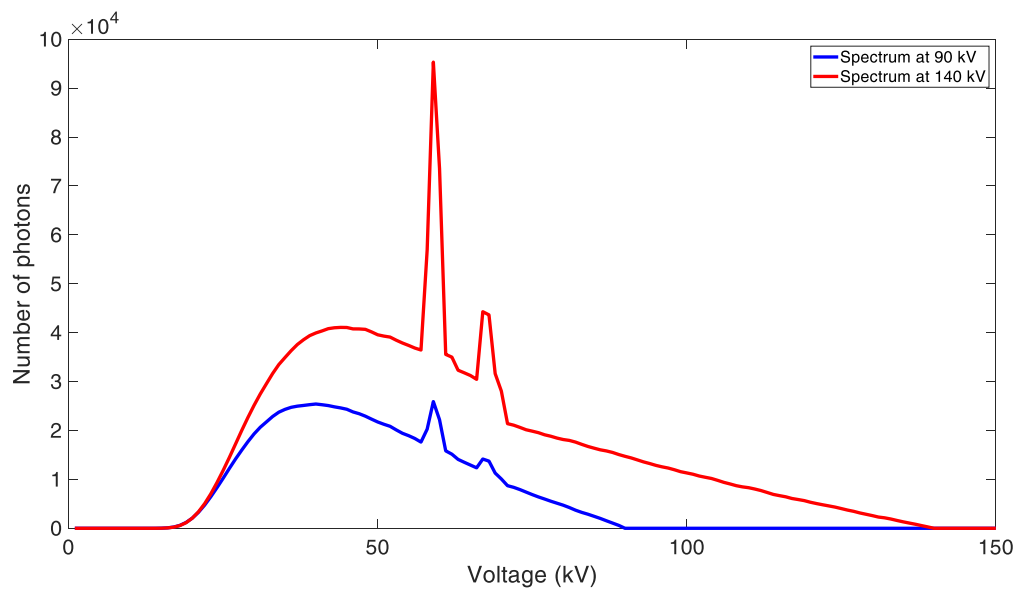


Figure 1. Simulated X-ray spectra at 90kVp and 140kVp for X-ray tube with tungsten anode and beryllium window. SpekCalc software was used for the simulation [8].

## 1.2 Interactions of X-rays with matter

The intensity of X-rays passing through a material is reduced by scattering or absorption within the material. Normally, photons travel a certain distance in the material before they release their energy by one of the following mechanisms:

- Photoelectric absorption
- Compton scattering
- Pair production
- Rayleigh scattering

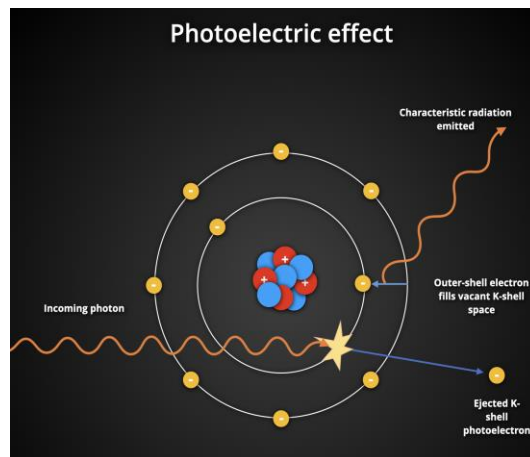


Figure 2: photoelectric effect, where an incident photon displaces an electron from an inner shell. The vacancy is immediately filled by an electron from the higher shell and the excess energy is emitted in the form of a characteristic X-ray photon [9]

### 1.2.1 Photoelectric effect

The photoelectric effect occurs only for bound electrons because of the law of conservation of momentum. When an incident photon is absorbed by an electron in the inner shell of the nucleus, an electron with energy  $E = E_{\text{photon}} - E_{\text{bind}}$  is released, Figure 2. If a photoelectric effect takes place in the sensor material of the detector, the electron subsequently loses its kinetic energy to the semiconductor material of the sensor through phonon excitation and ionization. The photoelectric cross section depends on the energy of the incident photon and atomic number  $Z$  of the attenuating material. Therefore, the probability of low energy photons losing their energy due to this effect is greater than that of high energy photons. The same is true if the probability of this effect occurring in materials with high  $Z$  is greater than in materials with low  $Z$ .

### 1.2.2 Compton scattering

Compton scattering or incoherent scattering occurs for high energy photons, it involves an interaction between the photon and an outer shell electron that has a negligible binding energy. As a result, the electron is ejected from the atom and the photon is scattered with slightly reduced

energy, Figure 3 (left). The scattering angle is dependent on the photon energy, while the high energy photons tend to forward scatter, the low energy photons usually perform a backward scatter, producing a ghost images on the detector [10].

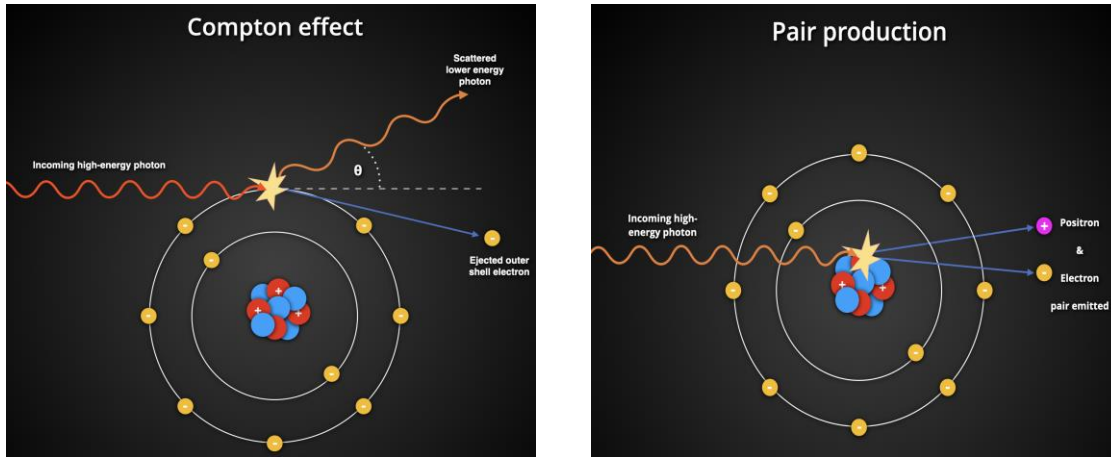


Figure 3. Compton scattering and pair production interaction mechanisms, left) Compton scattering in which the incident photon energy is divided between the ejected electron and the scattered photon. Right) pair production where positron and electron are formed near the nucleus [9]

### 1.2.3 Pair production

This effect occurs to photons with energy higher than 1.022 MeV in the coulomb field of the nucleus; it involves the transformation of a photon energy into an electron-positron pair, Figure 3 on the right side. However, as the range of energies for common industrial applications is well below 1 MeV, the pair production contribution to the total attenuation is zero.

### 1.2.4 Rayleigh scattering

The Rayleigh scattering occurs between the photon and bound electron without energy loss, the electron energy is increased without getting the level to leave the atom, and the electron goes back to its original energy state by losing the extra energy via emission of X-ray photon with identical energy but a different direction. The probability of this kind of scattering increases with increasing atomic number  $Z$  and decreases with the photon energy.

The total linear attenuation coefficient is a sum of all the previous mechanisms

$$\mu = \mu_{photoelectric} + \mu_{compton} + \mu_{Pair} + \mu_{Rayleigh}. \quad 1.1$$

The linear attenuation coefficient as a function of photon energy for silicon is shown in Figure 4 together with the contribution of individual interaction mechanisms.

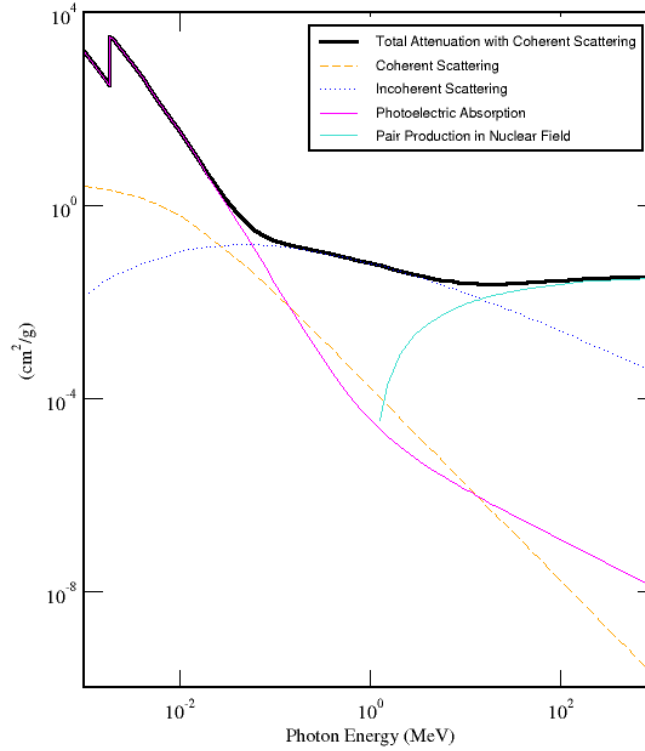


Figure 4. Linear attenuation coefficient for silicon as a function of photon energy, the photoelectric effect is the dominant effect at low energies, while Compton scattering (incoherent) dominates in the middle range, and pair production for the higher energies [11].

### 1.3 Beer-Lambert law of attenuation

The Beer-Lambert law describes the attenuation of photons as they pass through material as in the following equation.

$$I(x) = I_0 e^{-\mu x}, \quad 1.2$$

where  $I_0$  is the incident beam intensity,  $I$ : intensity after the beam passing through thickness  $x$ ,  $\mu$ : linear attenuation coefficient.

However, this equation is valid only for homogeneous material and monochromatic X-rays. To fit the realistic case for most industrial CT applications where non-homogeneous objects are scanned with a polychromatic X-ray spectrum, the equation was modified as follows:

$$I(x) = \int_0^{E_{max}} I_0(E) e^{-\int_0^x \mu(E) dx} \quad 1.3$$

Where  $\int_0^{E_{max}} I_0(E)$  describe the polychromatic spectrum and  $\int_0^l \mu(x)dx$  the integral along the path L in which  $\mu$  varies in every point of the path [10].

### 1.4 X-ray spectrum and filtration

The X-ray spectrum produced by an X-ray tube is characterized by the tube accelerating voltage and the tube current. While the acceleration voltage determines the maximum photon energy, the tube current increases the X-ray intensity, i.e., the number of photons emitted at each energy. Figure 1 shows simulated X-ray spectra at two different accelerating voltages (90 kV and 140 kV). The spectrum at 140 kV was shifted to the right, increasing the mean energy of the spectrum and the maximum emitted energy. However, X-ray spectra can be altered by filtering, which involves placing foils of a particular material between the tube and the detector. As a spectrum passes through a material, its mean energy changes due to absorption of the low-energy photons, which is called beam hardening. Figure 5 shows simulated X-ray spectra at 140 kV using different thickness of copper filter. The most common filters to absorb low energy photons in X-ray imaging are aluminum, copper and tin [12]. The type and thickness of the filter can be determined by a radiologist depending on the application.

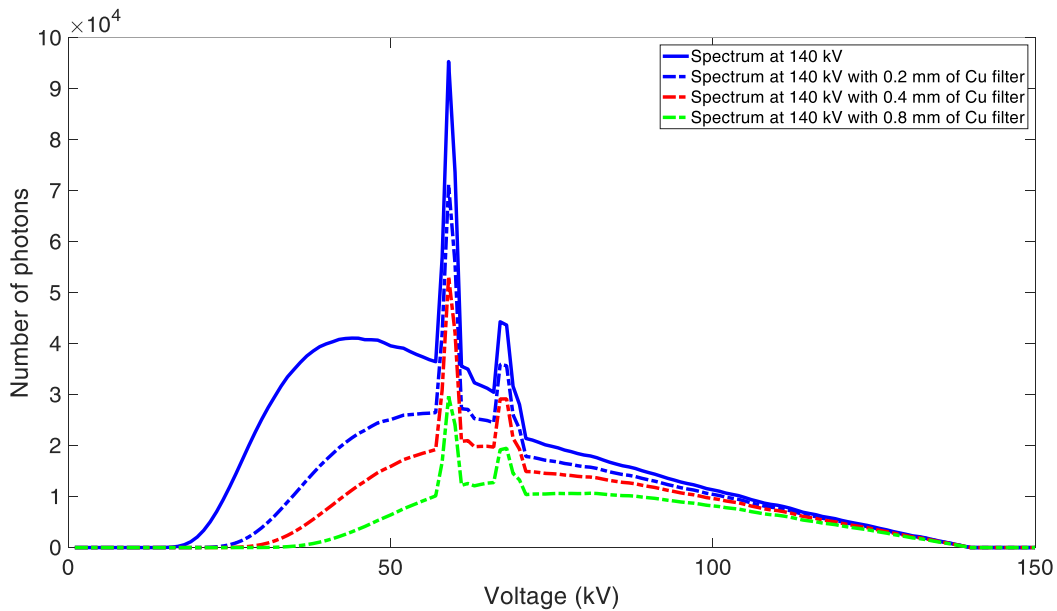
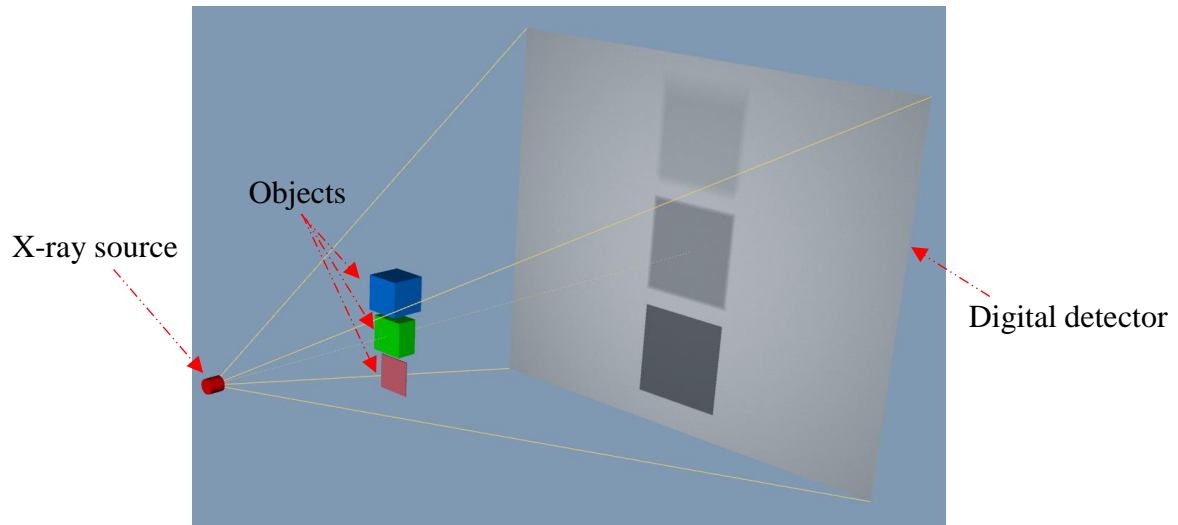


Figure 5. Simulated X-ray spectra at 140kV for X-ray tube with tungsten anode and beryllium window. The spectrum was altered by Cu filter of different thicknesses. SpekCalc software was used for the simulation.

### 1.5 X-ray transmission radiography

Since the discovery of X-rays by Wilhelm Conrad Rontgen in 1895, X-ray transmission radiography is still the one of the most commonly used X-ray technique. In its basic forms, this technique measures the decrease in intensity of X-rays after passing through the specimen, as described by Lambert's law. To perform transmission radiography, an object is placed between the

X-ray source and the detector. In digital detectors, the registered digital image (called projection) is a 2D matrix of brightness values represented by pixels in the spatial domain. The value registered by each pixel is proportional to the amount of signal arriving at each pixel. The contrast of the gray values between pixels of the digital image is an indicator of different attenuation percentages, which in turn are due to different materials or different thicknesses of the same material, see Figure 6.



*Figure 6. Principle of X-ray transmission radiography (cone beam geometry), in which the scanned object is placed between the X-ray source and the detector. The figure shows three objects made of different materials and with different thickness. The gray intensity values of the objects depend on the material type, with the thinnest object having a higher attenuation coefficient than the thickest object.*

## 1.6 X-ray Computed tomography

Computed tomography is a non-invasive technique that originated from 2D radiography and can be used to visualize the object in 3D. Representing the information contained in a volume of material in the imaged object is done using voxels (volumetric pixels). The theoretical basis for reconstruction was established by Johann Radon in 1917 [13]. In 1963, Cormack proposed a mathematical method for reconstructing images using a finite number of projections [10]. Cormack's theory turned into a real application in 1971 when the first CT scanner was developed [10].

The word tomography stems from the ancient Greek *tomos*, "section", and *graphein*, "write", and refers to the fact that the 3D image of the object is usually built by reconstructing the data slice-by-slice and by stacking the sections on top of each other [14]. A 3D computed tomography of an object can be created using a reconstruction algorithm from a series of 2D X-ray projections of the object taken from different angles. A Radon transform is applied on the projection data to obtain a sinogram using the following formula.

$$R(l, \theta) = -\log\left(\frac{I_{l,\theta}}{I_0}\right) = \int_{l,\theta} \mu(s) ds. \quad 1.4$$

Where  $I$  is the detected intensity as function of one-dimensional detector coordinate  $l$ .  $I_0$  The beam intensity after pass the object. The couple  $(l, \theta)$  indicating the detector position  $l$  reached by the ray and the angle  $\theta$  at which the image is taken, Figure 7 [14].

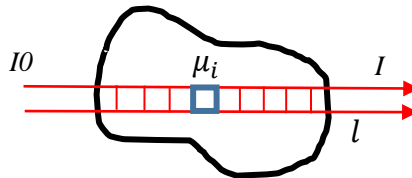


Figure 7. Volume represented by voxels where each voxel contribute to the total attenuation along the ray path  $l$

A sinogram is formed by stacking all of the projections acquired at different angles; in other words, a set of projection data for a given slice through an object is called a sinogram [10]. A sinogram is presented as an image where the number of lines corresponds to the number of projections taken; each line represents a projection at a given angle and the number of columns is equal to the width of the detector, Figure 8 [10].

The sinogram is also useful for analyzing the projection data and to detect abnormalities in a CT system. E.g., a defective detector channel manifests itself as a vertical line in a sinogram, since data collected by a single detector channel maintain a fixed distance from the iso-center (center of rotation), over all the projection angles [10].

## 1.7 CT reconstruction algorithms

The reconstruction algorithms determine the value of the photon absorption coefficient  $\mu$  at position  $(x, y, z)$  by giving all the values of  $R(l, \theta)$  for all paths  $(l, \theta)$ , and the problem of image reconstruction is a problem of inversion of the equation 1.4, Figure 7 [14]. The reconstruction

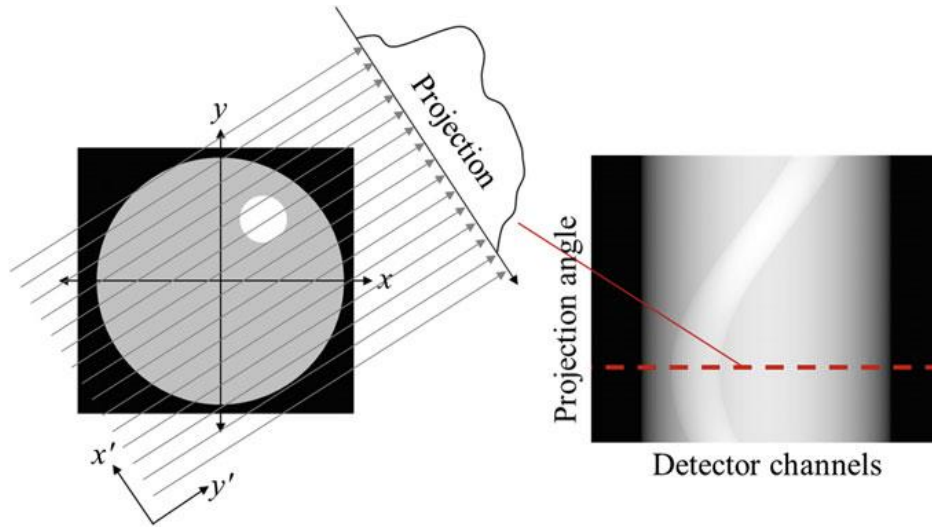


Figure 8. Illustration of mapping between the object space and the sinogram [10].

Algorithms use different approaches to the problem stated in equation 1.4, such as the analytical solution, algebraic formation, or statistical approaches. Analytical techniques model the object as a mathematical function, thus, reconstruct the object by solving a continuous integral equation [10]. Analytical techniques are divided into exact and non-exact algorithms, depending on whether or not the solution of the integral equation is exact [10]. Algebraic reconstruction techniques (ARTs) make use of iterative reconstruction approaches in which several iterations are performed until certain criteria are met. Statistical reconstruction algorithms are also iterative methods, but in this case the unknowns are assigned by means of likelihood principles [10].

Filtered back projection and iterative methods of the statistical approaches will be briefly discussed in the next subsection, as we used them in this work to reconstruct the CT data.

### 1.7.1 Filtered back projection algorithm

Filtered back projection (FBP) is the most commonly used reconstruction algorithm, which is characterized by its speed and gives good results in most cases. It is an extended version of the back projection technique, where the reconstruction of a slice is based on the principle of linear superimposition of the back projection data, Figure 9.

In FBP, the back projection is accompanied with a filtering process to remove typical star-like blurring caused in case of a back projection, usually using ramp filter, Figure 10 [10]. In its basic form, the FBP method assumes that the scanned object is homogeneous, the X-ray beam is monochromatic, and the focal spot is a point source. Each line of the calculated sinogram is filtered then backprojected into a voxel grid the size of the image field-of-view (FOV) [15].



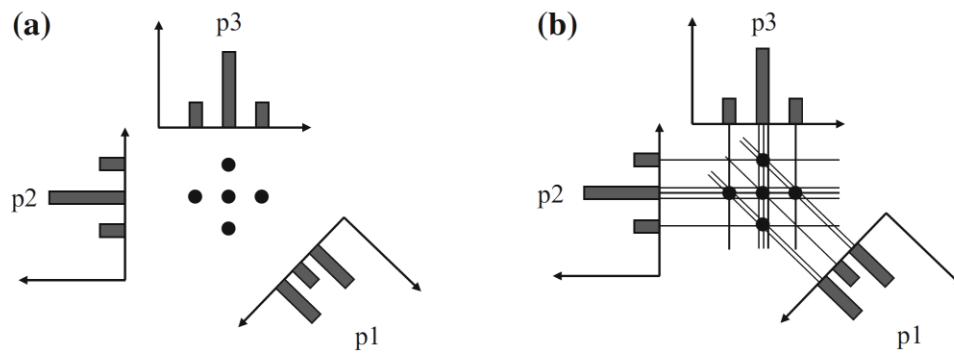


Figure 9. Concept of projection and backprojection. a) Projection: Each radiographic projection describes the distribution of attenuation coefficients along the given ray path. b) Backprojection: every radiograph is backprojected along the viewing direction from which it was acquired. The number of lines depicts the amount of absorption. A grid is generated, in which each contribution is added to the voxel intersecting that ray direction [10].

Using the known values of the projection angle and the distance along the projection, the measured attenuation is divided up equally among the voxels along the measurement beam path [15]. Increasing the number of projections increase the accuracy of the reconstructed slice.

Despite its popularity, FBP causes the appearance of artifacts like beam hardening and cupping artifacts. Such artifacts are caused by the assumption of monochromatic X-ray photons where most real CT scans use polychromatic radiation.

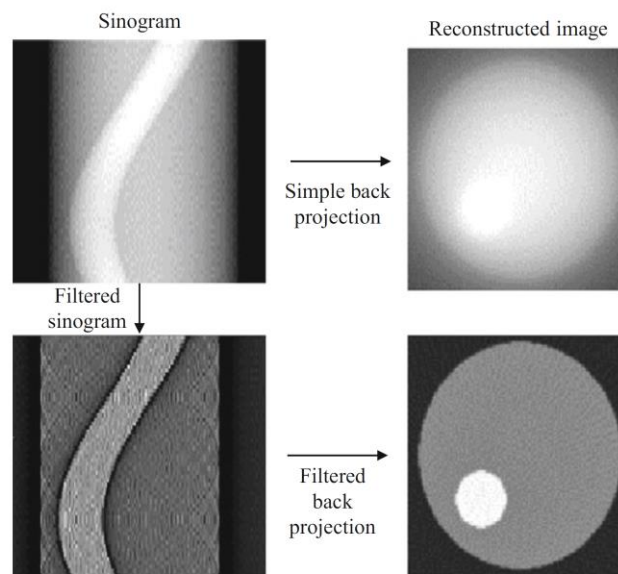


Figure 10. Illustration of reconstruction filtered/no-filtered data [10].

### 1.7.2 Iterative methods of statistical approach

The statistical reconstruction techniques were developed to overcome the limitations of the filtered back projection, which assumes a monochromatic beam and a homogeneous object.

To briefly explain these approaches in simple terms, we have quoted the following paragraph: “The basic idea on which iterative reconstruction algorithms rely is straightforward, and consists of a trial and error approach. The tomographic image to be reconstructed is considered as a discrete array of unknown variables, i.e., the attenuation coefficients. The set of projections, therefore, can be represented as a linear system of equations. Solving the reconstruction problem means solving this linear system. For each viewing angle, a forward projection is calculated by summing the intensities of all pixels along the respective ray path. The projection is then compared to the actual recorded projection and the process is iteratively repeated until convergence to the desired result. Iterative approaches provide better reconstruction in case of missing data projections. However, one of the major limitations of iterative algorithms is the computation time, which is normally significantly higher with respect to Feldkamp-type (FDK) reconstruction algorithms. The FDK algorithm is a widely used filtered-backprojection (FBP) algorithm for 3D image reconstruction from circular cone-beam projections” [10].

## 1.8 Artifacts

CT Reconstruction are accompanied with the appearance of erroneous structures that are not present in the scanned object, these structures are called artifacts. The artifacts degrade the quality of CT and lead to misinterpretation of the obtained results. CT Artifacts are generated by the reconstruction algorithms or by data acquisition errors (object movement or noisy pixels in the detector). The most common artifacts are:

**Streak artifacts** that appear at the edges of the reconstructed data. Such artifacts are caused by undersampling or corruption in the projection data, Figure 11(A).

**Motion artifacts** are caused by the unpredictable motion of any component of the CT setup (detector, sample, or source). Such artifacts appear as blurs or contours with double edges. Reliable fixation of the sample and detector helps to avoid motion artifacts. Usually, the movement of the source includes the movement of the focal spot with the measurement time, which in some cases requires correction of the data before reconstruction, Figure 11(B).

**Beam hardening:** while current reconstruction algorithms assume monochromatic X-rays, the reality is different, as current CT modalities use polychromatic spectra. When polychromatic spectra propagate through an object, the low-energy photons are attenuated faster than the high-energy ones, increasing the mean energy of the transmitted beam and making the spectrum harder. Such artifacts can be slightly reduced by using filters in front of the tube window that absorb the low-energy photons, increasing the tube voltages, and properly mounting the sample on the rotation stage in order to reduce the transmission paths, Figure 11(C).

**Ring artifacts** are usually caused by defective pixels in the detector. These pixels have much higher or much lower signals than the surrounding pixels, resulting in circular paths (rings) centered around the axis of rotation. Well-calibrated detectors can help avoid such artifacts, Figure 11(D and E).

**Metal artifacts** caused by photon deficiency (starvation) in the projection data when the object contains metallic parts that absorb the entire X-ray spectrum, Figure 11(F). Reducing this type of artifact requires advanced post-processing techniques, as will be discussed in Chapters 5, 6, and 7.

**Noise artifacts** caused by the low statistics of the projection data. This can be avoided by the technique of image averaging, which we will present later in chapter 5, to improve the quality of the reconstruction.

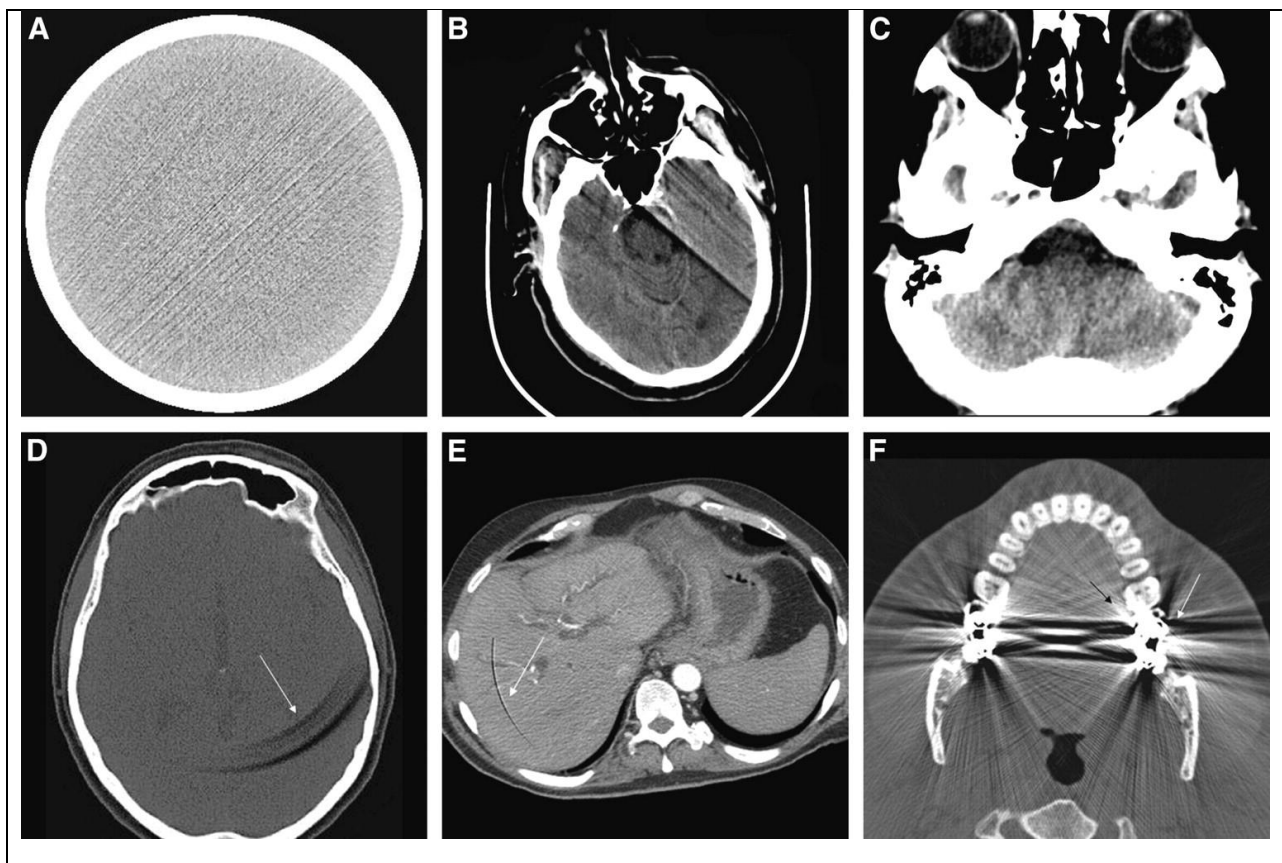


Figure 11. Examples of CT artifacts: streak artifact (A), motion artifact (B), beam-hardening artifact (C), ring artifacts (D and E), and metal artifacts (F) [16].

In addition to the aforementioned artifacts, scattering artifacts, aliasing artifacts, and cone beam artifacts may also be present. The most prevalent type of artifacts in CT measurements of microelectronic devices, studied in this work, are beam hardening and metal artifacts. To eliminate these artifacts, we will use the fusion approach as an alternative when the efficiency of other approaches is limited.

## 1.9 Energy sensitive imaging

Energy-sensitive or spectral X-ray imaging has been used for decades in medicine and NDT. The basic principle is to characterize the scanned object under different energy spectra.

The first application of energy-sensitive imaging was in medicine as dual-energy computed tomography (DECT). The DECT approach can be achieved by scanning the object with two X-ray sources and two detectors simultaneously (dual-source DECT). Or by performing two scans with the same detector and source in combination with appropriate filtering (sequential acquisition). Sequential DECT is used in this work to correct metal artifacts in which the Dexela flat panel detector was used at two different energy spectra. As mentioned earlier, shaping of the X-ray spectrum emitted by the X-ray sources can be achieved by filtering, where the filter absorbs the low-energy photons of the beam. The spectrum can be shaped depending on the type and thickness of the filtering.

The second and most recent implementation of energy-sensitive imaging can be performed with photon-counting detectors that allow photon energy selection. With the invention of PCDs, it has become easier to implement energy-sensitive imaging using the tuned detector through predefined energy thresholds to capture images of the same object using only portions of the X-ray spectrum. Energy-sensitive imaging using photon counting detectors is implemented in this work as multi-bin X-ray imaging as a tool for material decomposition.

## 1.10 X-ray tubes

As mentioned previously, the main components of an X-ray tube are a cathode and anode, which are inserted in a vacuum chamber. On the basis of their construction, X-ray tubes can be divided into X-ray tubes with side window and X-ray tubes with a transmission target [13]. Although the side tubes are described as high-power tubes, the transmission tubes are dedicated for high-resolution applications [17]. However, both types can be produced in the form of sealed tubes or open tubes which require vacuum pumps to maintain the vacuum inside the tube.

### 1.10.1 X-ray tubes with side window

X-ray tubes of this type are known as high power system, they are equipped with a tilted target relative to the electron beam, Figure 12. The size of the effective focal spot is determined by the orientation of the surface of the target normal [10]. Despite the type of the X-ray tube, only 1% of the kinetic energy of the electron beam are converted into X-rays, whereas the remainder is converted into heat (99%). Therefore, such tubes are cooled to avoid the anode damage either by circulating oil inside the anode or by adopting rotating anodes. Rotating targets are commonly used in the medical field, and have been introduced in the industrial CT field primarily for the higher power systems, whereas liquid metal jet sources are more suited for lower power systems [10].

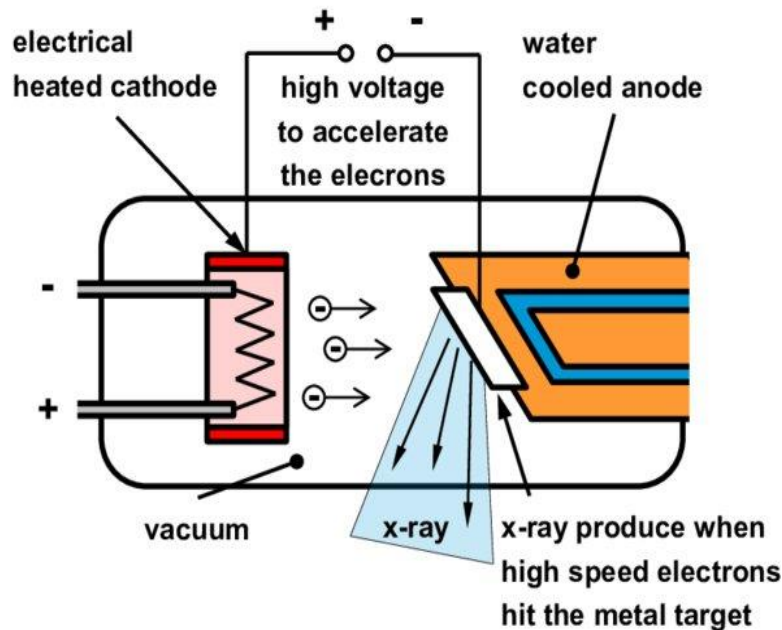


Figure 12. Schematic view of sealed X-ray tube [18]

### 1.10.2 X-ray tubes with transmission target

For smaller power CT systems and high resolution applications, X-ray tubes can be equipped with a transmission target that generates X-rays collinearly with the electron beam within the vacuum chamber [10]. In this case, the target is a thin material placed perpendicularly to the electron beam, so the photons are generated within an angle at the same direction of the electron beam, Figure 13. The thin layer of target material cannot resist high temperatures, thus limiting the allowable power range of the X-ray tube [10]. With this type of tubes the resolution is increased by decreasing the size of the focal spot to few micrometers or less.

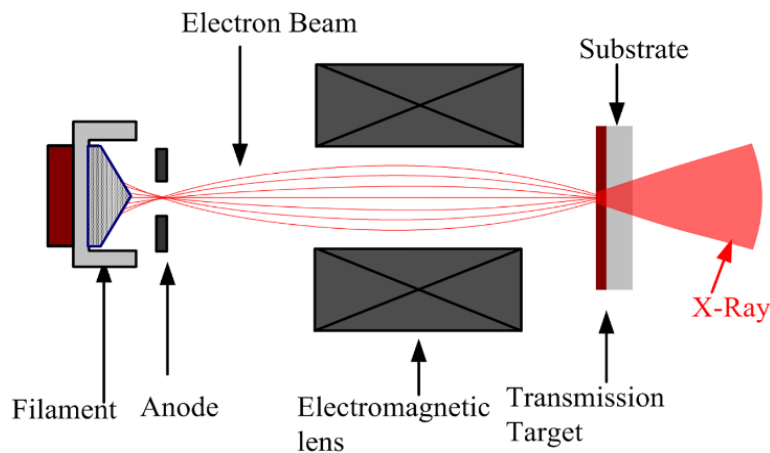


Figure 13. Schematic view of open X-ray tube (transmission target) [19]

## **2 Recent advances in digital X-ray imaging detectors**

In X-ray imaging, digital detectors are used to record the X-ray photons that pass through the scanned object. The acquisition of an image by a digital detector involves two main processes: First, the attenuation of the photons by converting their energy into electrical signals using a sensing material. The second process is the transfer of the electrical signal into a computer as encoded binary values originating from the electronic circuits of the detector. On this basis, digital X-ray detectors are divided into direct or indirect detectors based on photon detection mechanisms and energy integrating or photon counting detectors based on signal registration. The most commonly used X-ray imaging detectors are flat-panels, charge couple devices (CCDs), and single photon counting detectors. Evaluation and comparison between these detectors can be made based on physical parameters that directly affect the quality of the image obtained, such as spatial resolution, detection efficiency, dynamic range, and registered noise. Another parameter that can be considered when selecting a detector for a CT system is the acquisition speed in terms of frame rate per second, which is related to the readout electronics.

Each of these detector types will be presented individually in this chapter, explaining their operating mechanisms and characteristics, with focus on photon counting detectors.

### **2.1 Energy-Integrating detectors**

In energy-integrated detectors (EIDs), the charges generated by the interactive photons are integrated over the acquisition time, with the total charge stored in a storage capacitor. The stored charge is then transferred for digitization, with each pixel measuring the amount of charge stored in it. EIDs in the form of charge couple devices (CCDs) and flat-panels are widely used in CT facilities for industrial or clinical applications. Most EIDs are scintillator-based detectors with a variety of scintillator materials and thicknesses. The choice of scintillator material and thickness directly affects the quantum efficiency and spatial resolution achieved by these detectors.

#### **2.1.1 Charge couple device**

A CCD chip was first used in photography to detect visible light, using metal-oxide-semiconductor technology (MOS) to divide the chip into small pixels. To detect X-ray photons, a scintillating material was placed on the top of the chip. The photons are converted to visible light in the scintillator, which is passed through optical fibers to a photoelectric diode that generates electron-hole pairs. The electrons generated in each photodiode are collected by a potential well, which generates an integral signal for each pixel. The charge stored in each pixel is transferred from well to well by the charge-coupled device CCD (hence the name of the detector). Because of the need for scintillation material and the method of charge transfer, these detectors are classified as indirect integrated X-ray detectors. There are also CCD detectors with direct conversion; in this case, the scintillator is replaced by a semiconductor material, and such detectors are not very popular, Figure 14.

CCDs suffer from reduced spatial resolution caused by the scintillator, extra noise in the fibers, and charge movement from well to well. Although CCD detectors offer the smallest pixel size in detection technology down to a few microns, several studies comparing the state of the art of CCD detectors with PCDs of type Timepix have shown that the spatial resolution achieved with PCDS of 55  $\mu\text{m}$  pixel size is better than that of CCD cameras with 9  $\mu\text{m}$  pixel size [20] [21]. CCDs are also limited by the time required to read out the entire pixel matrix, on the order of 1 s due to well-to-well charge movement, which reduces the number of frames per second [21] [20] [22]. Another limitation arises from the limited dynamic range associated with the AD converters. The maximum capacity for one pixel is in order of 16bit [22].

CCD detectors are typically used for applications requiring high-resolution soft X-rays in medical imaging or diffraction imaging where there is no need for high energy photons. CCD detectors are not preferred for NDT imaging where hard X-rays are needed. They have been gradually replaced by complementary metal-oxide semiconductor (CMOS) detectors which offer advanced features.

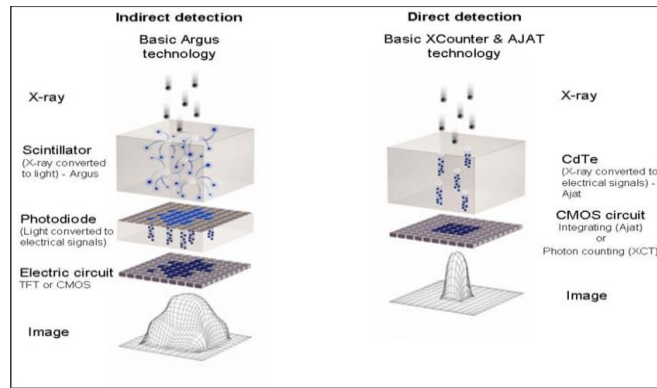


Figure 14. Indirect vs direct conversion in X-ray imaging detectors, left) Indirect detection where a scintillator material is used to convert X-ray photons to visible light which is then turned to electro-hole pairs in a photodiode, right) direct conversion where a semiconductor material is used to convert X-ray photons to electron-hole pairs [23].

### 2.1.2 Flat panel detectors

Flat panel detectors (FPDs) are the most widely used X-ray detectors in medical and industrial applications. They provide images with high resolution and wide dynamic range [24]. FPDs are divided into two groups:

1- Indirect detectors that use scintillators to convert absorbed X-rays into visible light photons. The scintillator is followed by an amorphous silicon plate (photodiode/transistor array), which in turn converts the light photons into electric charges, Figure 15. Each photodiode can be considered as a pixel; the charges accumulated in each photodiode are transferred to the readout circuit via a thin-film transistor (TFT), Figure 14 on the left side.

2- Direct detectors, in which the scintillators are replaced by a high-Z material such as amorphous selenium (a-Se), which converts the X-ray photons directly into electrical charges. An applied bias

voltage is used to drive the charges on the TFT to the readout circuits. The signal obtained with this type is also integrated, Figure 14 on the right.

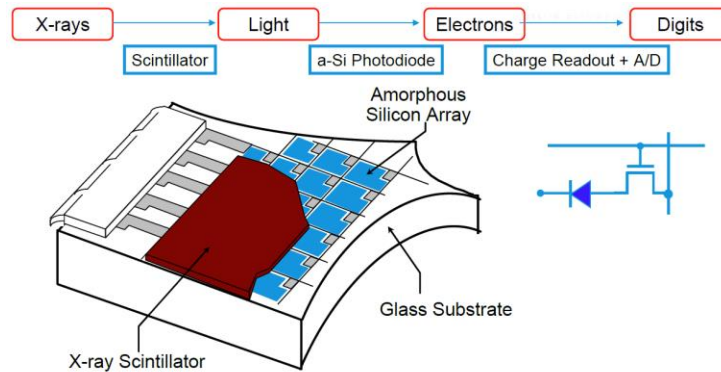
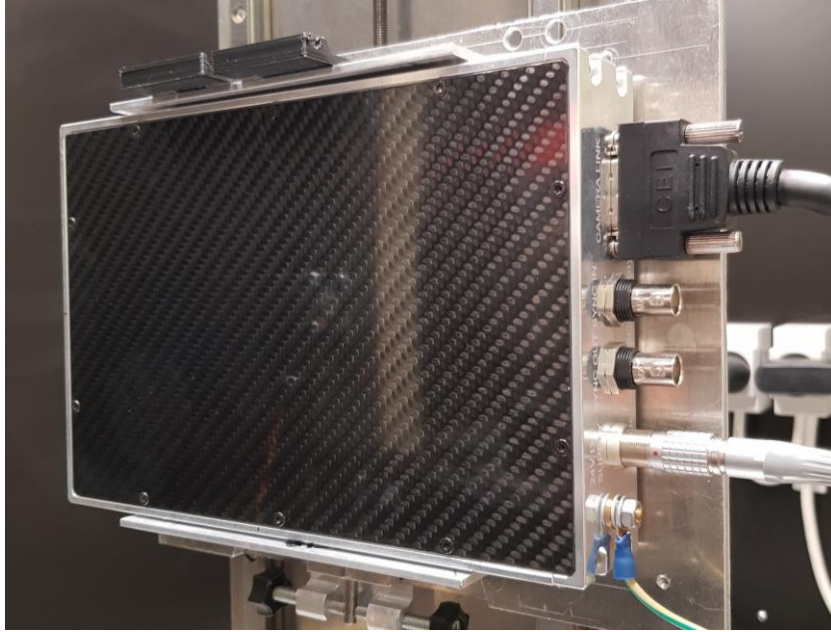


Figure 15. Main components of a-Se flat panel detectors [25]

In more recent flat panel detectors, TFT has been replaced by CMOS technology for data transmission and a-Si by crystalline Si. The advantages of these changes are higher readout speed, lower noise, higher dynamic range, and higher spatial resolution [26]. CMOS technology offers FPDs a smaller pixel size because crystalline Si is easier to be fabricated than amorphous Si. There is also the possibility of binning to form larger pixels [26] [27]. FPDs have large fields of view, which is suitable for NDT. For example, the XRpad24336-HWC detector offers a pixel matrix of  $4288 \times 3524$  with  $100 \mu\text{m}$  pixel pitch [28]. Figure 16 presents the Dexela 1512 flat panel detector installed in the IEAP micro CT labs which is used to acquire CT scans in some parts of the thesis. With a total resolution of  $1944 \times 1536$  pixels of  $75 \mu\text{m}$ , this detector is suitable for imaging of large industrial samples.

Advanced FPDs provide a 16-bit depth image; this parameter refers to the gray levels in which the image is displayed, as well as a frame rate of up to 60 fps for CMOS readout detectors, providing a real-time image. Newer technologies use plasma display panels to pixelate the scintillator, which allows the fabrication of large and thick scintillators without degradation of the resolution. FPDs with the pixelated scintillator have higher modulation transfer function (MTF) corresponding to the theoretically achievable maximum value [29].





*Figure 16. The Dexela flat panel detector with 1944×1536 pixels, 200  $\mu\text{m}$  CsI scintillation crystal, and 74.8  $\mu\text{m}$  pixel pitch. The detector is used in the micro-CT setup in IEAP.*

#### **2.1.2.1 Signal processing of flat panel detectors**

A signal generated by photon interaction in the flat panel detector is stored in a capacitor before being read out. During an acquisition time, multiple signals are generated for the same pixel, all of which add up including noise. Therefore, as the integration time increases, the integration noise becomes more pronounced and reduces the signal-to-noise ratio achieved by the detector.

In flat panel detectors, the amount of charges produced by a photon is directly proportional to its energy, which results in the contribution of the converted photons being weighted according to their energy. The low energy photons have less weight in the image than the high energy photons.

The main disadvantages of the flat panel are the high electronic noise and the inhomogeneity of the pixels. The electronic noise shows up in a dark image (offset image) obtained without illumination, while the inhomogeneity (gain image) is visible when the detector is irradiated when illuminated with constant X-ray conditions, Figure 17. Both effected are corrected before using the detector for imaging, the applied correction is called flat field correction and will discussed in the detector response section.

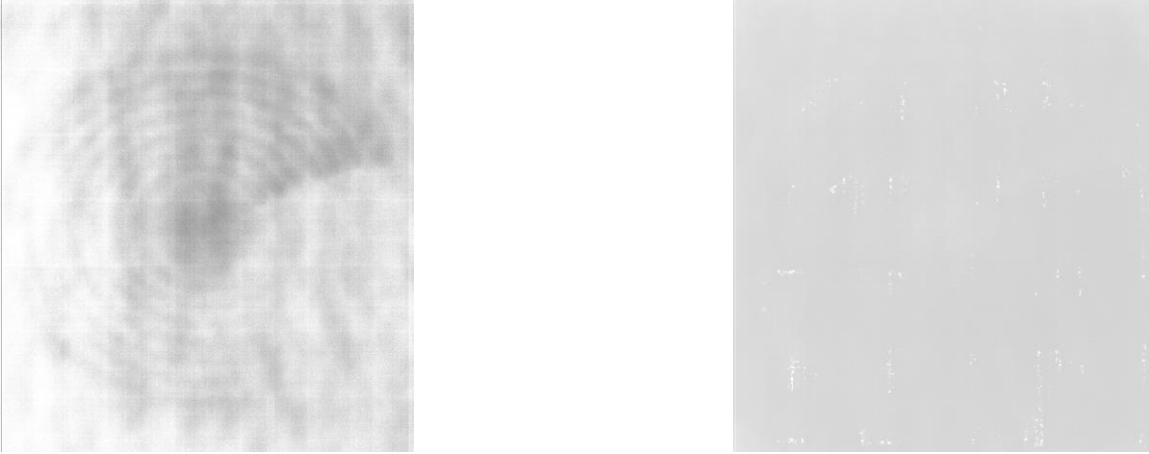


Figure 17. Offset and gain images obtained of the Dexela flat panel detector. Left) dark image (offset image) obtained with X-ray off. Right) gain image obtained when is X-ray is one without any object between the source and the detector.

### 2.1.2.2 Detective quantum efficiency

As an indicator to measure the performance of a detector, the detective quantum efficiency (DQE) is used according to the following formula.

$$DQE = \frac{SNR_{out}^2}{SNR_{input}^2} \quad 2.1$$

Where  $SNR_{out}$  is the output signal to noise ratio of the detector,  $SNR_{in}$  is the input signal to noise ratio of the detector. The DQE describes how effectively a detector can transfer the energy of the incident X-ray beam from the detector. Constant sensitivity ensures that the radiation intensity and grayscale values have a linear relationship. Flat panel detectors lose linearity at pixel intensities of 75% to 90% (depending on noise) of the total dynamic range, which is the maximum amount of signal variation that can be quantified by the detector [10].

## 2.2 Photon counting detectors

Unlike integrating detectors, photon counting detectors (PCDs) do not integrate the signal over time but register each photon individually (see Table 1 for more differences between EIDs and PCDs). These devices have the advantages of CMOS technology, which allowed each pixel to have its own charge-to-voltage converter. PCDs consist of two main components: a sensor layer of semiconductor material that converts the X-ray photos directly into pair charges, and an ASIC chip for electronic readout, with the two components connected via bump bonding. One of the PCDs in recent use is the Medipix/Timepix family, developed by CERN. The Timepix chip is one of the most commonly used ones for X-ray imaging, and will be discussed in detail later. In addition to the Medipix chips, many readout (ASICs) are used in various research centers and universities around the world. For example, Pixirad Pixie developed by the Italian National Institute of Nuclear Physics and the Pilatus chip developed by PSI, Samsung, Siemens PC, and so

on [30]. These detectors are similar in concept and technology, but differ in physical parameters such as pixel size, number of pixels, number of thresholds, energy resolution, and number of buttlabe sides. In this work, we will focus only on the Medipix/Timepix chip [6].

Table 1 comparison between EIDs and PCDs.

Energy integrating detectors	Photon counting detectors
Indirect and Direct conversion	Direct conversion
Whole signal is registered	Only signals above THL are registered
High spatial resolution	Good spatial resolution
Noise exist	Noiseless
Dark current	No dark current
Limited dynamic range	Unlimited dynamic range

### 2.2.1 X-ray detection mechanism with PCDs

When a photon releases its energy through a photoelectric effect in the sensor, all the photon energy is transferred to the inner electron that leave the atom. This generated photoelectron subsequently loses energy through phonon excitation and ionization in the semiconductor material, creating electron-hole pairs, Figure 18 (left). The energy required to form an electron-hole pair is 3.6 eV in silicon (ionization energy). The charge is then collected as a signal in the p-electrode and transferred to the preamplifier in the pixel ASIC via the bump-bonding ball. In the discriminator, a comparison with a previously defined threshold value takes place. The counter is incremented by 1 if the signal is above the threshold, Figure 18 (right).

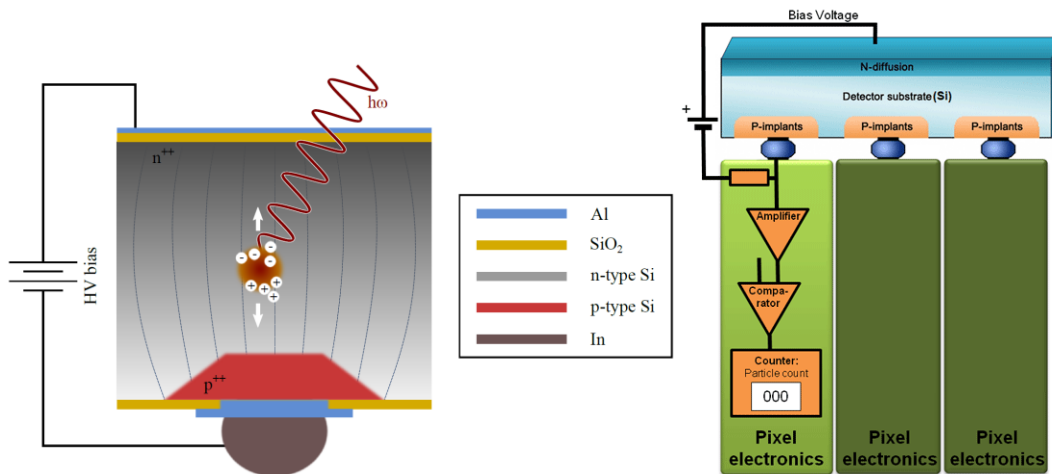


Figure 18: Photon detection inside semiconductor detector. Left: Creation of electron-hole pairs inside the sensor by the photon, Right: sensor with pixel electronics, where the formed signal moves from the sensor to the amplifier, then to the comparator, and if it is above the threshold, the counter will increase by [31].

### 2.2.2 Common sensor materials for PCDs

A variety of materials are used as sensors for photon counting detectors. The choice of material and thickness depends on the type of measurements to be made with the detector and the energy spectrum used for imaging. Table 2 presents properties of most commonly used sensors. Si is the material with the best behavior in terms of material homogeneity, temperature stability, availability, and cost. However, high-Z sensors, despite their drawbacks, are inevitable in many imaging applications because of their higher absorption efficiency.

Table 2 Properties of the most commonly used materials as sensors in Timepix detectors.

Semiconductor	Atomic number ( $Z$ )	Band-gap ( $E_g$ (300/ $eV$ ))	Ionization energy ( $E_i$ ( $\frac{eV}{pair}$ ))	electron – mobility $\mu_{e-}$	Hole- mobility $\mu_{p+}$
Si	14	1.12	3.61	1.4	0.45
GaAs	31.33	1.42	4.26	8.5	0.4
CdTe	48.52	1.56	4.43	1.1	0.1

The sensor's quantum efficiency can be calculated based on the following equation:

$$\emptyset(E) = 1 - e^{-\mu_s(E)ds} \quad 2.2$$

Where  $\mu_s(E)$  is the absorption coefficient,  $ds$  is the thickness of the sensor. Figure 16 shows the detection efficiency of silicon sensors at two different thicknesses compared to the quantum efficiency of GaAs and CdTe. The figure shows the low detection efficiency of silicon at high energies, where the efficiency drops %40 at 24 keV. Such low efficiency limits the use of silicon detectors for applications requiring hard X-rays.

### 2.2.3 Characteristics and challenges of PCDs

Compared to CCD and MOS based detectors, the improved characteristics of PCDs make this type of detectors the first choice for various applications. The presence of discrimination logic for each pixel circuit allows electronic noise to be reduced by setting a pre-threshold value. PCDs are considered noise-free energy dispersive detectors where only signals higher than THL can pass through the comparator. They have an unlimited dynamic range due to the 15-bit depth noise-free counter associated with each pixel. The count rate is on the order of MHz per pixel [30]. Direct photon conversion, in addition to the small pixel size, optimizes the spatial resolution obtained with PCDS. The measured modulation transfer function (MTF) for such detectors is 2 or 3 times better than that of indirect detectors with the same pixel size [21] [30]. Spectral or

multi- bin imaging can be performed with PCDs by adjusting the THL values that cut off unwanted photons.

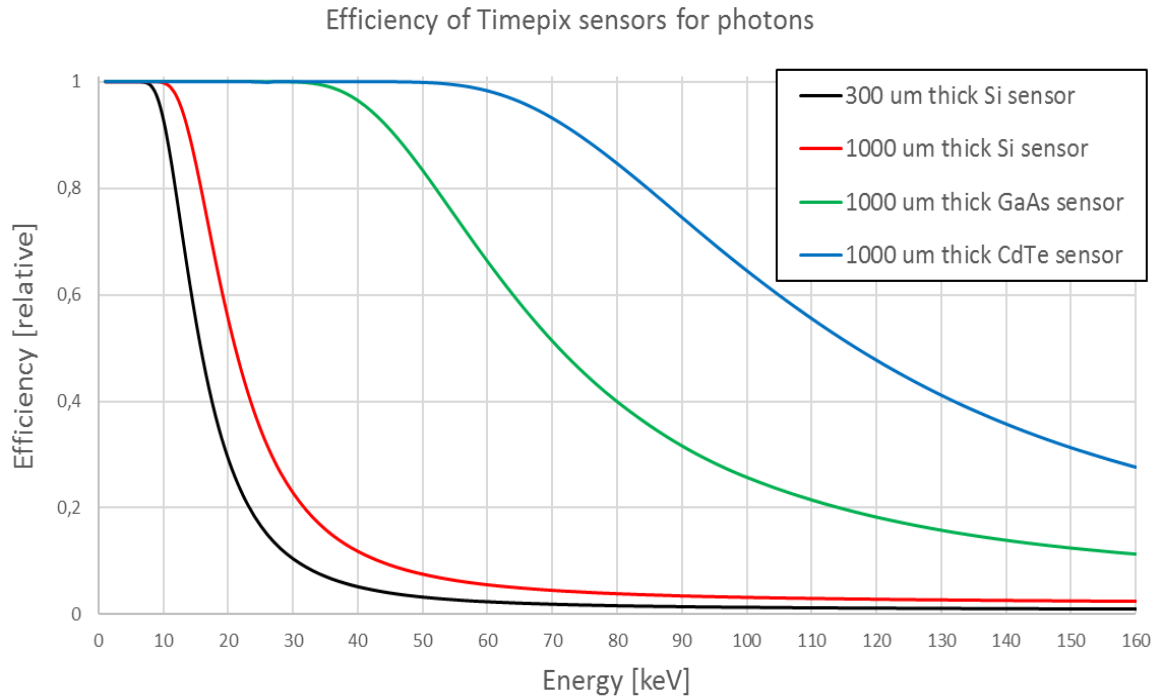


Figure 19: shows the quantum efficiency of silicon, gallium arsenide, and cadmium telluride. The figure shows the rapid decay of stopping power of Si sensors, in particular when compared with CdTe [13].

The shortcomings of these detectors lie in the degradation of spatial resolution due to charge sharing and propagation in the sensor material. The low detection efficiency for high-energy photons, especially in Si sensors, and the limited area of the chip related to CMOS technology lead to further shortcomings in PCDs. Some of these challenges have been overcome by the new generations of these detectors as will be discussed in the next section. Generally, the use of PCDs in medical settings showed an increase in spatial resolution with spectral information as well as a reduction in dose to the patient [32].

### 2.2.4 Medipix based detectors

Medipix detectors are classified as single photon counting detectors [33]. They were developed in the 1990s as part of an international collaboration at the European Center for Nuclear Research (CERN).

The first prototype was Medipix1, which comprises a matrix of 64×64 pixels with a pixel pitch of 170 μm. The chip is connected to Si or GaAs sensors that allow direct conversion of photons into electric charges. Each pixel circuit contains a preamplifier, a comparator, and a pseudo-random counter with 15-bit depth that provides a high dynamic range. The pixels count signals above the THL value while the shutter is open. The chip runs only in one mode, Medipix mode, in which

pixel registers the number of photons that hit the pixel. The total number of counts per pixel is stored as a digital image after the shutter is closed [34].

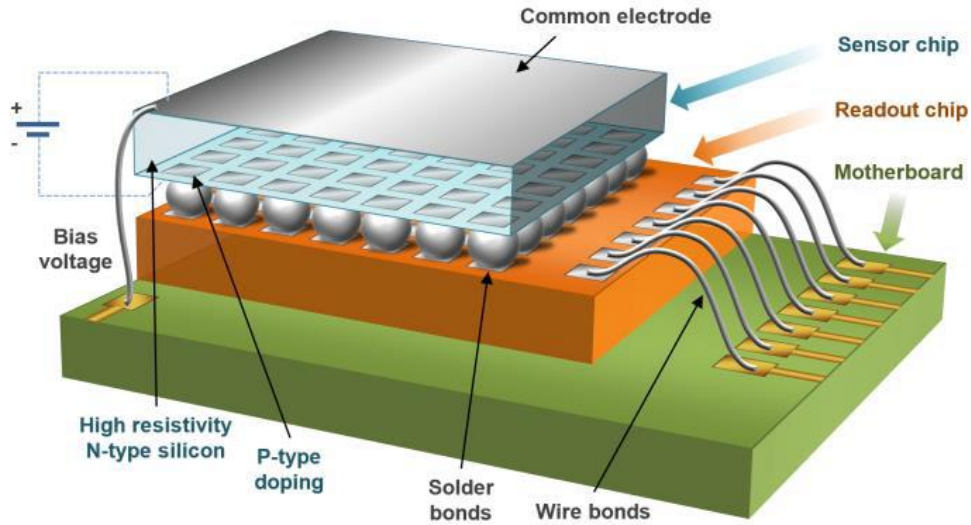


Figure 20: The hybrid semiconductor device Timepix consists of two chips: The pixelated sensor chip (usually 300  $\mu\text{m}$  thick Silicon, but also other materials are available e.g. GaAs and CdTe) and the readout chip. Both chips are connected using bump-bonding technique [31].

The success of the Medipix1 chip led to the Medipix2 collaboration, which used a 0.25  $\mu\text{m}$  CMOS process, helping to reduce the pixel pitch to 55  $\mu\text{m}$ . Two new chips were developed as part of this collaboration, Medipix2 and Timepix, both of which are divided into the same pixel matrix of 256 $\times$ 256 pixels with a pixel pitch of 55  $\mu\text{m}$ , but have different functions, Figure 20. While the Medipix2 is still under development, the Timepix is used for single event analysis and X-ray imaging, it will be discussed in more detail in the next section. Besides to the Medipix mode, Timepix chips run in two different modes, time-over-threshold (TOT) mode and time of arrival (TOA). In the TOT mode, the chip register the time the signal above the set threshold, utilizing a precise calibration, this mode can be used to measure the photon energy. On the other hand, the TOA mode register the time of arrival of the charges to the pixel.

The third generation includes two different chips, both of which are in use and overlap in certain applications. The first chip is Medipix3. It is similar to Medipix2 without including timing information represented by TOT mode. The chip offers two pixel pitches, 55  $\mu\text{m}$  pixel pitch and 110  $\mu\text{m}$ , where an internal binning can be applied to form a pixel pixel. The second chip is the TimePix3, which is similar to the Timepix chip with better time resolution and a different readout method based on continuous sparse data, suitable for particle tracking and spectral X-ray imaging.

The latest daughters of this family are Medipix4 and Timepix4, both still in development. The goal of this new generation is to design the pixel readout to be fully ready for Through-Silicon-Via (TSV) technology. This allows the chips to be read out through copper-filled holes that bring

signals from the front of the chip to its back. A comparison between all usable chips can be found in Table 3.

*Table 3 comparison between all Medipix/Timepix chips. Medipix: Single particle counting mode, TOT: Time over threshold, TOA: Time of Arrival, CSM: Charge summing mode.*

	<b>Medipix1</b>	<b>Medipix2 collaboration</b>		<b>Medipix3 collaboration</b>	
Chips	Medipix1	Medipix2	Timepix	Medipix3	Timepix3
Pixel size( $\mu\text{m}$ )	170	55	55	55    110	55
Pixel matrix	64×64	256×256	256×256	256×256    128×128	256×256
Number of THL	1	2	1	8	1
Operation modes	Medipix	Medipix	Medipix, TOT, TOA	Medipix , CSM	Medipix, TOT, TOA
Charge collection	holes	electrons or holes	electrons or holes	electrons or holes	electrons or holes
Readout system	MRS Mrros1	Muros2 MedipixUSB	Fitpix	Fitpix	Kathreine Advadac

### 2.2.5 Medipix for X-ray Imaging

Despite the superior properties of Timepix detectors, which provide noise-free signals with high dynamic range, their use for imaging purposes is limited due to their small sensor areas. To overcome this limitation, many techniques have been used to develop Timepix detectors with larger areas. Recently, large area photon counting detectors have become available in various sizes suitable for different applications in X-ray imaging. One of the first methods of constructing a detector with a larger area was to share a sensor between adjacent chips. LAMBDA is an example of a large area detector designed using the technique of sharing a sensor. The detector consists of a shared Si sensor bumped to 12 Medipix3 chips with a total resolution of 1536×512 pixels; the detector showed potential for material decomposition [35]. The disadvantages of this technology are the thermal expansion of the common sensor and chip carrier board which leads to dis-bonding of sensor and the chip over time [13].

Assembling multiple chips in one detector utilizing the tilting method was the solution to overcome the limitations of the previous approach. The tilting method was only possible after the success of producing edgeless sensors in which the chips were placed side by side to form a bigger detection area. With this technique, it was possible to assemble more chips to increase the active area of the detector like WidePIX<sub>10×10</sub> and WidePIX<sub>4×5</sub> installed in IEAP [36], Figure 21. The WidePIX<sub>10×10</sub> was brought to IEAP labs for some measurements, however it is placed at the Centre Telč of Czech Academy of Sciences as a high resolution imaging option [13].



Figure 21: Left) WidePIX  $4 \times 5$  detector of 20 tiles of edgeless Timepix detectors. Right) WidePIX  $10 \times 10$  detector composed of 100 edgeless Timepix chips.

While WidePIX  $10 \times 10$  contains 100 edgeless Timepix chips of  $300 \mu\text{m}$  silicon sensor, the WidePIX  $4 \times 5$  contains 20 edgeless Timepix chips of  $500 \mu\text{m}$  silicon sensor [36].

## 2.3 Detector response correction

Multiple post-processing methods are applied to the collected projection data to linearize and uniform the detector's response. Since PCDs and EIDs have slightly different working principles, the correct response of the used detector which impacts the quality of the obtained data should be implemented. Flat filed and beam hardening corrections are the most efficient detector response correction in X-ray applications.

### 2.3.1 Flat field correction

Regardless of detector type, flat field correction is beneficial in correcting pixel efficiency nonuniformity, and sensor inhomogeneity. X-ray projections for a workpiece at certain imaging parameters (acceleration voltage, current, and acquisition time) can be corrected by utilizing open beam projections (without the workpiece) and under the same parameters. The flat field corrected image can be calculated using the following formula [17].

$$FFI = \frac{RI - DI}{OI - DI} \quad 2.3$$

where  $FFI$  is flat-field-corrected image,  $RI$  is a raw image and  $DI$  is a dark image.  $DI$  measures the detector noise without any radiation source, therefor it is acquired with the X-ray tube off and it is necessary only for energy integrating detectors while the photon counting detectors suppress the noise. In addition to noise suppression, flat-field correction remove border defects between Timepix chips for large area detectors, Figure 22.



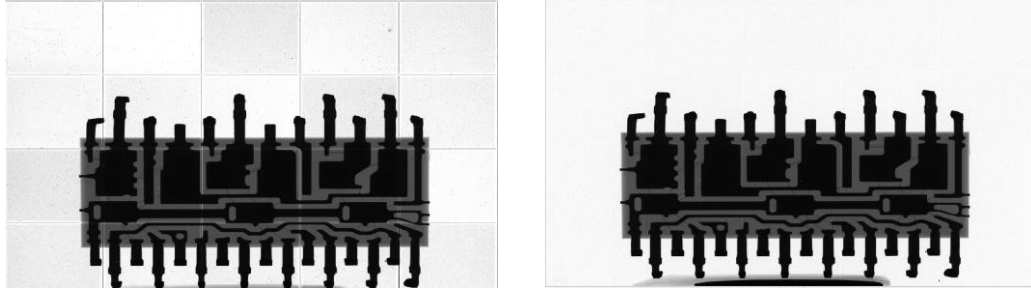


Figure 22. Images of an electronic component taken by WidePIX 4×5 detector, A) non-corrected image where noisy pixels besides border between the Timepix chips are visible. B) Flat-field corrected image where the noisy pixels and the border between the chips are removed.

### 2.3.2 Beam hardening correction

Beam hardening correction is a signal to thickness calibration method that equalize the detector response and minimize the effect of X-ray beam hardening caused by the polychromatic nature of X-ray spectra. The idea behind the beam hardening calibration is to calibrate each pixel of the detector with signals from different thickness of different materials, Figure 23. This correction works better for PCDS where each pixel records photons transmitted through material of different thickness. A relation between the thickness and signal can be set for each pixel element providing calibration points. In order to set a continuous BHC function for each pixel, the calibration points are interpolated or fitted with local exponential [17]

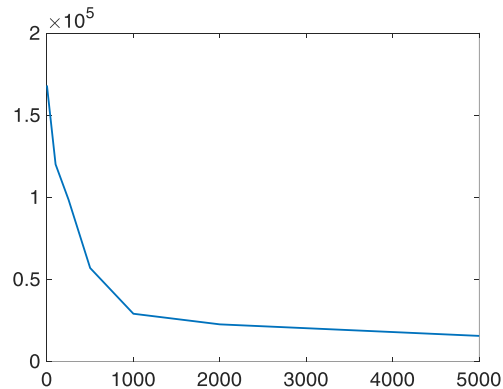


Figure 23. Thickness to signal plot with Cu as a calibration material.

Depending on the number of calibration points, the relation can be determined by the following formula [37].

$$S = A_k e^{B_k t} + C_k \quad 2.4$$

where  $A_k$ ,  $B_k$  and  $C_k$  are the free parameters, to be determined for each point  $k$ .

The beam hardening correction works better for workpieces with one material similar to the calibrated materials, in case of workpiece with several materials the correction works but with less efficiency.

## 2.4 The experimental setups used in this work

All CT measurements in this work were performed in the IEAP's CT laboratories. Two custom-built CT scanners are installed in the IEAP laboratory, both of which provide X-ray transmission tomography, where the sample rotates on a rotational stage between a fixed detector and a source. Both scanners use a 3D cone of X-rays (cone-beam geometry) that allows the specimen to be scanned in one go. They are suitable for non-destructive testing of industrial and biological samples of limited size.

The first CT setup is equipped with a 150 kV Hamamatsu L12161-07 X-ray source, a tungsten target with a beryllium window, and selectable focal spot modes depends on the applied voltage (small focus mode around 5  $\mu\text{m}$ , medium focus mode at 20  $\mu\text{m}$ , and large focus mode at 50  $\mu\text{m}$ ), Figure 24. By changing the magnification and focal spot, the maximum spatial resolution of this setup can reach up to 5  $\mu\text{m}$ . Depending on the type of measurement, one of the available detectors can be used for the measurements, here a Dexela flat panel or a large area photon-counting detector, Figure 24.

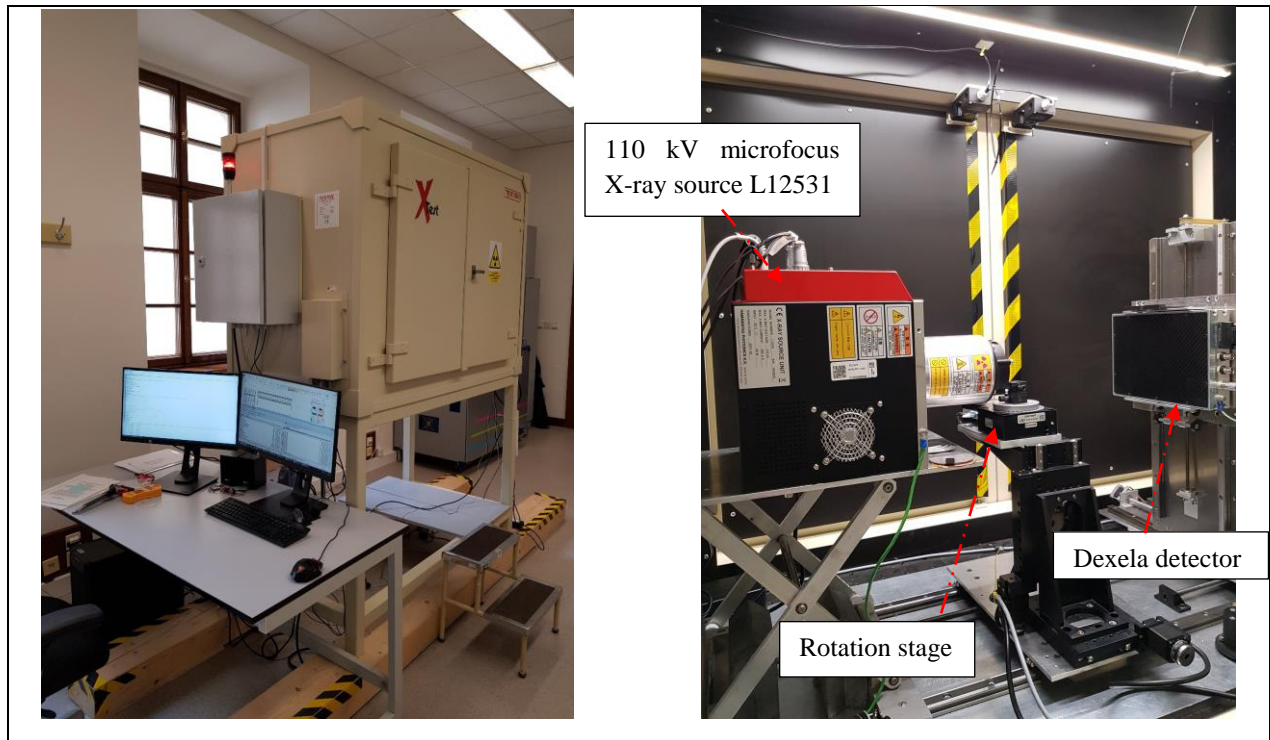
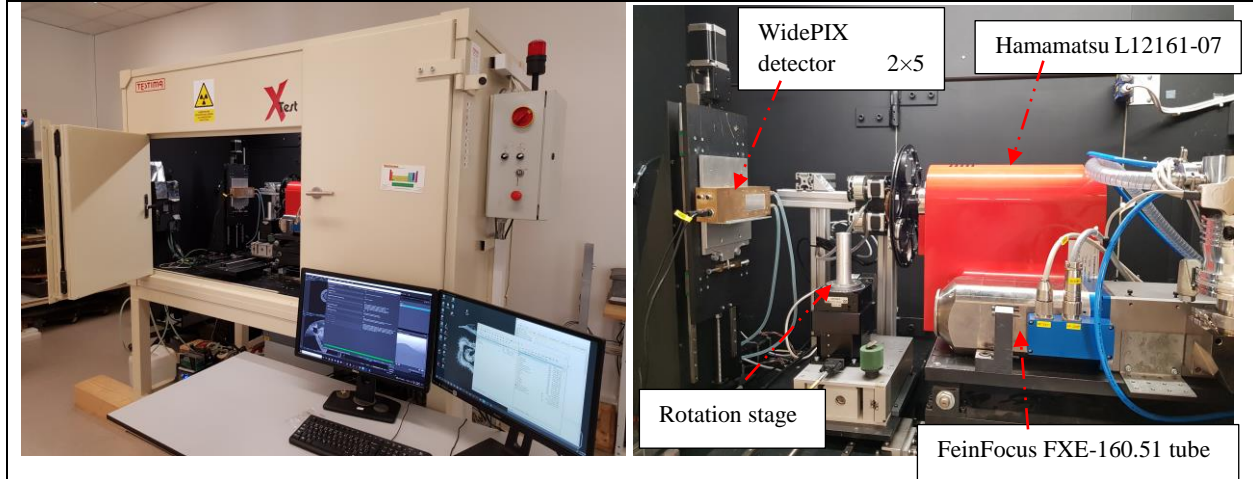


Figure 24. The micro-focus X-ray setup installed at IEAP. Left) the cabin that houses the setup, the photo was taken while a CT scan is running. The PC presented here are used to control the setup and process the CT data. Right) the components of the setup.

The second CT setup is equipped with a FeinFocus FXE-160.51 tube, Figure 25. With a maximum power of 10 W at 160 kV, the setup provides a maximum spatial resolution on the order of 1  $\mu\text{m}$  [17]. Typically, one of the WidePIX detectors available from IEAP is used in this setup, since photon-counting detectors offer higher resolution than integrating detectors.



*Figure 25. The nano-focus X-ray setup installed at IEAP. Left) the cabin that houses the setup. The PC presented here is used to control the setup and process the CT data. Right) the components of the setup, a micro X-ray tube is also temporarily installed next to the nano-focus tube, one of the tubes is used depending on the type of measurement*

### 3 Improvement of Timepix energy resolution correcting threshold variations

This chapter describes the basic configurations required to operate a TimePix detector. It also describes new calibration methods for TimePix detectors operated in counting mode, the mode of choice for high-flux imaging. The methods were applied to a single-chip TimePix detector with  $256 \times 256$  pixels and allowed us to correct the energy threshold in each pixel by determining the true threshold-energy relationship of each pixel, thus improving the spectroscopic information obtained from the detector. The above correction methods were published in the author's articles list [38].

#### 3.1 Timepix detector and classical equalization procedure

As we already mentioned, the TimePix detector is a hybrid semiconductor detector which consists of a sensor layer that comes with a variety of possible thicknesses and materials, bump-bonded to a pixelated electronic read-out chip (ASIC). The sensitive area is segmented into  $256 \times 256$  pixels, with a pitch of  $55 \mu m$  and a total sensitive area of about  $1.98 cm^2$ . Each pixel acts as an ionizing chamber, consisting of circuitry for pre-amplification, signal comparison and data storage. The detector operates in 3 different modes, Figure 26:

- Counting mode (one count for each signal above THL)
- Time over THL (particle energy measurement)
- Time of arrival (TOA)

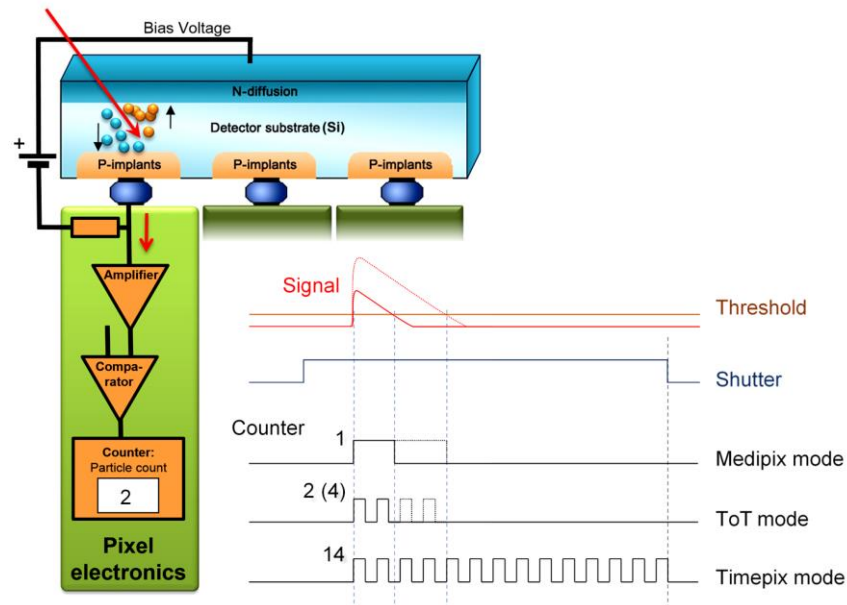


Figure 26. Scheme of principle of signal acquisition of the Timepix detector [31].

The main feature of the pixel cell is the discrimination logic, where the incoming signal is compared to a threshold level, providing discrimination by photon energy. This parameter can be set by Pixelman readout software or Pixet the newer version [39].

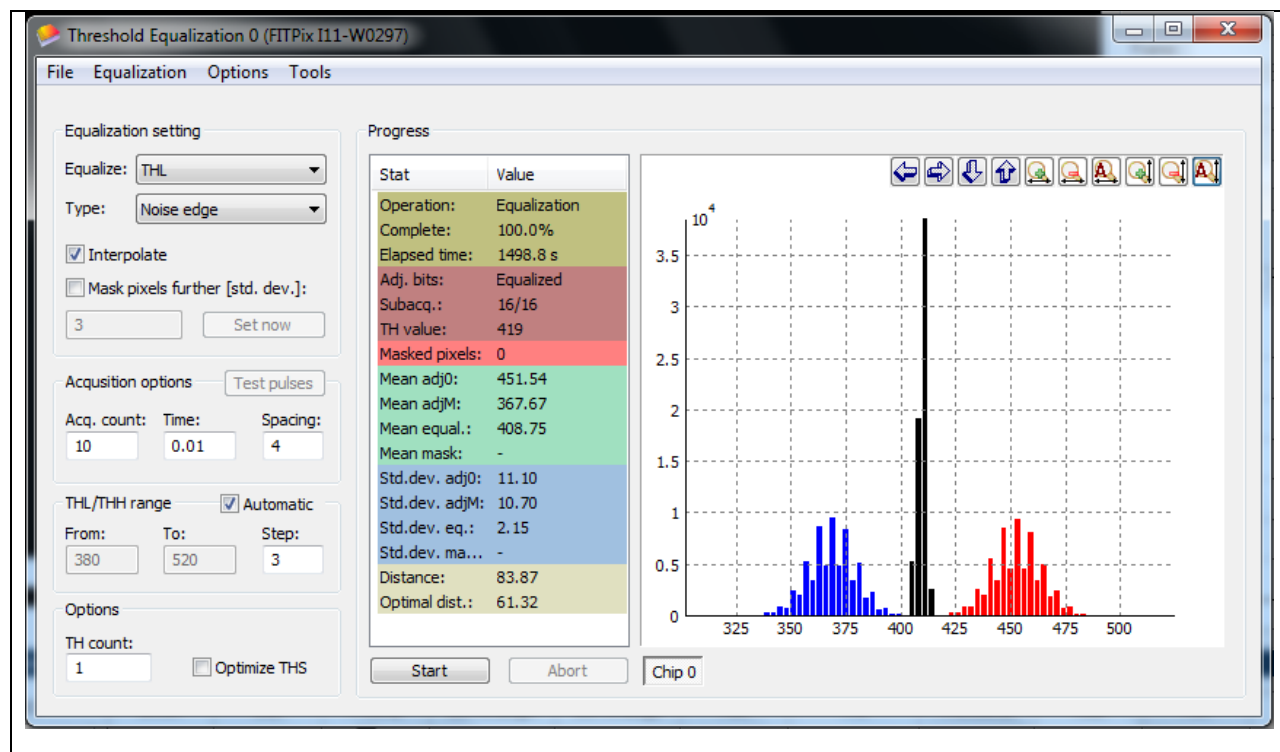


Figure 27: Threshold equalization plugin of the Pixelman software. Two THL adjust bits values are set to study the pixels THL distributions (red for THL set to zero and blue for THL set to maximum). The black distribution represents the equalized values.

As the Timepix chip contains 65,536 pixels, those pixels vary from each other due to fabrication. An adjusting process is needed to minimize the dispersion between pixels and to make them identical response, the process called threshold equalization, Figure 27. A 3-bit threshold adjustment mask is used during the equalization process to homogenize the detector response in terms of a set energy threshold [40]. Typically the noise edge of the detector itself is used for this equalization process, providing a narrow response distribution at the lowest available to the detector in noise free operation, Figure 27.

However, this method only corrects the pixel response in a single point of the energy spectrum, not taking into account the THL-energy response mismatch of single pixels. Furthermore the granularity of the equalization is limited by the 3-bit depth of the adjustment mask. In order to obtain clear spectroscopic separation in imaging, in particular at energy thresholds far from the equalization point, additional measures must be taken.

### 3.2 Threshold calibration

The threshold value of the Timepix detectors is tied to a DAC setting value of the chip. Therefore, a calibration procedure is required to determine the relationship between the actual energy and the threshold setting. Timepix calibration can be performed by measuring the spectrum of radiation sources with known energy in TOT mode. Normally, gamma rays from the source Am-241 (the energy of the emitted photons is 59.5 keV) are used to measure the energy response at higher energies. For the lower energies, a series of foils made of pure materials can be used to obtain monochromatic XRF radiation lines, such as copper at 8 keV and indium at 24.12 keV. The relationship between the TOT and the deposited energy in the sensor is described by the following formula.

$$f(x) = ax + b - \frac{c}{x - t} \quad 3.1$$

The formula shows a nonlinear dependence at low energies near the noise edge of the chip, at energies above 8 keV the relationship becomes linear, Figure 28 . Therefore, for a good calibration, 4 points are needed (4 energy lines), two of which should be in the nonlinear region (to determine c and t), while the other two should have high energies to describe the linear part of the curve (to determine a and b) [41].

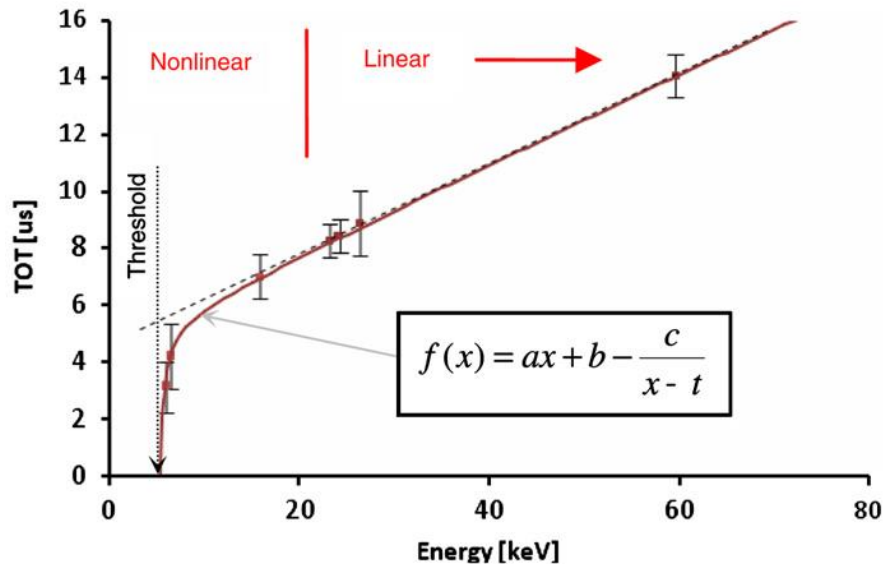


Figure 28. Dependence of time over threshold (TOT) on measured energy in a single pixel. The dependence is modeled by a surrogate function  $f$  that depends on four parameters [41].

### 3.3 Principles of the new calibration methods

To correct the threshold mismatch between pixels throughout the energy spectrum, two calibration methods are presented, based on acquisition of THL scans from the noise edge up to the highest energy emitted by the source, utilizing single photon counting mode. The first method is based on

detection of apparently polychromatic spectrum of monochromatic source to obtain one calibration point and consecutively to match the spectrum of the THL scan of individual pixels, whereas the second method necessitates multiple threshold scans of different monochromatic sources in order to obtain several calibration points.

In case of spectrum matching we exploited the fact that, due to charge sharing, a monochromatic source in counting mode shows a broad polychromatic tail towards lower energies, giving us all the data required for the method in a single scan of a single gamma source [42] .

The following steps were performed in the first method:

1. Detector equalization to get the threshold adjustment mask near the noise edge.
2. THL scan in presence of a monochromatic source, featuring a prominent gamma peak. The scan is performed from noise edge up to the highest detectable energy of the source (in case of Am-241 this is the 59.5 keV peak).
3. Determining the actual threshold value for each pixel at this peak by fitting.
4. Matching (stretching) the THL scan spectrum for all pixels to determine the gain and offset factors for each pixel.
5. By interpolation and extrapolation, the number of counts was corrected at each energy channel measured.

The second calibration method requires additional calibration points; therefore steps 2-3 of the previous method are repeated multiple times in presence of different fluorescent targets. Here we chose zirconium (Zr at 15.77 keV) and copper (Cu at 8 keV) as additional calibration points.

### **3.4 Energy-threshold per pixel calibration based on the matching method**

#### **3.4.1 Calculation of the gain and offset factors**

A TimePix silicon detector with a thickness of 1 mm, biased at 400 V, was used to verify our methods. After threshold equalization at the detector noise edge, the detector was placed in front of the Am-241 source and a THL scan was taken. The differential of the THL scan, summed over all pixels, reveals two peaks emitted by the source at energies 59.5 keV and 26.3 keV, Figure 29 (left). Whereas visible in the summed spectrum, the 26.3 keV peak suffers from poor statistics, charge sharing and high THL dispersion contribution in the single pixel scans and can hardly be used for fitting in the single pixel spectra. The THL scan reveals deviating positions in THL value of the 59.5 keV peak, Figure 29 (right). As well as deviating THL gain and signal amplitude between different pixels, Figure 30 (left). After the spectrum matching procedure these differences have been compensated, Figure 30 (right).

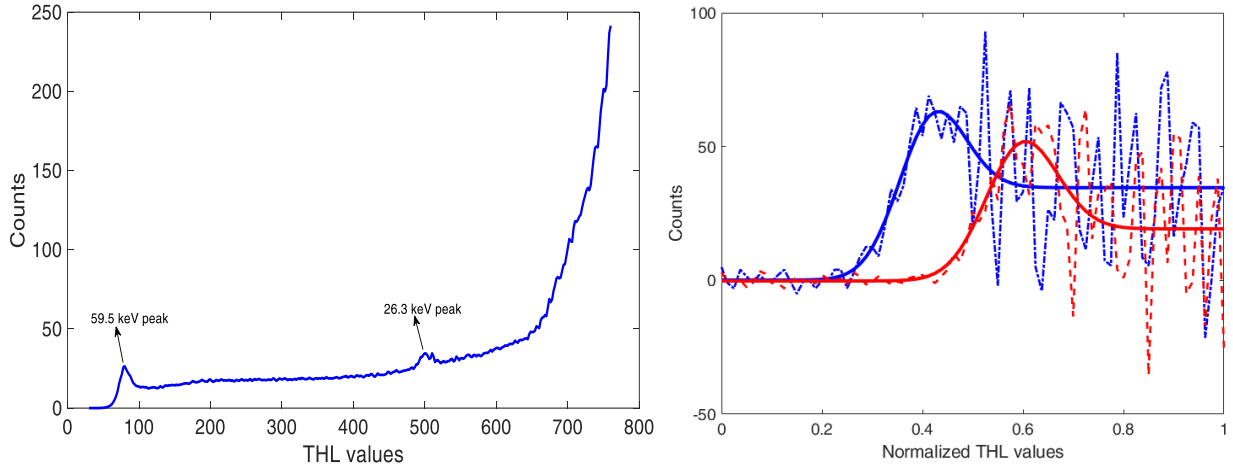


Figure 29. Left: Differential THL scan of 1mm Si Timepix detector in presence of an Am-241 source, Right: Am Peaks at 59.5keV of 2 random pixels fitted using Gaussian + error function, THL values normalized to [0-1]

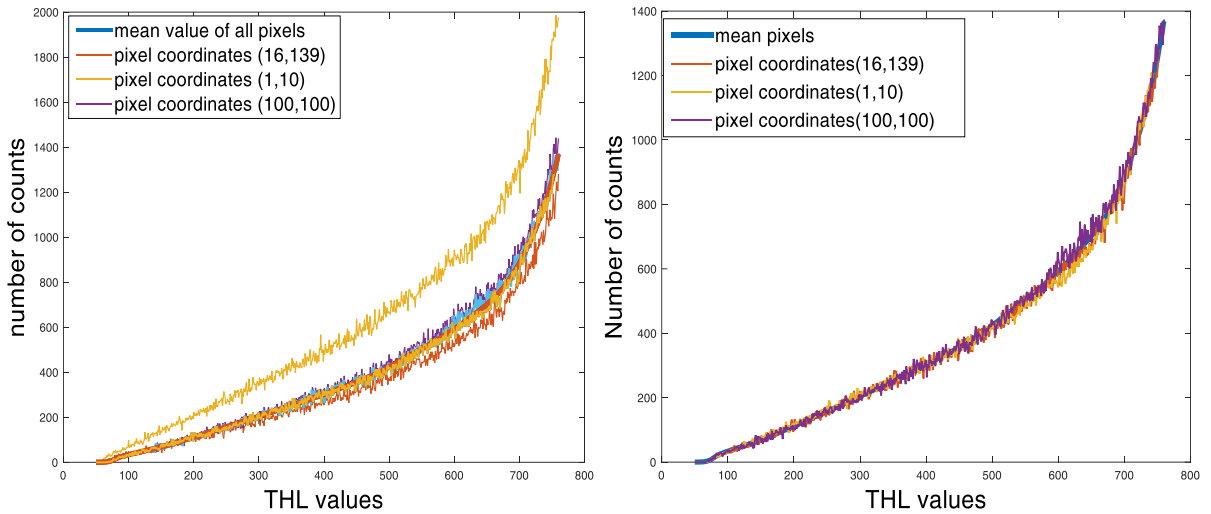


Figure 30. Left: integral THL scan spectrum for random pixels demonstrate the variance in offset and gain for each pixel. Right: matched THL scan spectrum for the same pixels to the mean pixels spectrum

Due to the mechanism of charge sharing, individual peaks in the spectrum need to be fitted by Gaussian + error function of identical mean ( $\mu_{\text{mean}}$ ) and standard deviation ( $\sigma$ ). The distribution of the resulting THL values ( $\mu$  from the fitting) throughout the detector is depicted in, Figure 31 (right). The distribution has a FWHM of 7.3 THL steps, with a long tail towards lower values, mainly corresponding to pixels in the periphery of the chip, Figure 32. Having obtained the 59.5 keV peak position for each pixel, the individual pixel's THL response is shifted to the mean position of this peak over all pixels. Figure 31 on the right shows the shift values. Fixing the position,  $\mu$ , of the peak fit to 59.5 keV, in a next step the THL response of all pixels is iteratively refined by re-scaling THL gain and pixel count normalization. The scaling factors obtained from the matching process is shown in Figure 31 on the right.



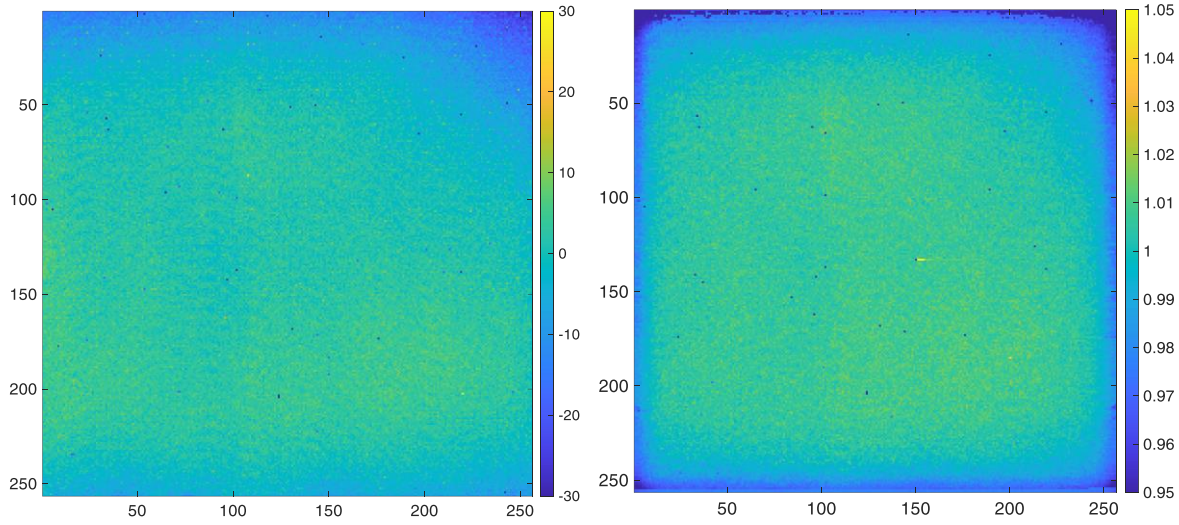


Figure 31. Correction factors obtained by the spectrum matching process. left: THL shift values relative to the mean value. right: scaling values obtained by the THL stretching process.

Using formulas (3.2) and (3.3) the correct per-pixel energy threshold  $E(i,j)$  at a given THL value is calculated:

$$E(i,j) = 59.54 - \frac{(THL - THL_{59.5keV}(i,j))}{M} \quad 3.2$$

$$THL_E(i,j) = THL_{59.5keV}(i,j) + \left( \frac{(59.54 - E(i,j)) \times M}{S(i,j)} \right) \quad 3.3$$

where  $THL$  is the threshold value set by Pixelman;  $THL_{59.5keV}(i,j)$  is the threshold value per pixel  $(i,j)$  at 59.5 keV determined by fitting;  $M$  is the mean Energy-THL slope calculated from the averaged THL scan of the two visible Am peaks (59.5 keV and 26.3 keV);  $S(i,j)$  is the relative Energy-THL slope per pixel calculated in the stretching step.

### 3.4.2 Assessment of stability of the proposed method

The THL-energy calibration of the detector was repeated using a number of different THL scan datasets, in order to analyze the stability of the method. All measurements were performed under standard laboratory conditions, at room temperature, acquiring ~400 k counts per pixel throughout each THL scan. As observed in Figure 32, left, the dispersion of THL values obtained appears to have Gaussian behavior, with a sigma of 7.3 THL steps (0.58 keV). A prominent tail towards lower THL values, mainly corresponding to pixels in the periphery of the detector, is well visible. Repetition of the fitting process using data from the independent measurements shows, that Besides a Gaussian distributed per pixel the variation of the peak width and position Figure 32 (right), also a total shift of the distribution between different THL scans is observed.

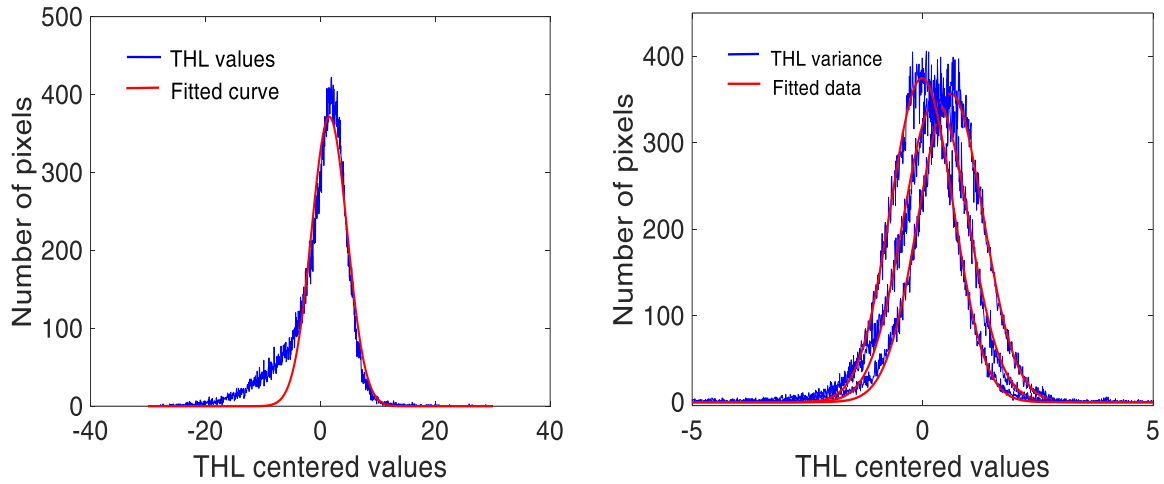


Figure 32. **Left** THL dispersion, centered around the mean THL value. The THL values at energy 59.5keV were determined by fitting and subtracted from the mean. **Right** THL variance between 4 sets of measurements. The 59.5keV peak positions of 3 datasets were subtracted from one reference dataset

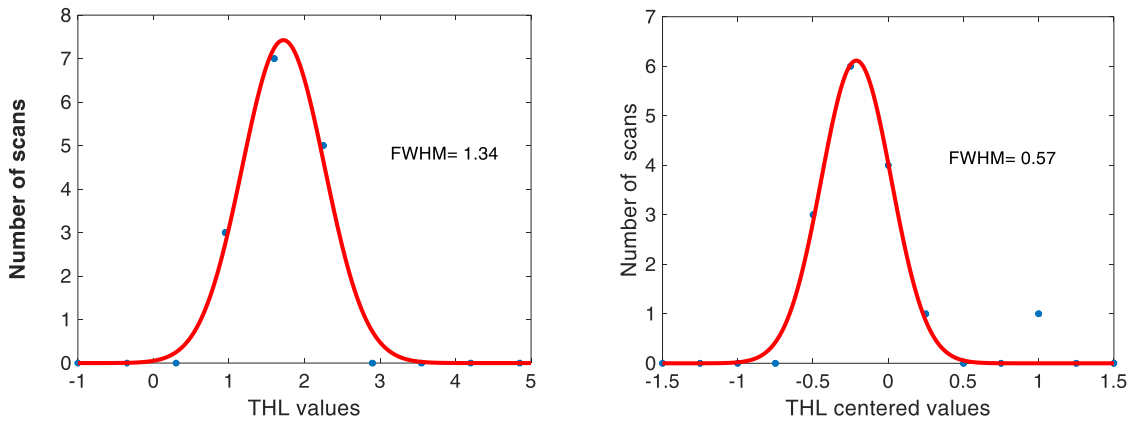


Figure 33. **Left**: Shift of the determined distribution mean over 15 independent measurements. **Right**: Peak width distribution over the same 15 THL scans.

In Figure 33 the shift of the distributions mean ( $\mu$ ) and the distribution width ( $\sigma$ ) over 15 independent measurements are histogrammed, using a bin width of .25 THL steps. We observe a normal distribution of both observables, which we will denote with *sys* (for systematic, meaning the shift of the entire distribution) and *rand* (width of the distribution) difference in between scans. Whereas the peak width is presumed to be owed to photon statistics, the FWHM of these two peaks are 0.57 THL for the *sys* and 1.34 for the *rand*, the shift of the entire distribution supposedly is owed to external factors like temperature change, sensor bias variation etc. The total error then calculates as follows:

$$\sigma_t = \sqrt{\sigma_{sys}^2 + \sigma_{rand}^2} = \sqrt{0.57^2 + 1.34^2} = 1.45 \text{ THL} = 0.12 \text{ keV}$$

### 3.5 Energy-threshold per pixel calibration using multiple mono-energetic sources

To reference the method described above a comparative calibration using a set of 2 additional mono-energetic sources was performed on the same detector. Here a linear fit, using Cu and Zr fluorescence in addition to the Am-241 source, was used to determine the per pixel THL-energy response. To this end, an Amptek mini-X tube was aimed at fluorescent targets, Cu at 25 kVp and Zr at 40 kVp, placed in front of the detector. The respective fluorescences were fitted by Gaussian + Error function. The distributions of resulting  $\mu$  values are given in (Zr on the left, Cu on the right).

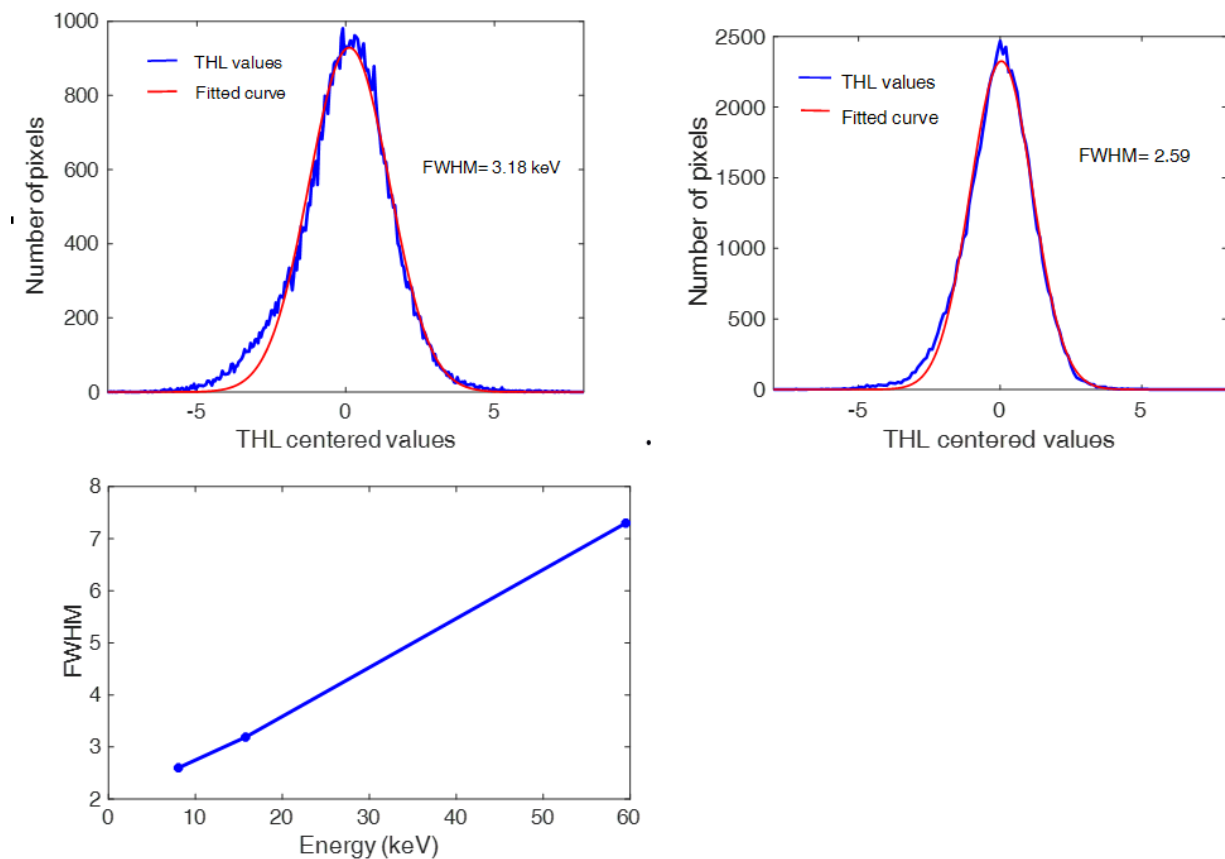


Figure 34. left THL centered values distribution for Zr X-ray fluorescence at 15.77 keV, the peak was fitted with Gaussian and the FWHM is 3.18 THL, right THL centered values distribution for Cu X-ray fluorescence, the peak was fitted with Gaussian and the FWHM is 2.6 at 8.03 keV, bottom: FWHM of threshold values distribution shows that threshold variance increases far away from the noise edge.

Since the detector was equalized to the noise edge it is expected that the width  $\sigma$  of the THL distribution will increase linearly at high energy thresholds. In the proximity of the equalization point however, due to the granularity of the adjustment bit settings, resulting in pixels being placed slightly below or above the mean calibrated energy, this behavior is non-linear. This behavior is observed in the plot in (bottom), which displays the width of  $\mu$  distributions at the respective

calibration points. In order to obtain a THL-Energy calibration, a linear fit of each pixels response was performed using the fluorescences of Cu at 8.04 keV, Zr at 15.77 keV as well as the Am-241 at 59.5keV peak. The THL-Energy response of some representative pixels are shown in Figure 35.

### 3.6 Comparison of the calibration results and application to imaging data

The calibrations results obtained by spectrum matching and fluorescence calibration were verified performing a THL scan over the Cd fluorescence peaks at  $k_{\alpha 1}=23.173$  keV,  $k_{\alpha 2}=22.98$  keV, and  $k_{\beta 1}=26.09$  keV. As can be seen in Figure 36, the  $k_{\alpha 1}$  &  $k_{\alpha 2}$  are not resolved, however the  $k_{\beta 1}$  is well discriminated from the latter. Using any of the previous two calibration methods (green or blue line) we obtain a much better resolved spectrum than without THL-Energy calibration (red line). Table 4 displays the fit parameters of the 2 peaks for the respective calibration methods.

Table 4. Parameters obtained from the fitting of Cd spectrum for raw and corrected data

		Raw data	calibration points method	matching method
<b>First peak</b>	Amplitude(count)	21.95	26.34	24.55
	FWHM(keV)	1.14	0.94	0.95
	Position(keV)	23.26	23.27	23.24
<b>Second peak</b>	Amplitude(count)	4.30	5.07	4.7
	FWHM(keV)	1.22	1.07	1.09
	Position(keV)	26.19	26.28	26.25

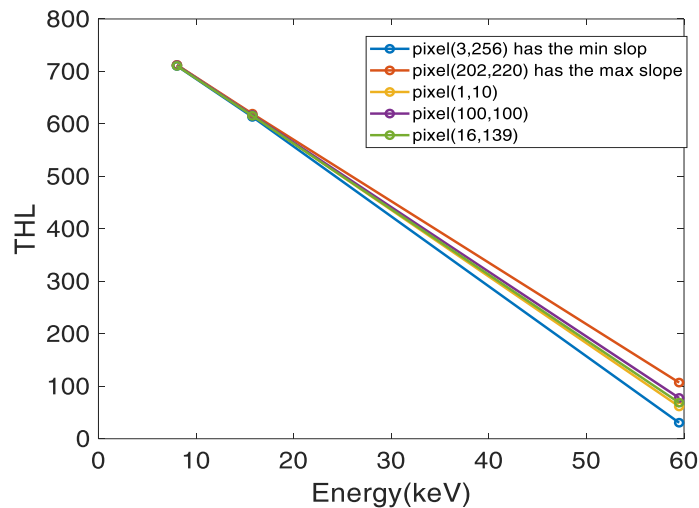


Figure 35: Energy-THL calibration obtained from 3 points (Am, Zr, and Cu) for some representative pixels

Whereas the peak positions hardly deviate for any of the data, the FWHM of the peaks are about 15–20% better for the data corrected by the calibration methods compared to the uncorrected data, which in terms of image contrast is a vast difference, Figure 37 shows the separated components (Gaussian and error function) of the spectrum corrected by the matching method.

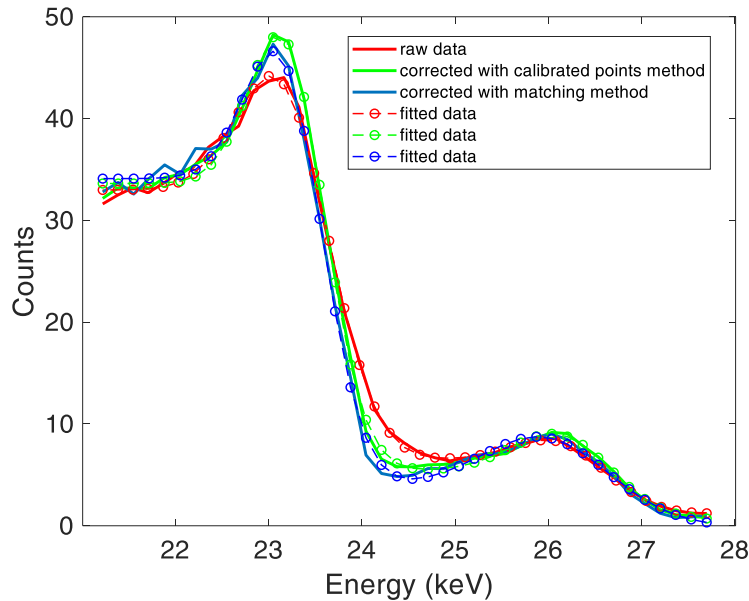


Figure 36: X-ray fluorescence of Cd, the figure shows differential THL scan in energy for raw and energy corrected data using both methods described above. The fitting of these two peaks was done separately, using Gaussian plus Error function, as illustrated in figure 10. All fitting parameters are included in the Table 4.

The energy correction obtained by the methods described above can be integrated to acquire spectroscopic image in a number of ways. The straightforward method is to perform a short THL scan around the desired edge of an energy bin and correct for the acquired count-rates by 1st or higher order or spline interpolation, which is faster and easier comparing with the measurements in TOT mode which consume a lot of time for having high statistics images.

### 3.7 Conclusion remarks

The presented methods precisely described the THL-Energy calibrations for Timepix type hybrid pixel detectors, operated in photon counting mode. Due to the inherent influence of charge sharing, if single clusters cannot be identified due to high flux or exposure time, this calibration modality is inherently more problematic than standard TOT calibration, which is usually applied for Timepix type detectors [41]. In particular charge sharing adds additional background to the measured differential spectra, rendering multi-peak fitting within complex spectra difficult and inaccurate [43].

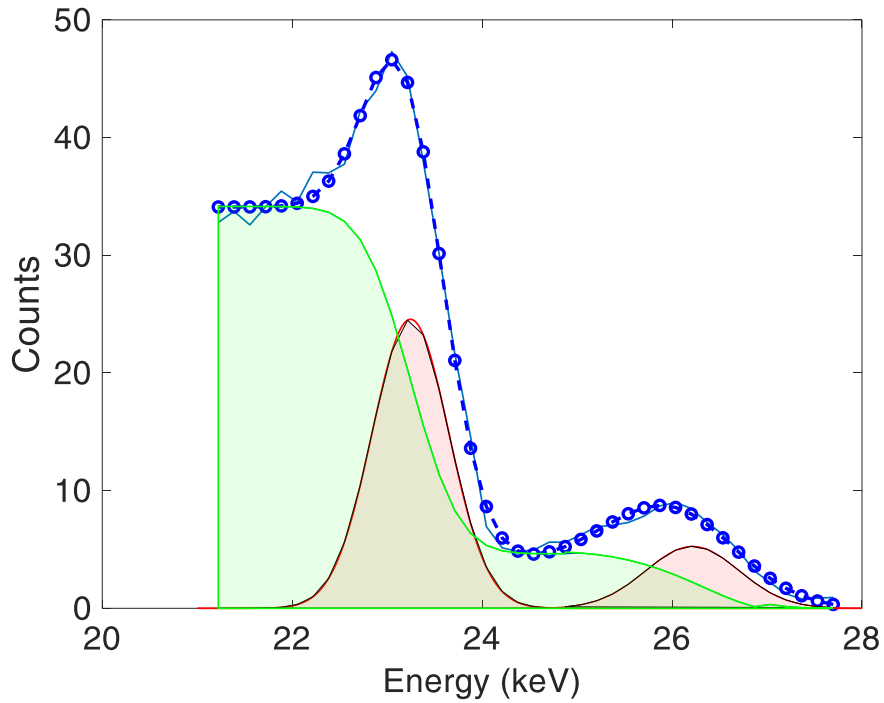


Figure 37: Separated Gaussian (red area) and error function (green area) components of cadmium spectrum corrected by the matching method. The sum of all components is shown in blue.

Two calibration methods were evaluated in this chapter. A straightforward approach, the calibration point's method, is based on the acquisition of multiple single-peak THL scans and linear fit of the resulting calibration points. This method works well due to the fact that the respective peaks to be fitted are not affected by charge sharing from higher energy contributions. The second method presented, instead of fitting single peaks, attempts to find THL gain and offset of individual pixels by spectrum matching, using shift and scale operations on the full THL spectrum acquired. Compared to each other, the calibration point's method gives only slightly better results than the spectrum matching. However, this minor improvement comes at the price of multiple THL fluorescence measurements, entailing multiple fitting procedures. Also, to modify the range of calibration points, one needs to find and mount adequate fluorescence targets for calibration. In case of the spectrum matching method, one can simply use a single mono-energetic peak plus an arbitrary X-ray spectrum. Therefore the spectrum matching method, having very comparable performance to the calibration point's method, provides an easier to handle and faster calibration of hybrid pixel detectors operated in counting mode. The above mentioned methods are applicable on silicon sensors of thickness 1 mm or above. The application of these methods on CdTe sensors will be possible in the future when polarization issues can be minimized [38].

## **4 Material decomposition based on multi-bin X-ray imaging**

This chapter presents spectroscopic X-ray measurement using Timepix large area photon-counting detector. The goal is to distinguish between different materials due to their response to photon energy by utilizing the advanced features of the detector with proper methods. To achieve that, an incident X-ray tube spectrum was split into three bins (energy channels) utilizing the detector energy threshold function. Then, the object under examination was tomographically reconstructed for each energy bin separately. The reconstructed volumes were subtracted from each other giving us three volumes of three different energy bins. RGB coding was assigned to the volumes providing us with a 3D colored volume approximation with respect to the material composition. The results of this work were presented at the University of Upper Austria as part of a contribution to the International Computed Tomography Conference [44].

### **4.1 Basics of spectral imaging**

Spectral X-ray imaging has been used for decades as a useful technique for material resolution "material resolving". The concept behind this technique is generated from the energy dependence of the attenuation coefficient for different elements in the X-ray range. This can be expressed in the Beer-Lambert law describing the linear attenuation of x-ray photons through a homogeneous medium. As the generated spectra of X-ray sources are polychromatic in nature, photons with different energies are attenuated differently when they pass through an object. As a result, the attenuated X-ray spectra carry information about the materials inside the scanned object. Such energy information can be useful only if it is registered by energy-sensitive detectors. Therefore, energy information encoded in the data from energy-sensitive detectors can be used to measure features in the image that can be correlated with the presence of a specific element or material in the object [14]. The energy response can be partially exploited using single event analysis of photon counting detectors or dual-energy computed tomography (DECT) with EIDs. However photon-counting detectors not only exceeded DECT of integrating detectors but also provide faster measurements with more precise results [45] [46]. Photon-counting detectors can measure the energy response using single-event analysis or by adjusting the threshold of the detector. Single event analysis is not suitable for CT measurements because creating a single frame/image is time consuming. Therefore, measurements was made using threshold adjustment in the form of multi-bin X-ray imaging.

### **4.2 Multi-bin X-ray imaging based on Timepix detectors**

One of the unique properties of Timepix detectors is spectroscopic performance utilizing the programmable threshold value of the discriminator in the pixel logic. The principle is simple, a preset threshold value controls the registered signal; in other words, the registered energy photons. Since the amount of charge released in the sensor by the photoelectric effect is proportional to the photon energy, the signal height is proportional to the photon energy as well. Therefore, Timepix detectors provide a selection of the photon energy using the threshold parameter.

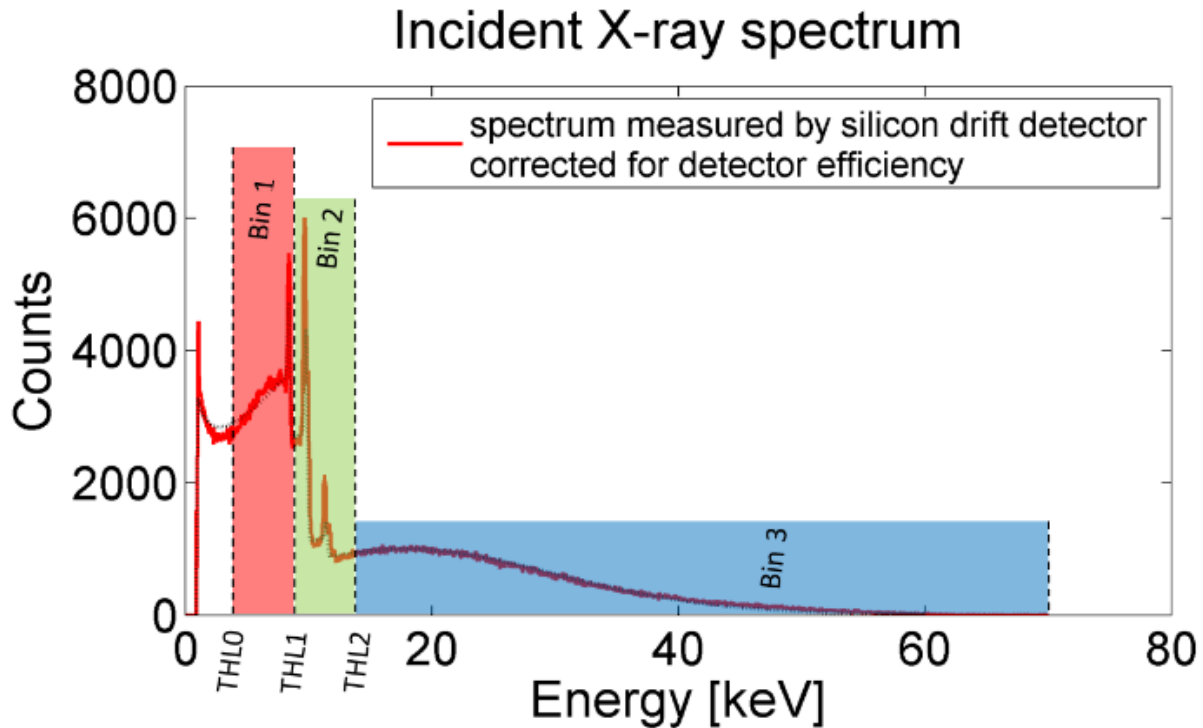


Figure 38: Illustration of energy sensitive counting approach, several energy bins are selected by subtracting integral images taken with different thresholds. The underlay spectrum of FXE-160.51 X-ray tube was recorded with silicon drift detector [13].

In practical use, the threshold value for Timepix detectors can be set using the operating software. By setting the threshold to a certain value, only pixels with signals higher than the threshold are counted; therefore, acquiring images at different threshold values provides different images in terms of the exploited energy spectra. Figure 38 presents an X-ray spectrum divided into three energy bins by subtracting integral images with different thresholds. Due to splitting the spectrum into different energy bins, the spectral X-ray term is replaced by multi-bin X-ray. With this approach, the contrast of different attenuation materials in the sample changes as a consequence of the different energy dependence of the respective photon attenuation. Figure 39 shows that two images for a tracking device were taken at two different threshold values, 7 keV and 16 keV, where the contrast changes between different materials are noticeable. The images were acquired using WidePIX<sub>4x5</sub> installed at IEAP laboratories, which was mentioned in the previous chapter. Such a feature (changing the threshold) does not exist in conventional energy-integrating detectors, where the spectral information is lost.



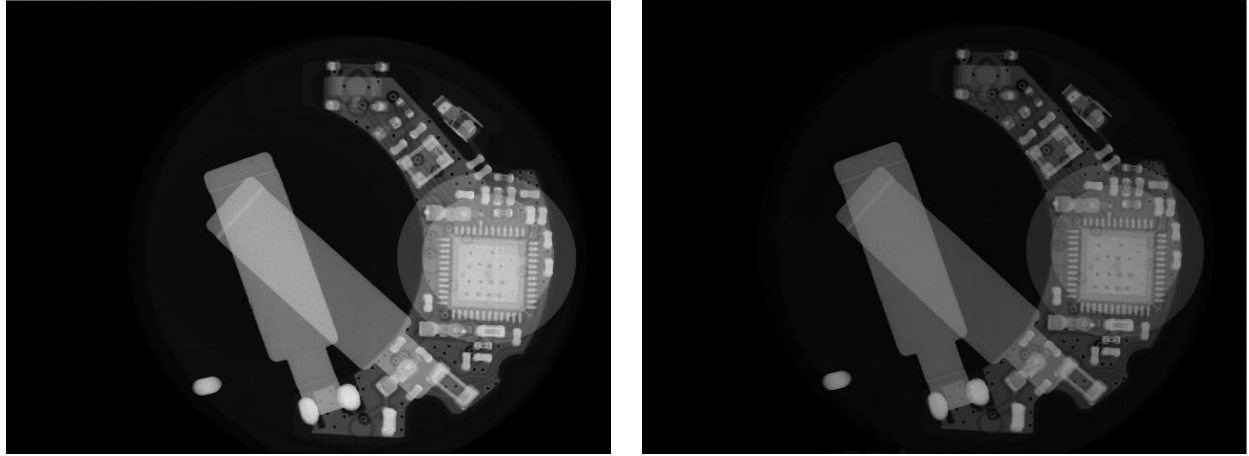


Figure 39: X-ray images of a tracking device, the images were beam hardening corrected, Left: at THL 7 keV, right: at 16 keV.

### 4.3 Materials and experimental setup

Measurements were made using the micro-CT setup with the large-area photon detector (WidePIX<sub>4×5</sub>). The WidePIX<sub>4×5</sub>, previously studied, consists of 4 rows and 5 columns of TimePix chips with 500 μm thick endless silicon sensors. The total resolution of the detector is 1280×1024 pixels (1.3 megapixels). The detector was calibrated using the standard threshold energy calibration method presented in the previous chapter, where the chips that make up the detector are calibrated individually. Due to the low efficiency of silicon sensors with a thickness of 500 μm, the energy bins were chosen in the effective detection range of the sensor, i.e., below 20 keV. Therefore, it was not necessary to apply the new correction methods, which showed improvements at high energy thresholds far from the noise edge (i.e., the methods are effective when the detected photons have energies higher than 30 keV).



Figure 40. Tracking device used for the purpose of material decomposition using multi-bin X-ray tomography.

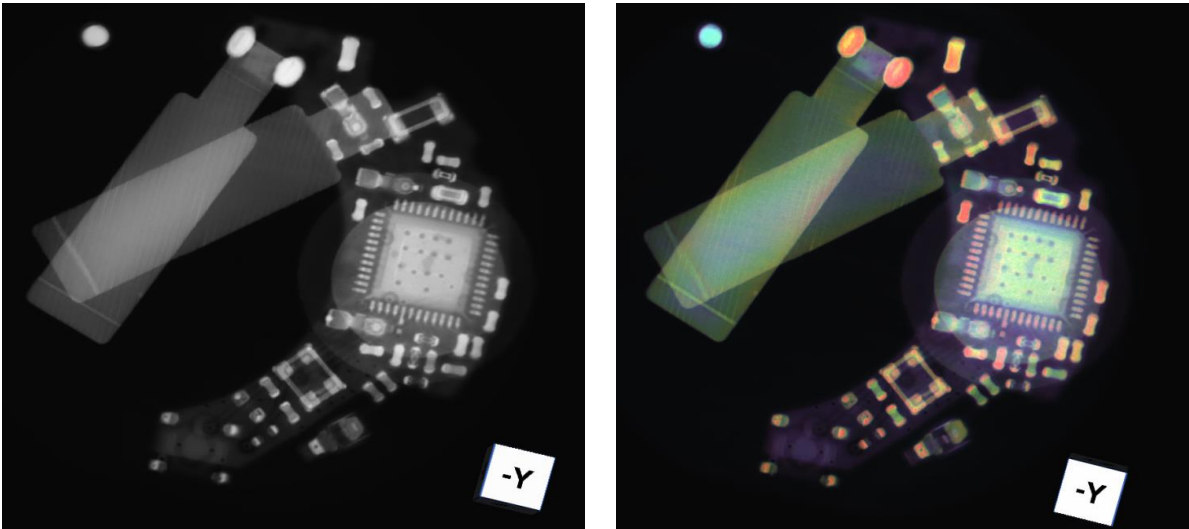
An electronic tracking device was chosen to verify material decomposition by multi-bin X-ray computed tomography, Figure 40. The device consists of various electronic components made of different attenuated materials that can be distinguished using the spectroscopic performance of the

Timepix detectors. The device was chosen to fit the FOV of the detector and to have adequate projection statistics in the selected X-ray spectra to obtain reconstructed volumes with less noise.

#### 4.4 Dataset and results

The tracking device was scanned with the FienFocus tube (FXE-160.51) operated at 70 kV and 60  $\mu$ A. Three sets of data were acquired at three different thresholds: 7, 12, and 16 keV. We chose these values to enhance the material contrast by utilizing the energy response of the materials. However, due to the low detection efficiency of the silicon sensor, 16keV threshold was set as the high-energy bin. The chosen thresholds corresponded to three energy bins: 7-70keV, 12-70keV, and 16-70keV.

Each full scan ( $360^\circ$ ) consists of only 120 projections. The projections were corrected using the beam hardening correction method, which is helpful to reduce the beam hardening artifacts [3]. For reconstruction, each data set was reconstructed with a voxel size of 40  $\mu$ m and using the developed iterative algorithm based on ML-EM (Maximum Likelihood Expectation Maximization). The reconstructed volumes were then subtracted from each other to obtain two differential volumes for two different energy bins. In order to visualize different materials in different color coding, we assigned the RGB coding to the differential volumes. Thus, the first differential volume represents voxels of the 7-12 keV energy bin and was shown in **red**, and the second differential volume for the 12-16 keV energy bin was shown in **green**. The third volume for the 16-70 keV energy bin was shown in **blue**. By composing the multi-bins volumes together, we obtained a colored volume for the tracking device in which different materials (components) are colored in different colors.



*Figure 41: Rendering images of the reconstructed volume of the tracking device. Left) Conventional tomography, where information energy is not exploited. Right) Multi-bin computed tomography, where the energy information is exploited, and different materials are colored with different colors.*

Figure 41 shows rendering images of conventional and colored volumes for comparison. As is well known, conventional tomography uses a grayscale representation to show the estimated CT numbers without using spectral information. Therefore, the difference in gray values between two different parts (materials) of the reconstructed volume is not sufficient evidence for two different attenuation materials. Conventional tomography can also be presented in a color coding other than the gray scale coding, but this color coding is a false coding. The spectral information of the multi-bin approach can be seen in Figure 41 (right), where the different components of the different materials are colored with different colors. The colored volume shows not only pure red, green, and blue colors, some components are also assigned to mixed colors from the three coded colors. The multi-bin approach works better for materials with high Z-values or materials with k-edges in the selected energy bins. For example, capacitors and oscillators contain copper with a k-edge at 8.98 keV, which is in the first differential energy region. Therefore, these components can be easily distinguished with the colored X-ray image, Figure 42. Two types of capacitors are shown in Figure 42. The first type is encapsulated with a copper layer, while the second type contains a barrier layer of Ni at the edges. However, copper encapsulated capacitors are coded red in the colored volume, while the second type of capacitor is coded green, with red edges where the nickel is present. Both copper and nickel have close atomic numbers (29 and 28, respectively), so they are colored red because it is difficult to separate them based on attenuation properties. Lightweight materials such as IC components and printed circuit board (commonly made of low Z materials) have lower attenuation factors and are coded blue because they are mainly represented by the third energy bin.

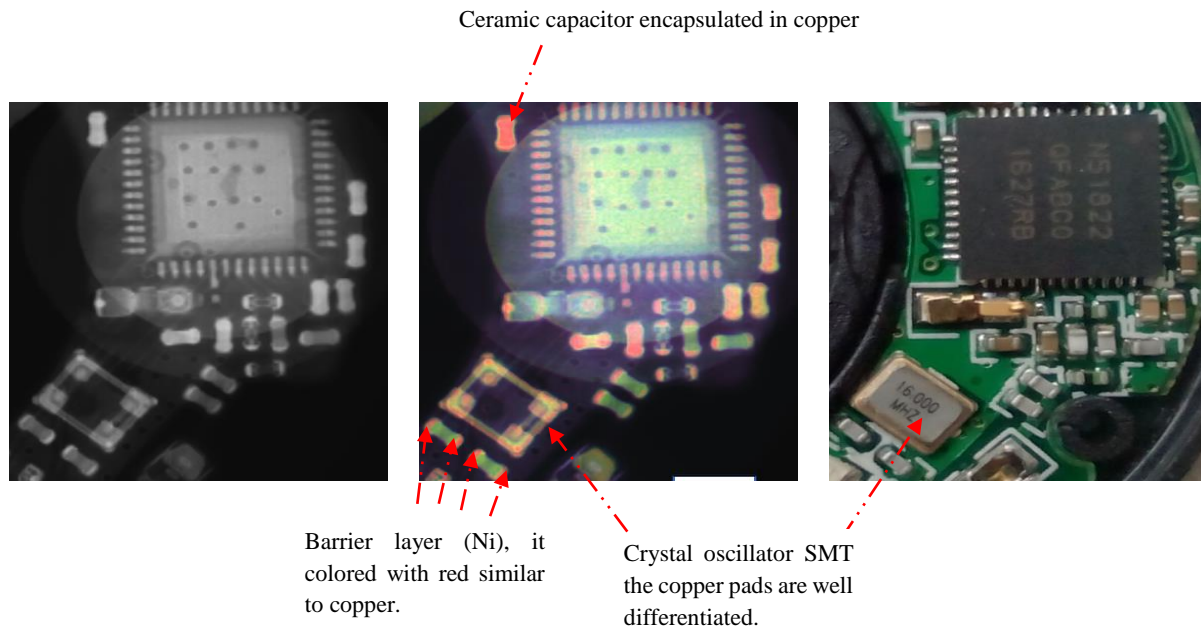


Figure 42: Illustration of material differentiation based on multi-bin tomography. Left) conventional CT, middle) multi-bin CT, right) enlarged photograph of the imaged components.

The conventional volume, which does not exploit the energy information, presents all the components with gray. The presence of materials with certain property of color shade in the colored volumes are difficult to be recognized in the conventional CT, Figure 42.

#### **4.5 Conclusion remarks**

Despite its success, this approach is not sufficient for highly attenuated materials due to the limitations of the silicon detector, such the low efficiency of silicon which requires the use of low energy spectra. To implement this approach efficiently, a high-Z detector should be used with the possibility of using energy thresholds higher than 16 keV. Cadmium tellurite sensors are already available for use in large area detectors. However, they are still imperfect due to the polarization phenomenon of the sensor, which causes defects to occur [47]. With a proper photon-counting detector (large area with a high Z sensor) this approach can be used to separate different materials of different components for selective of biological and industrial samples [44].

## **5 Inspection of epoxy underfill utilizing X-ray imaging techniques**

This chapter presents the inspection of defects associated with an underfill process for microelectronic devices that use ball grid arrays as interconnects between ICs and PCBs. The defects appear in the form of excess epoxy, the underfill material, on the surface of various components of the PCBs, especially the ICs. Our objective is to verify the presence of an epoxy underfill layer at the IC and above the PCB. For the investigation, we tried to find the optimal X-ray technique, which can be performed with standard X-ray setups without special equipment. The samples under study contain a large amount of metals that cause artifacts in standard computed tomography. However, at the beginning of the study, conventional computed tomography was obtained for the studied sample to check the effects of metal artifacts on the representation of the underfill material. We used metal artifact reduction algorithms (MAR) to correct the artifacts created, and we also tested the dual-energy computed tomography (DECT) and rotary laminography approaches. The aforementioned approaches were not able to help correct the artifacts created, which interfere with the epoxy underfill layer and lead to misinterpretations regarding the epoxy distribution between the BGAs. However, these approaches are presented in this chapter as an introduction to the use of Data Fusion of Multiposition Computed Tomography (DFMCT) as an effective alternative for studying such samples. The data fusion approach will be explored in detail in the next chapter.

### **5.1 Ball grid array packaging**

In recent decades, there has been a great demand in the microelectronics industry for miniaturization with higher functionality and lower prices. Stacking multiple dies such as IC, semiconductor devices, printed circuit boards, and wafers on top of each other to form 3D packaging has been a solution to this trend. As a result, verification of reliability and defects generated has become more complicated, especially with non-destructive testing methods. Ball grid array (BGA) packages play an important role in the downsizing of electronic devices and cell phones, as they are used to mount ICs on the surface of printed circuit boards. The BGA consists of tiny solder balls arranged in a grid pattern to conduct current between IC and the PCB. Figure 43 shows a BGA pattern used to connect IC and BCP. The arrangement of the balls in the pattern is determined by the manufacturer based on the interconnection criteria. X-ray tomography was used to visualize the BGA of the samples presented in Figure 43. While the image on the right shows voids within the spheres that are considered defects, the image on the left shows the pads used to connect the BGA to the PCB.

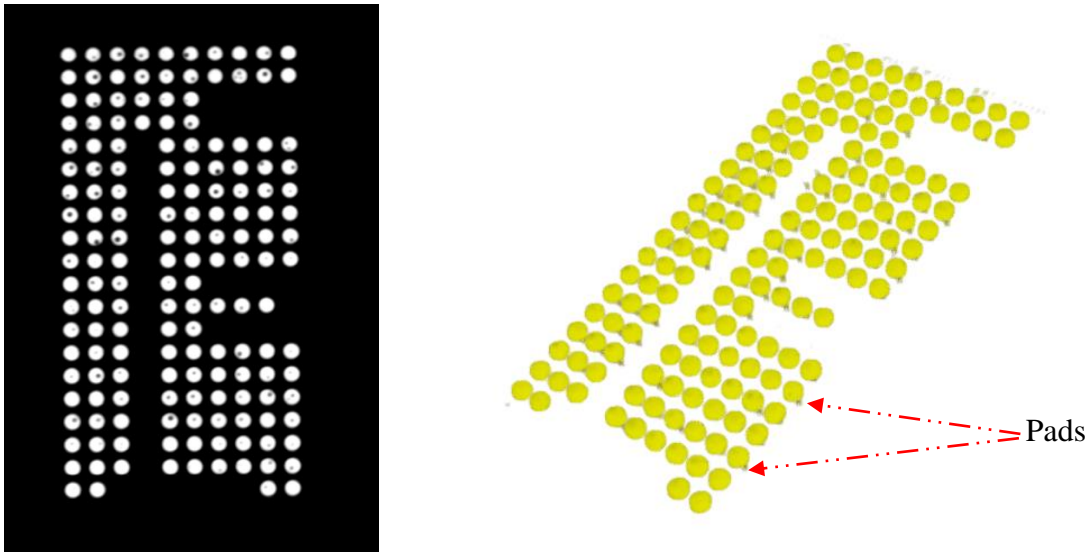


Figure 43: BGA pattern made of 162 spheres with a total length of 10.6 mm×8 mm. Left) Slice from computed tomography, the air voids inside the spheres are visible. Right) 3D tomography of the BGA, pads are visible for some spheres.

## 5.2 Epoxy underfill technique

To increase the reliability of BGAs under mechanical and thermal stress, the spheres are encapsulated with a polymer or liquid epoxy (underfilling technique). The underfill material is applied along one or more edges of the IC to fill the space between the PCB and the bottom of the chip by capillary forces. The process begins by preheating the circuit boards to facilitate flow of the underfill material under the chip. After the preheating phase, the underfill is applied to the bottom edges of the chip, which flows through the capillary forces, Figure 44.

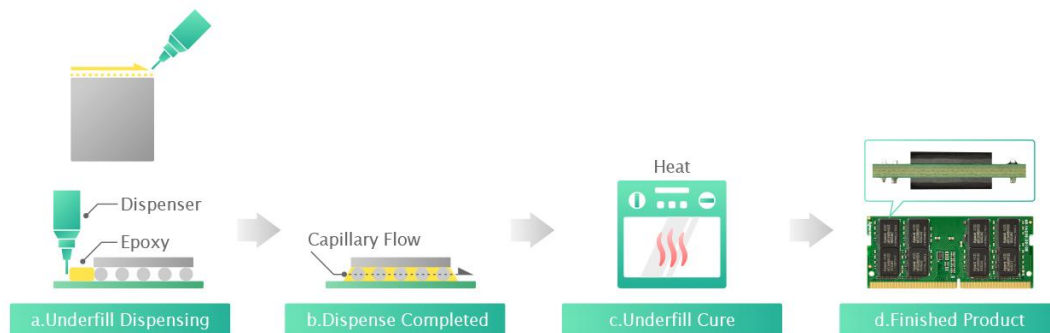


Figure 44: Mechanisms of epoxy underfilling [48].

The manufacturing process in which the underfill is applied is usually determined by the manufacturer to achieve the best properties. Depending on the number of edges involved in the process, some dispensing patterns are introduced, such as I pattern (one edge), L pattern (two edges) or U pattern (three edges). Accurate execution of the underfill is a major challenge because

there are various components next to be ICs which may affect the movement of the jetting pumps. Other factors such as the techniques used, the size of the spheres and the properties of the underfill material also influence the underfilling process [49].

### **5.3 Standards for evaluating the underfilling process**

The criteria for successful underfilling were established in the Manual for the Selection and Application of Underfill Materials at the Printed Circuit Board Level (IPC J- STD -030A). It states that underfill should fill the area under the chip and cover at least 50% of the height of the chip along the edges. However, process validation and control are still critical, as the integrity of the resin deposits has a direct impact on the efficiency of the underfill [50]. Reliability can be compromised in the event of poor adhesion or voids in the underfill resin [50]. However, the major disadvantages of underfilling are incomplete (partial) filling, voids, and excess underfill on the chip surface [51].

### **5.4 Nondestructive techniques to control the quality of the underfill process**

In recent decades, few nondestructive techniques have been introduced to control the integrity of underfilled assemblies, such as visual inspection, X-ray imaging, and scanning acoustic microscopy (SAM). The visual inspection technique is very limited since only excess epoxy defects can be detected; defects associated with partial fills or voids cannot be inspected. On the other hand, X-ray imaging technique has been consistently reported as inadequate for inspection of underfill defects because the CT reconstruction algorithms produce artifacts [50] [52] [53].

The scanning acoustic microscope has been introduced as a solution for the inspection of underfill defects [50] [51]. Basically, acoustic analysis uses high frequency ultrasonic waves to detect defects related to the presence of air, such as porosity, voids, cracks or delaminations [50]. This technique can be used in two different modes: C-scan and Through-scan mode. However, both modes have problems, such as lower signal-to-noise ratio and uncertainty about the specific depth encompassed by the data [51]. In general, the technique SAM, especially the C-scan mode, is inadequate for multilayer PCBs separated by fiber optic layers because attenuation prevents a clear echo from direct reflection. However, with SAM in through-scan mode, it is possible to detect large defects, but only with low resolution [50].

In this work, we will focus on using new approaches to advance radiographic techniques for such studies.

### **5.5 Epoxy underfill defects for power supply devices**

In this section, we investigate the epoxy underfill process for power supply devices. The manufacturing company of these devices prefers to remain anonymous, but we have obtained large circuit boards of these devices from the Faculty of Electrical Engineering of the Czech Technical University. Each board contains several electronic components such as capacitors, resistors, and ICs mounted on the surface of the boards, Figure 45 (A). Excess epoxy defects can also be seen on the top surface of the ICs, causing the entire board to no longer meet PCB standards. Therefore,

a non-destructive technique was required to investigate the presence of epoxy under the ICs and to establish a relationship between the excess epoxy defects and the underfilling epoxy. X-ray radiography measurements for the entire PCB are possible with the equipment installed in the IEAP CT. However, this type of measurement does not provide adequate information about the internal structure of the objects under investigation, so computed tomography measurement is required. The PCB consists of copper layers connected by glass fibers with total thickness of ~3 mm. CT for the whole board is limited with CT equipment equipped with X-ray sources of limited power, due to the high content of metals that absorb the whole applied X-ray spectrum. To simplify the problem, a small portion of the board containing IC with excess epoxy on top was selected for the CT. Therefore, a simple cutting process was performed with standard tools to reduce the size of the studied PCB, Figure 45 (right).

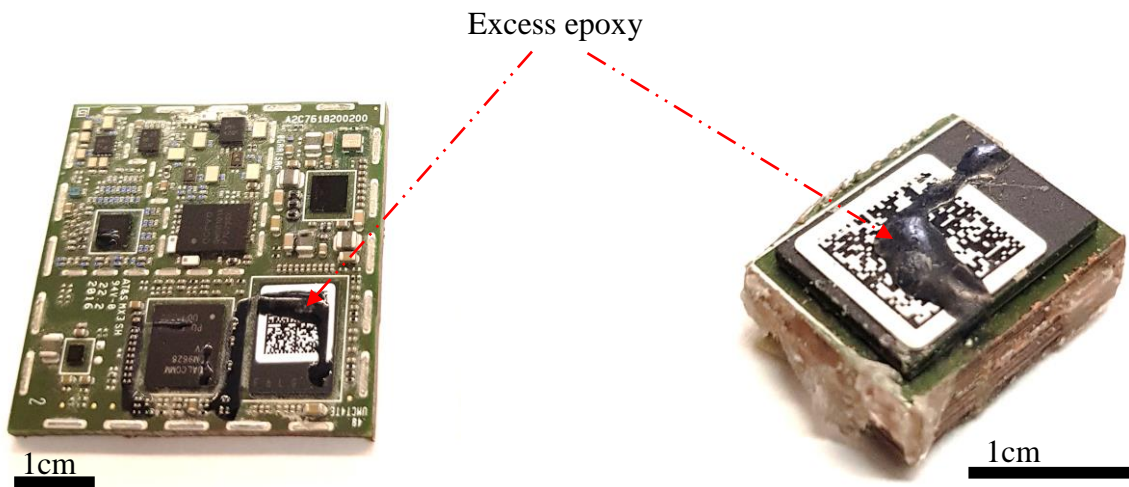


Figure 45. Left PCB with several ICs, capacitors and resistors mounted. Excess epoxy defects are visible on the top of some ICs. Right) Enlarged a small portion of the board (cut sample) is prepared for measurement from CT.

The cut sample contains several copper layers that form the PCB with a total thickness of 3 mm; the other two dimensions are 12 mm×7 mm, the IC is mounted on the top with a BGA. The BGA pattern is rectangular and not completely filled with spheres, Figure 43. The diameter of each sphere is ~400 μm and the center-to-center distance between spheres is ~800 μm. The BGA is made of lead-free tin Sn ( $Z = 50$ ), which has a high attenuation coefficient for X-rays. The maximum number of spheres in a row can be up to 20, depending on the orientation of the sample on the rotation stage. When the specimen is mounted in such an orientation, the transmission length within the tin material is ~ 8 mm, resulting in strong metal and beam hardening artifacts. The underfill material is an epoxy compound (type: LOCTITE ECCOBOND FP4531), which has a lower attenuation coefficient, especially for high energy photons. Detection of low attenuation material such as epoxy between BGAs is problematic because the contrast is reduced by the overlap of the epoxy and the resulting metal artifacts.



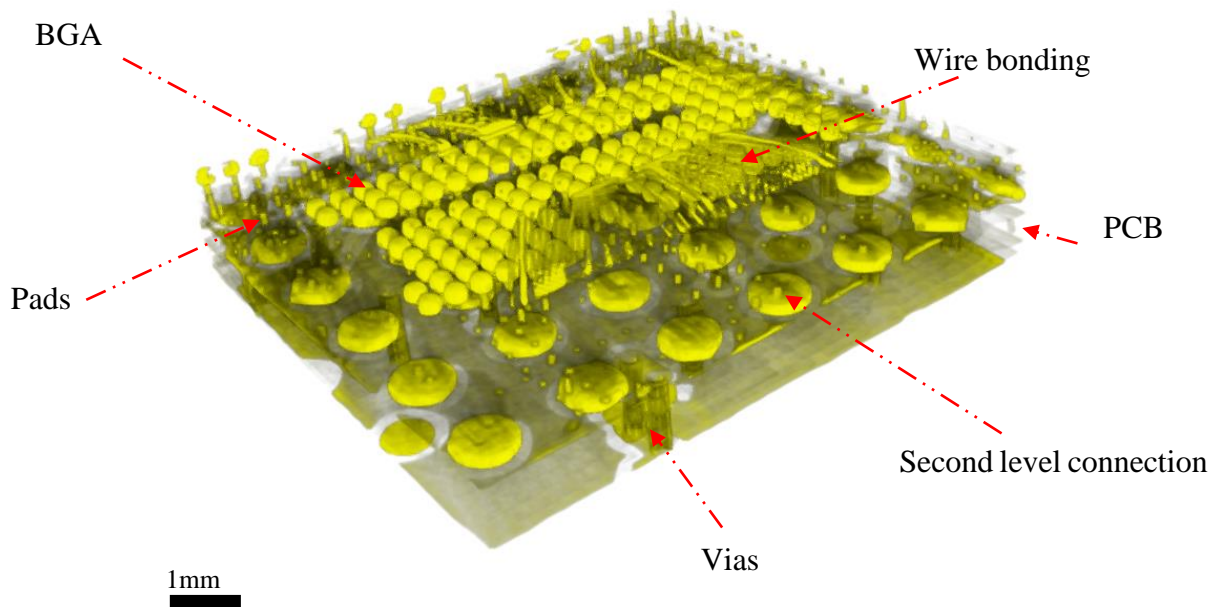


Figure 46: Tomography of the sample shows the high content of metals in the scanned sample.

### 5.5.1 Computed tomography parameters

A computed tomography scan of the sample was performed at 140 kV and 160  $\mu$ A using a 2 mm copper filter at magnification of 4.6 and Dexela detector. The total number of projections was 1800 with an exposure time of 350 ms for each projection. For reconstruction, we used the filtered back projection from VGSTUDIO MAX with cone beam geometry and Shepp-Logan filter [54]. The 3D tomography of the sample is shown in Figure 46 where the intensity color was modified to show the metallic parts inside the BGA sample that cause different types of artifacts. Selected slices of the reconstructed volume are also shown in Figure 47 to show the challenges in examining the underfilling epoxy with the standard CT. Slice A was taken between IC and the PCB where the BGA is located. The distribution of the underfill should be seen in slices at this level, so similar slices will be shown repeatedly later to investigate the underfilling epoxy. The slice reveal the existence of epoxy in a small region to the lower-right side of the BGA, this was verified by comparing the contrast of this region with the contrast of the excess epoxy defects detected in slice (B). However, verification of the epoxy distribution between the BGA and other parts of the chip is difficult due to the metal artifact streaks. Another slice of the reconstructed volume can be seen in Figure 47 (B). The slice was taken on the top of the IC where excess epoxy defects are located, from which information about the shape and contrast of the excess epoxy can be determined.

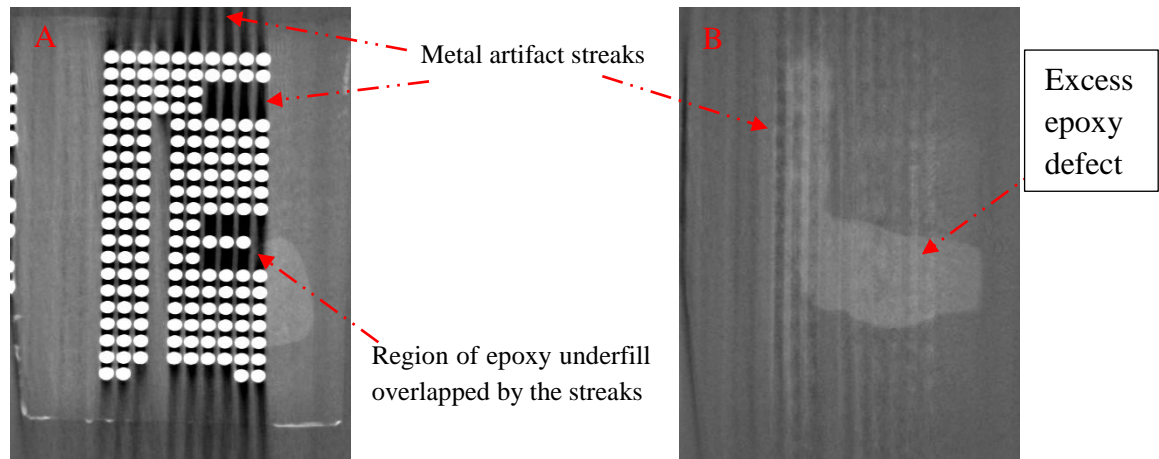


Figure 47: Slice of the reconstructed volume of sample 1. A) The slice shows the BGA, strong metal artifacts and the detected epoxy region to the right of the BGA. B) The slice shows the excess epoxy defect on the top of the IC.

Both slices show strong metal artifacts and beam hardening artifacts caused by the high metal content of the sample. The metal artifacts produced by the BGA appear as dark streaks whose intensity depends on the number of spheres facing the X-ray beam (slice A). The intensity of the streaks is high enough to disrupt the entire image and discard any information about the epoxy distribution in the region between the spheres. The streaks overlap with the detected epoxy region, resulting in reduced contrast compared to the surrounding air area, especially within the BGA region.

The effects of the metal artifact streaks and the beam hardening artifacts can also be seen in slice B as white and black streaks. The edges of the excess epoxy on the left side are disturbed by the overlap with the streaks, leading to a misinterpretation of the epoxy distribution. Since the overlap between the epoxy and the metal artifacts leads to a degradation of the contrast compared to the surrounding areas, we cannot evaluate the correct distribution of the epoxy, so we need to minimize the effects of the artifacts by using a suitable correction technique.

## 5.6 Measurement strategy

Due to the strong metal artifacts in the area of the underfilling epoxy, the examination should be optimized to obtain more useful information about the underfilling with lower artifacts. To achieve this, we had to test X-ray techniques that can be performed with a limited energy source, and then choose the most efficient approach to examine more BGA samples to reach a conclusion about the excess epoxy defects. Therefore, we will present our study as follows:

- 1- CT improvement by reducing noise in projection data
- 2- Reducing metal artifacts by reviewing different X-ray approaches
  - 1- Applying metal artifact reduction (MAR) algorithms
  - 2- Performing Laminography measurement

- 3- Performing a dual-energy computed tomography
- 4- Performing fusion data of multipositional computed tomography.

## 5.7 CT improvement by reducing noise in the projection data

### 5.7.1 Improving the contrast-to-noise ratio

Improving the quality of CT reconstruction mainly depends on the quality of scanned projection images. Therefore, selecting the scanning parameters that provide the best CT data should be done carefully. Noise is one of the parameters that affect the quality of the reconstruction, so it must be kept low in the projection images. Noise reduction can be achieved by enhancing the images acquired by the detector, later by using filters and specific CT corrections, such as flat field correction or beam hardening correction [10].

Image contrast depends on the applied X-ray voltages, since the voltage affects the energy of the emitted photons. Applying higher voltages produces a higher X-ray spectra and images with lower contrast. On the other hand, increasing the tube current increases the flux in the tube, which increases the number of photons hitting the detector. The higher the current, the higher the number of photons reaching the detector, which in turn reduces the quantum noise, the same applies for the integration time used to acquire an image. The standard deviation is equal to the square root of the number of registered photons [10].

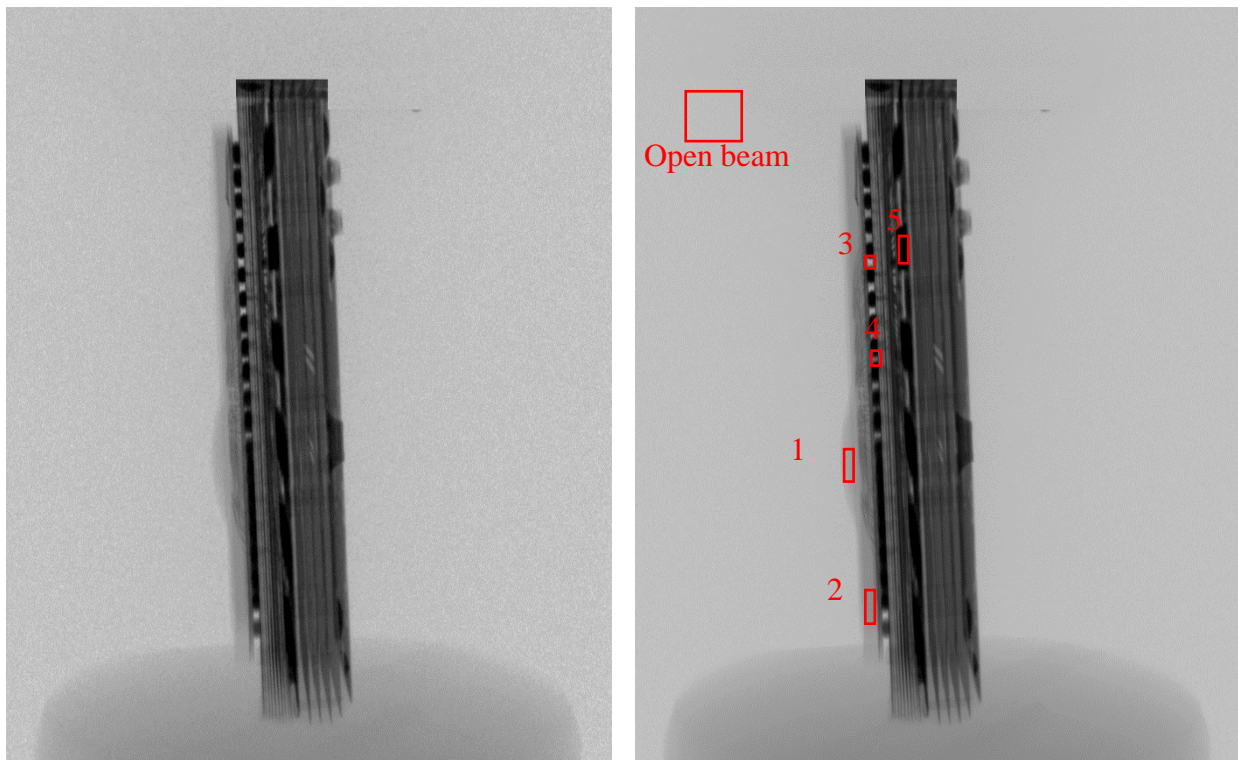


Figure 48: Projection image of BGA sample obtained by averaging different frames. Left) single frame, Right) 10 averaged frames.

Image averaging is used as a technique to reduce random noise because the fluctuations between pixels can be reduced by averaging multiple similar images. However, the scanned images/frames should be scanned under the same irradiation parameters to reduce noise [10]. To check the effect of image averaging on the quality of CT reconstruction, we had to collect several datasets for the BGA sample by averaging a different number of images. For this purpose, the Python script controlling the Dexela detector was modified to store projections of 1, 2, 4, 6, and 7 averaged frames at each rotation angle. A single complete scan for the sample therefore yielded 5 data sets, each obtained by averaging a different number of frames. By averaging multiple combinations of these data sets, we were able to obtain new data sets. For example, we summed the projection data sets of 4 averaged frames and 6 averaged frames to obtain a new data set of 10 averaged frames.

### 5.7.1.1 Evaluation of the projections

Figure 48 shows two projections for the sample obtained by averaging a different number of frames. The image on the left is a single frame, while the image on the right was obtained by averaging 10 frames. The noise in the projection obtained from a single frame is notable, especially in regions of open beam and light materials, Figure 48(left). However, the noise was remarkably reduced by averaging 10 frames, Figure 48 (right). Quantitatively, the standard deviation (SD) and contrast-to-noise ratio (CNR) parameters were calculated to address image enhancement. Different regions of interest (ROIs) were selected for the calculation Figure 48 (right). The open beam area was chosen as a reference for CNR calculation based on the CNR formula (5,1).

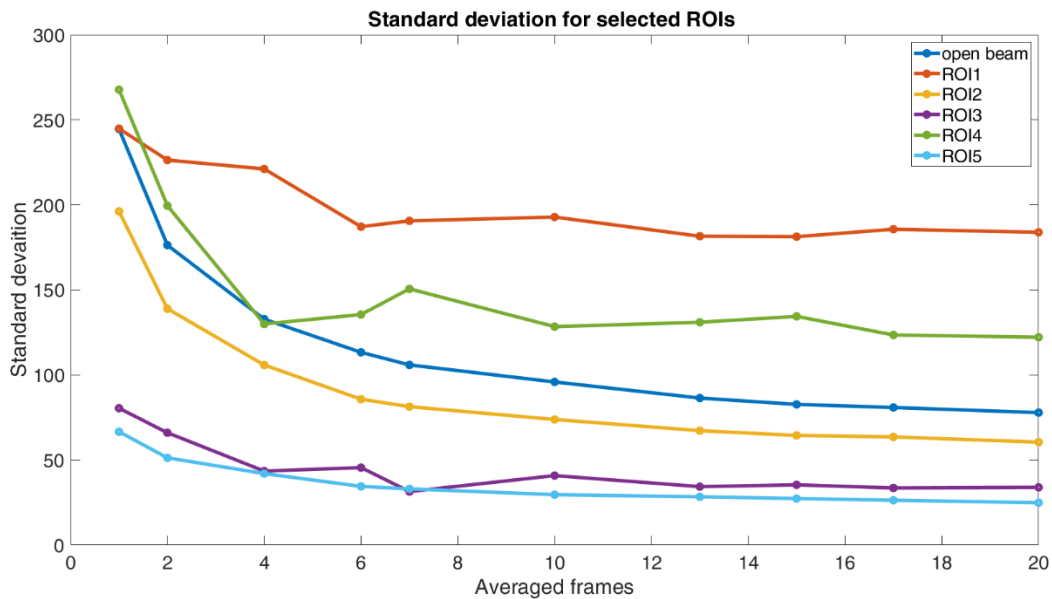


Figure 49. Standard deviation for the selected ROIs calculated at different number of averaged frames. SD values decrease with increasing number of averaged frames, after 6 averaged frames the decrease becomes small.

$$CNR = \frac{|I_a - I_b|}{\sqrt{\sigma_a^2 + \sigma_b^2}} \quad 5.1$$

Where  $I_a$  signal intensity for region of interest a,  $I_b$  signal intensity for open beam area,  $\sigma_a$  and  $\sigma_b$  are the standard deviations in these zones.

The calculated values of standard deviation (SD) for the selected ROIs (Figure 49) show the decrease of noise by increasing the number of averaged frames. For the selected ROIs, the standard deviation was reduced by 65% by averaging 6 frames. The reduction of noise becomes smaller after 6 averaged frames, for example, the noise can be reduced by only 7% by averaging 20 frames.

Although the standard deviation measures the signal improvement due to the reduction of noise, the calculation of the contrast-to-noise ratio (CNR) is a preferred criterion in the field of imaging. The calculated CNR values are shown in Figure 50. The curves show that the CNR increases as the number of averaged frames increases. After 6 averaged frames, the CNR increases only by 5%, especially for ROI1, ROI2 and ROI4.

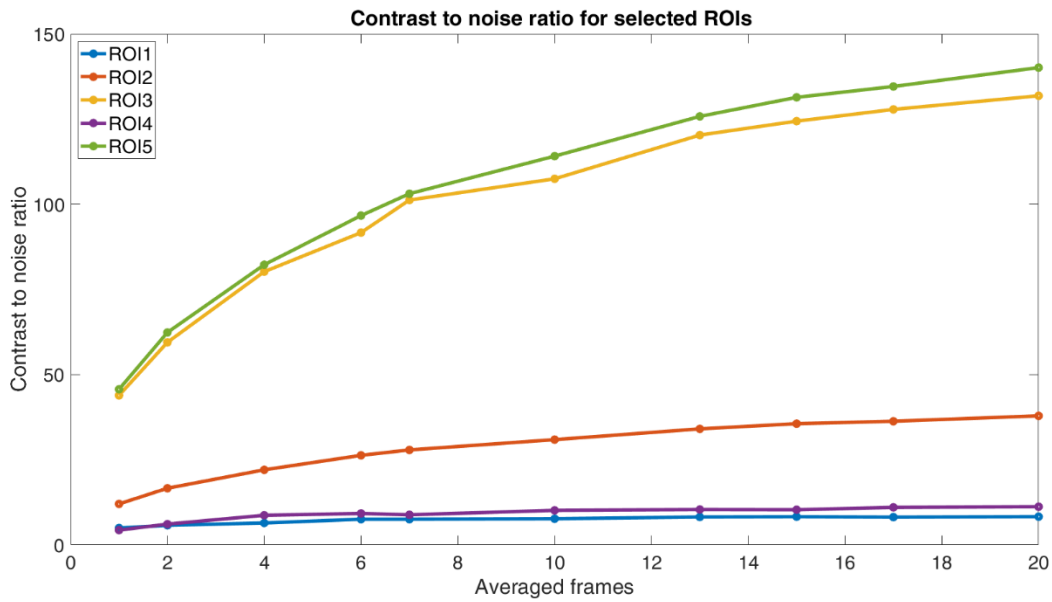


Figure 50. Changes in contrast-to-noise ratio compared to the air as a function of the number of averaged frames. Light materials (ROI1, ROI2, and ROI4) show improvement up to 6 averaged images, where the curves begin to flatten. On the other hand, heavy materials (ROI3 and ROI5) show a different behavior due to the low statistics caused by the high absorption of low energy photons

ROI3 and ROI5, which belong to the metal parts, show higher CNR values due to the lower standard deviations calculated in these regions. In order to verify the obtained results, the same calculations were performed with the reconstructed data sets in the next section.

### 5.7.1.2 Reconstruction evaluation

The projection data sets obtained from different averaging frames were reconstructed using the VGSTUDIO MAX software and the filtered back projection method. Figure 51 shows two slices of volumes reconstructed from the data set of a single frame (left) and from the data set of 10 averaged frames (right). The slices show the excess epoxy on top of the IC, the BGA, the printed circuit board, and the metal artifact streaks caused by the BGA, Figure 51. However, the noise level in the slice of the single frame volume is remarkable, especially in the area of the open beam surrounding the sample. The CNR between air and IC is low due to the high noise level, and the edge of IC can hardly be distinguished from the surrounding air, Figure 51 (left). On the other hand, the volume of 10 averaged frames has lower noise and higher contrast. The contrast of the IC and the excess epoxy was increased, which helped to distinguish the edges of IC and epoxy from the surrounding air, red box in Figure 51 (left).

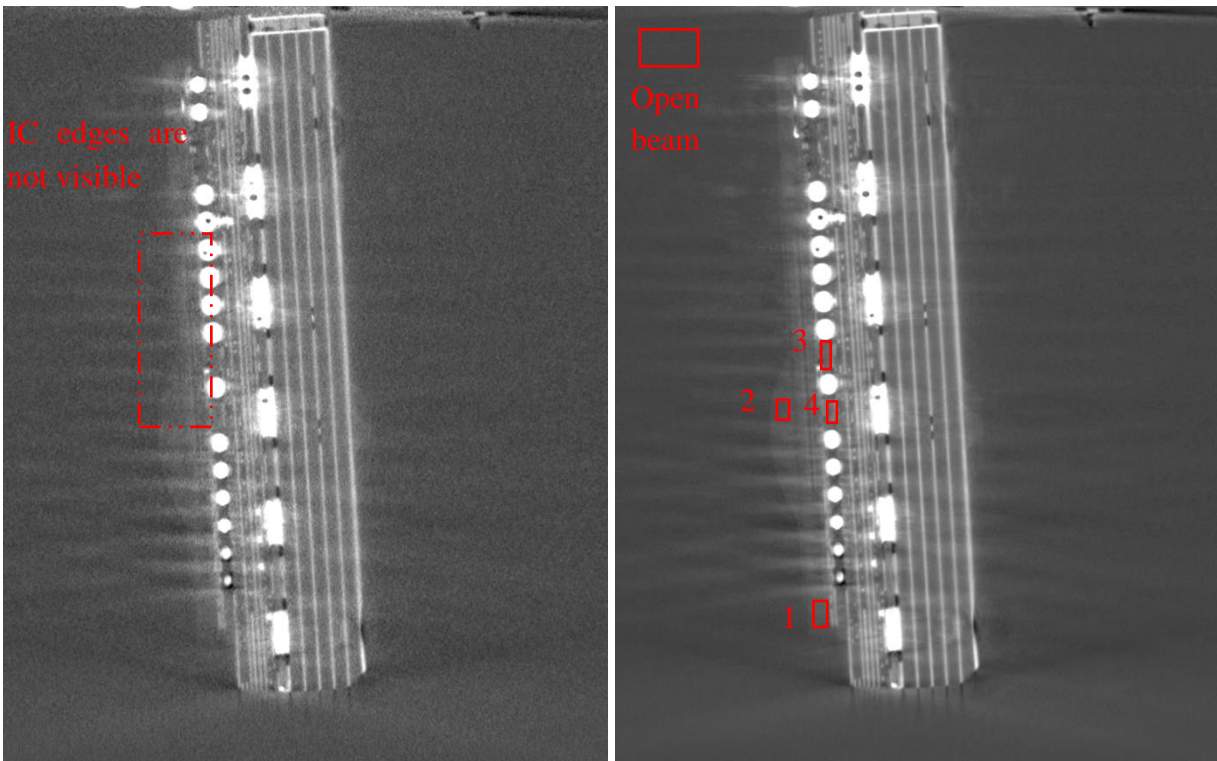


Figure 51: Volume slices reconstructed from different projections showing the improvement of the reconstruction by the image averaging approach. Left) data set obtained from individual images. Right) data set obtained by averaging 10 frames per projection.

Quantitatively, selected ROIs were chosen from the reconstructed volumes to investigate the improvement of the reconstruction by the image averaging approach. While ROI1 belongs to IC, ROI2 belongs to the excess epoxy on the top surface and (ROI3 and ROI4) for regions between the spheres. The gray values in the slices are related to the reconstructed volumes calculated based on the Lambert-Beer law attenuation coefficients. Therefore, regions of interest with the same

CNR values might indicate the same material type, such a measure is invalid for the projection calculation where different material with different thickness may produce same contrast.

The standard deviations for all selected ROIs decrease as the number of averaged images increases, Figure 52. While the SD curves for all ROIs decrease sharply in the range of (1 - 6) averaged frames, the SD value decreases by only ~ 8 % after 6 averaged frames. The standard deviation for the selected ROIs has higher values than the open beam area due to the overlap with the artifacts.

The contrast-to-noise ratio plots for the selected ROIs are shown in Figure 53. The curves show that the CNR value increases as the number of averaged images increases. The CNR values for all ROIs increase dramatically up to 6 averaged frames and then increase by less than 8% in the range of 6 to 20 averaged frames. The CNR plots for ROI3 and ROI4 have similar values to the plot of ROI2, indicating the presence of epoxy between the BGAs. However, the CNR value for the excess epoxy resin is below 5 for all volumes, so it is necessary to improve the contrast with additional approaches, especially approaches for metal artifacts reduction.

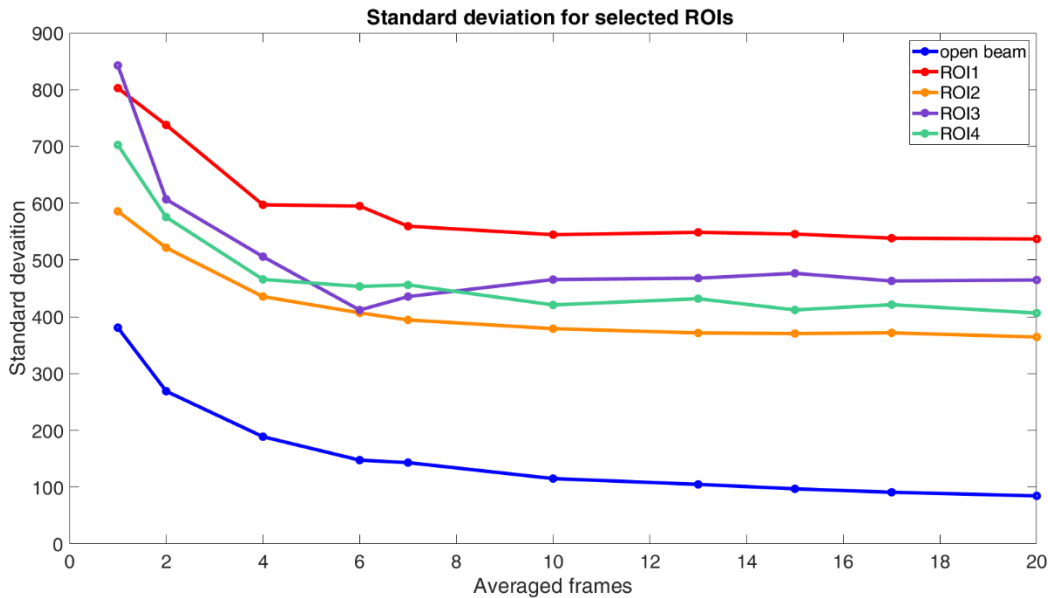


Figure 52: Standard deviation for selected ROIs. The standard deviation decreases as the number of averaged images increases. The selected ROIs are shown in Figure 51.

### 5.7.1.3 Conclusion remarks

Calculation of the standard deviation and contrast-to-noise ratio for both the projection data and the reconstructed volumes showed noise reduction using the image averaging technique. Noise can be reduced by more than 65% when only six frames per projection are averaged. The results showed a slight improvement after 6 averaged frames, e.g., the CNR increased by 7% for 20 averaged frames. However, the improvement obtained after 6 averaged frames comes at the expense of measurement time, which increases as the number of averaged images increases. Therefore, based on a trade-off between the improvement in reconstruction and measurement time,

we chose 6 averaged frames as the parameter for the next measurements with the Dexela flat panel detector.

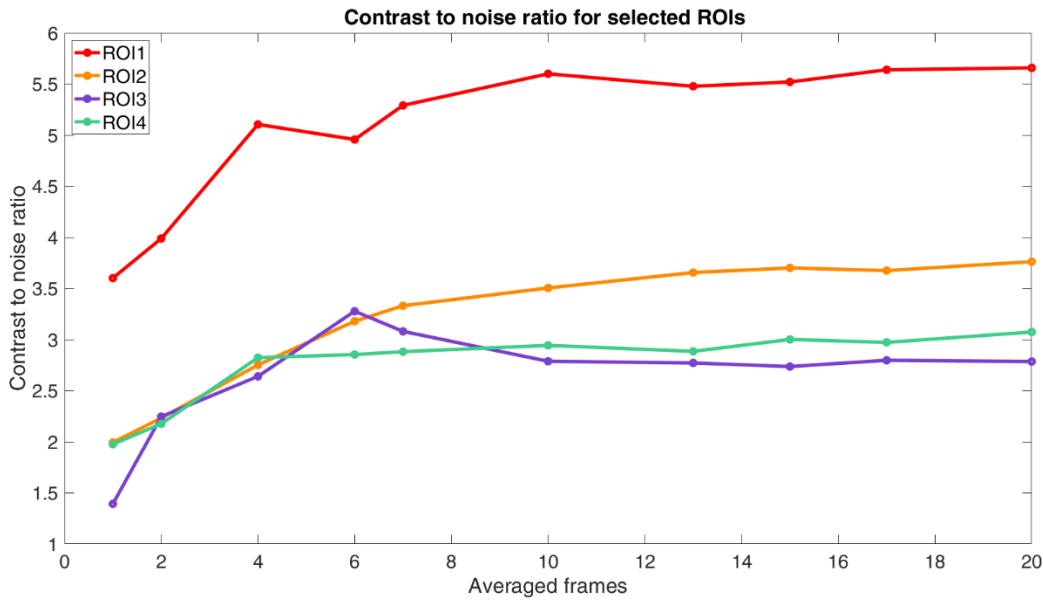


Figure 53: Contrast-to-noise ratio plots for selected ROIs. The curves show the increase in contrast with increasing number of averaged frames.

## 5.8 Metal artifact reduction utilizing different X-ray techniques

In this subchapter, we discuss the latest approaches to metal artifact reduction. We have tried to highlight the most efficient techniques, but have avoided approaches that can be performed with dedicated facilities such as synchrotron tomography, where single energy beams are used. For the experimental part, we have selected only available techniques that can be performed with the classical CT setups.

### 5.8.1 Techniques and approaches established in CT for metal artifacts reduction

Metal artifacts are consistently cited in clinical and industrial computed tomography as a problem that limits the quality of computed tomography images. They arise from CT reconstruction algorithms, mainly due to beam hardening and photon starvation caused by the highly attenuating parts of the scanned object. They usually appear as black and dark streaks near the metallic parts and across the reconstruction image. Several approaches and techniques have been introduced to minimize the effects of metal artifacts either before or after performing the CT scan. Conventional approaches can be applied prior to the CT scan to reduce the formation of metal artifacts. For example, proper filtering and high tube voltages help reduce the amount of low-energy photons, the main cause of beam hardening. The most commonly used filters to absorb the low-energy photons are copper and aluminum. A radiologist can determine the thickness of the filter by considering the applied voltage and the object content of the metals. Such approaches partially



reduce the metal artifacts. Therefore, several techniques and algorithmic approaches have been developed to overcome this limitation.

The algorithmic approaches work either in the pre-reconstructed space (projections) or in the post-reconstructed space (slices), some correct the disrupted data by interpolating from neighboring data, and others repeat the reconstruction in an iterative loop to optimize the results [55] [56]. The most common post-processing approaches are metal artifact reduction algorithms (MARs), which segment and correct the disrupted data associated with metallic parts using the Hounsfield unit threshold [56]. Several commercial MAR algorithms are available for metal artifact correction, e.g., MAR VGSTUDIO MAX, single-energy MAR (SEMAR; Toshiba Medical Systems, Otawara Japan), iterative MAR (iMAR; Siemens Healthineers, Forchheim, Germany) [57] [58]. In general, MAR algorithms are suitable for objects with sparse distribution of metal parts. They partially reduce the metal artifacts, but generate new artifacts due to misinterpretations during the segmentation and interpolation process [56].

In addition to the pre-reconstruction approaches, several techniques and approaches are also used to correct the artifacts in the post-reconstructed space. The most effective of these are dual-energy computed tomography (DECT) and data fusion of multipositional images CT [59] [60]. While the DECT technique requires two scans with two different X-ray spectra to produce a final enhanced CT, the data fusion approach requires the object to be scanned in different orientations with the same spectrum and irradiation geometry. DECT is used in clinical radiographic imaging to correct soft tissue areas damaged by metallic implants. However, choosing the right spectra is critical to achieve satisfactory results, as the approach is characterized by data acquisition at low and high energy spectra. DECT requires post-processing of the obtained images to optimize the differences between the two spectra. This can be done by calculating the monochromatic images or by calculating a weighting factor that normalizes the affected areas.

The data fusion approach is relatively new and is mainly suitable of industrial CT, where dose is not an issue and the sample can be flexibly placed in any orientation. Few studies have been found that implement this approach with only two different mounting positions, horizontal and vertical, and using weighting factors [61] [57] [60]. In this work, this approach was implemented in a different way, we performed a simulation to study the influence of workpiece orientation on the intensity of metal artifacts. The simulation allowed us to choose the identified mounting positions that give an optimal data fusion volume without using weighting factors.

### **5.8.2 Metal artifacts correction (MAR) algorithms**

Countless commercial MAR algorithms have been used in clinical and industrial fields to correct metal artifacts. However, common to all MAR algorithms is the basic concept of correction based on segmentation of corrupted projection data corresponding to metallic parts [62]. Then, the corrupted data is modified by replacing it with estimates of the corrected values [56]. The algorithms use different methods to segment the metallic parts. Some algorithms use the projection data, others use the reconstruction images (slices). In general, all commercial algorithms use the

reconstruction images to segment the metal parts by performing the following steps, Figure 54 [56].

1. Voxels belonging to the metal parts are segmented in the slices using a intensity threshold.
2. The slices are forward-projected to identify the pixels in the projections (sinogram) that are corrupted by the metal parts.
3. Interpolation of the segmented-corrupted data based on the uncorrupted projection data.
4. The corrected sinogram is back-projected to create the corrected image.

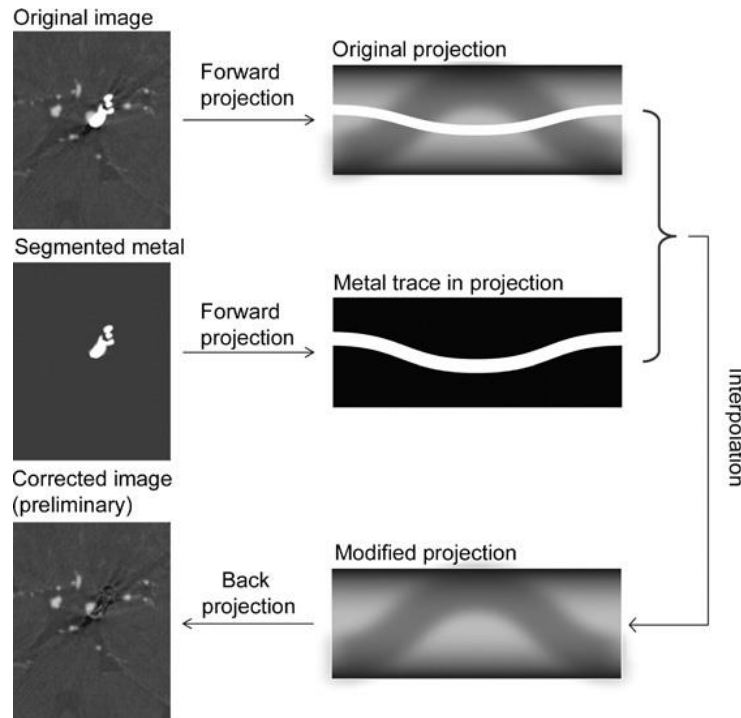


Figure 54: Illustration of metal artifact correction steps performed by image-based MAR algorithms [56].

Some algorithms iterate the correction process to reduce the remaining misclassification and consequently improve the quality of the correction at each step [56]. In normalized metal artifact removal (NMAR) technology, the image CT is normalized in the sinusoidal domain before interpolation and simple processing is first applied to abnormal data [63]. Although the algorithms of MAR correct the metal artifacts, they are associated with some disadvantages caused by miss-segmentation and miss-interpolation. For example, discarding metal-damaged data results in information loss that may not be fully recovered by interpolation. Degradation of contrast as well as introduction of new artifacts has also been reported in clinical CT using MAR algorithms [64] [56] [65].


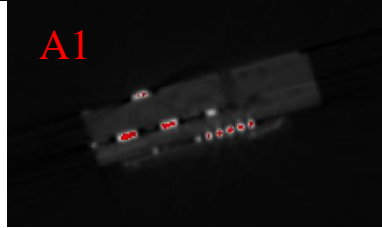
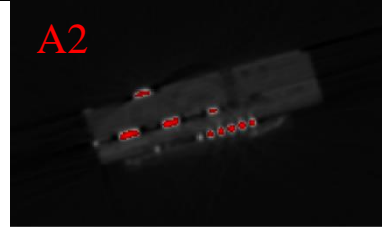
### 5.8.3 Correction of metal artifacts using sMARt from VGSTUDIO MAX

sMARt algorithm from VGSTUDIO MAX is an advanced version of MAR algorithms for improving contrast of low attenuation materials affected by metal artifact streaks. The algorithm

works during the reconstruction process. Therefore, all parameters concerning the algorithm should be set before starting the reconstruction. The user can define regions in projections belonging to metallic parts by changing an intensity threshold unit ( $I_{THL}$ ). Details about the segmentation and correction phases of this algorithms are not available due to the company privacy policy. By changing this parameter, voxels with higher intensity values will be highlighted in red (Figure 55, A0-A2). However, by increasing the number of voxels to be corrected, the quality of the reconstruction will decrease, as new artifacts will appear and the contrast will be reduced [54]. The routine was performed with different  $I_{THL}$  to correct the metal artifact streaks and make the underfilling epoxy layer visible, Figure 55 (B0 and C0).

While only central part of the spheres was corrected at  $I_{THL}$  1 (slice A1), the entire area representing the spheres was corrected at  $I_{THL}$  2 (slice A2). In addition to the spheres, metallic parts with a higher intensity than the spheres were also selected by the algorithm for correction, e.g. the second level junction (bonding) between the boards. The first set of slices in Figure 55 (A0-A2) shows the set of selected data corrected during reconstruction. The second set of slices (B0-B1) for the reconstructed volumes without and with the application of the correction show the excess epoxy defect on the top of the IC.

The corrected slices (B1-B2) are consistent with the original slice B0; however slice B1 shows an additional region of high contrast that could be interpreted as an epoxy defect, by the comparison with the original slice proves that this region is not related to the epoxy. The region of additional epoxy is not visible in slice B2, but new structures (artifacts) belonging to wire bonds are visible. The slices (C0-C2) show the efficiency of the correction routine in removing the streaks, with the streaks clearly visible in the uncorrected slice C0. However, the corrected slices (C1 and C2) show decreased contrast in addition to the appearance of new structures.

<b>Slice 0 visualize selected regions to be corrected in the projections data</b>		
Without applying sMART correction	$I_{THL}$ 1 (red voxles will be corrected)	$I_{THL}$ 2 (red voxles will be corrected, here the corrected regins are extended due to the set threshold)
		
<b>Slice2 of the reconstucted volumes shows epoxy defect on the top of the IC</b>		
The slice shows excess epoxy defect on the top of the IC	Slice after correction level 1 shows new structures (artifacts)	Slice after correction level 2 shows additional structures (artifacts) mainly form the wires.

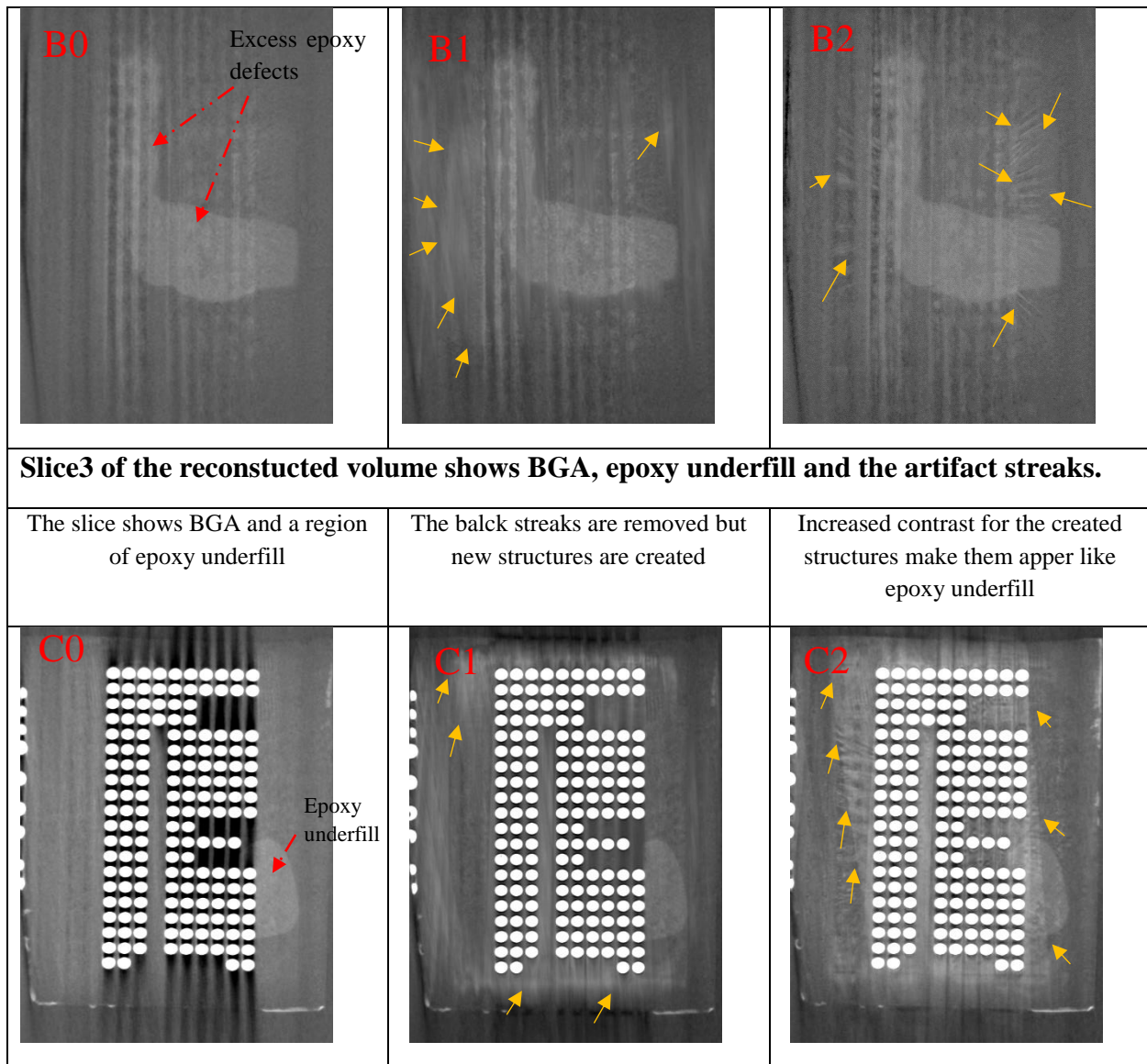


Figure 55: Effect of the application of the algorithm sMARt provided by VGSTUDIO MAX on the reconstruction. Slices of the reconstructed volumes are presented without correction and after applying the correction at two different ITHL, the yellow arrows refer to the appearance of new structures.

Due to the high metal content of this type of samples (BGA, copper pads, PCB copper substrate), the projection data set suffers from severe photon starvation. Therefore, the application of the MAR algorithm to correct for the metal artifact streaks results in an additional loss in the projection data, which already has a low information content (low statistics). The miss-correction caused by improper segmentation/interpolation resulted in the appearance of new artifacts/structures that were not present in the uncorrected slices. In addition, the contrast of the detected epoxy was degraded by the overlap with the artifact structures that could be interpreted as epoxy without prior knowledge of the original, uncorrected data.

## 5.9 Dual Energy Computed Tomography as a tool to reduce metal artifacts

Dual Energy Computed Tomography (DECT) technique has been used for decades as a tool for material decomposition and metal artifact reduction [59] [66] . DECT measurements based on a sequential acquisition approach can be performed using the micro CT setup installed at IEAP, where a sample is scanned sequentially with high energy (HE) and low energy (LE) spectra. The DECT approach benefits from the dependence of the attenuation coefficient on the photon energy and the type of material. Two different Z materials, when scanned with X-ray photons, show higher contrast in the low-energy spectrum than in the high-energy spectrum. Their contrast can be improved by subtracting the images obtained from each energy scan [67].

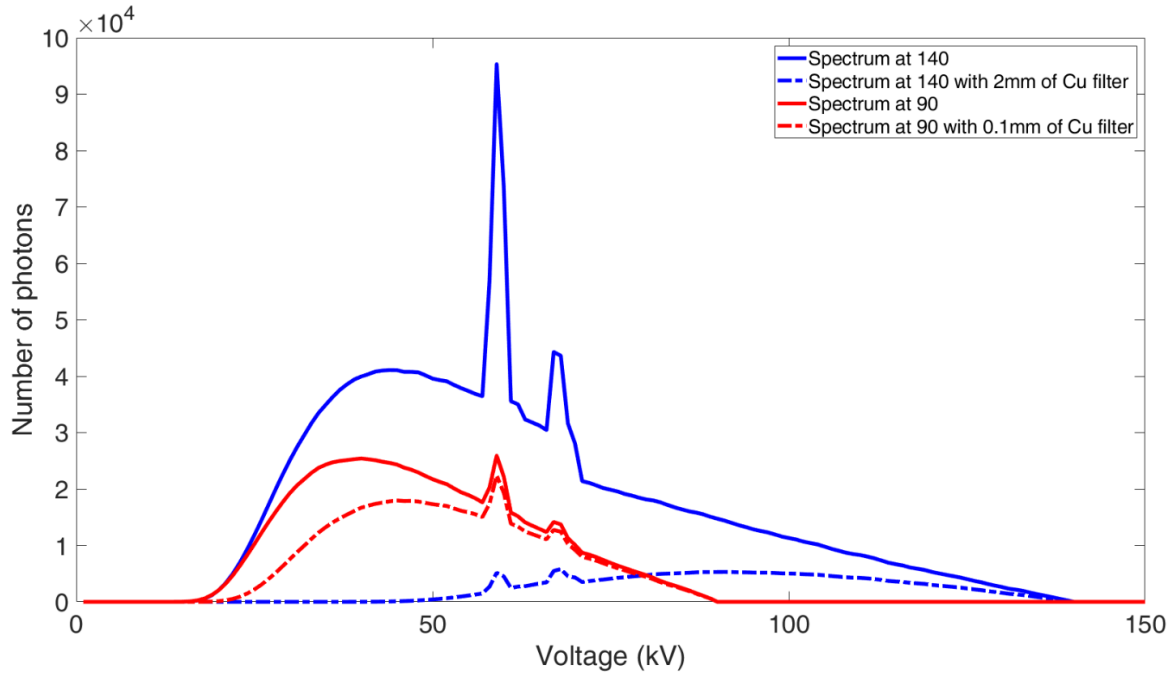


Figure 56: The simulated X-ray spectrum obtained with the Spektr open source code [8]. The solid blue line shows the spectrum at 140 kV without a filter, while the dashed blue line shows the spectrum at 140 kV with a 2 mm copper filter. The solid red line shows the spectrum at 90 kV without a filter, while the dashed red line shows the 90 kV spectrum with a 0.1 mm copper filter.

The high content of metals in the BGA sample limits the choice of high and low energy channels for the DECT approach when it is applied with limited power sources. The low-energy channel is chosen to increase the contrast of materials with low attenuation, while the high-energy channel is necessary to reduce the resulting artifacts. Therefore, the low energy measurement was performed at 90 kV using a 0.1 mm copper filter because the sample attenuates the spectrum greatly at lower voltage values. Due to the tube limitation, the high energy scan was performed at 140 kV voltage and 2 mm Cu filter. The simulated spectra obtained with the microfocus tube are shown in Figure 56. We used the open source program Spektr for the simulation [8].

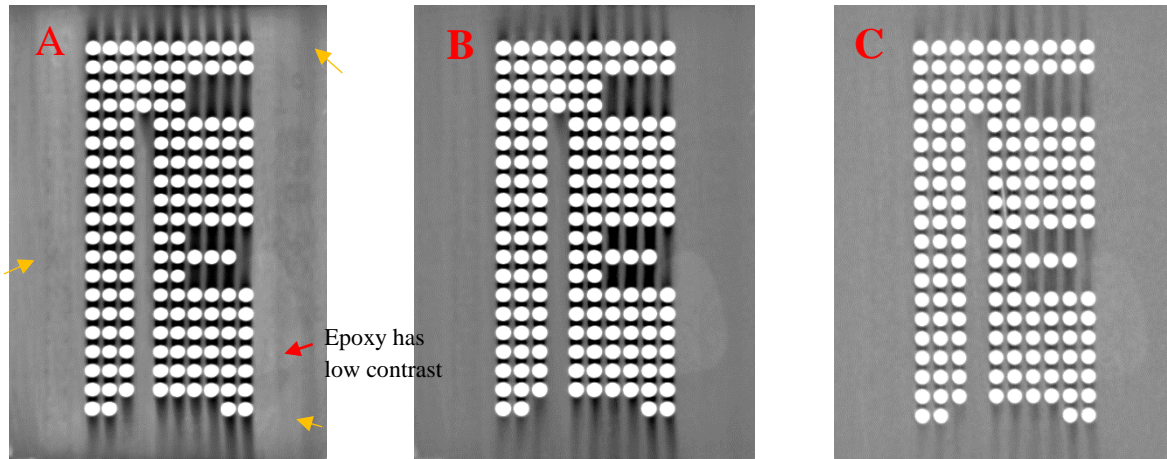


Figure 57: Dual-energy computed tomography with two different energy spectra. A) Slice through the volume at 90 kV shows low contrast for the epoxy. B) Slice through the volume at 140 kV. C) Differential slice of slice A and slice B (DECT slice) in which the streaks are less strong but the contrast of the epoxy is reduced too.

The reconstructed volume at 90 kV is noisy due to the low statistics of the projection data, where the high content of metals in the sample attenuate the X-ray beam sharply. Therefore not only metal artifact streaks are exist but also the beam hardening artifacts which degrade the contrast of epoxy, Figure 57 (A). Volume obtained at the high energy spectrum suffer mainly of metal artifact streaks with low contrast of the visualized epoxy , Figure 57 (B).

In order to enhance the contrast of epoxy and eliminate the metal artifacts, the DECT illustrated in (Figure 57, C) was performed utilizing the following formula [67]:

$$DECT_{epoxy} = HE - w_2 \times LE \quad 5.2$$

The weighting factor  $w = 0.8$  was calculated by taking the ratio of the voxel values of the same area of the metal artifact streaks of both volumes. The obtained dual-energy slice reduced the intensity of the streaks but failed to improve the contrast of the underfill epoxy. Such results were expected since proper energy channels cannot be chosen due to the tube limitation. Therefore, DECT for this type of samples cannot be successfully performed with limited energy X-ray sources.

### 5.9.1 Rotary laminography (tilted or oblique CT)

For decades, laminographic technology has been introduced to replace traditional CT techniques for inspecting flat objects (paints, circuit boards, fossils). The classical CT geometry requires a certain alignment between X-ray source, center of rotation and center of detector. For such alignment, the main axis of the X-ray beam should pass through the center of rotation to the center of the detector, while the axis of rotation is parallel to the vertical axis of the detector, Figure 58(a). Therefore, using the traditional CT trajectory to scan planar objects results in a large aspect ratio that leads to long X-ray paths through the sample at certain projection angles and prevents useful X-ray photons from reaching the detector. Projections obtained at these rotation angles cannot

provide sufficient information about the scanned object, so the traditional CT produces artifacts in the reconstructed volume. The aspect ratio problem was solved by using new scan trajectories and geometries compared to the traditional CT. Apart from the fixed trajectory between detector and source, the laminographic trajectories define relative motion between source, sample, and detector, resulting in planar laminography, swing laminography, and rotary laminography [68] [69].

While planer and swing laminography require hexapods and robotic arms to perform relative motion between the source and detector, rotary laminography can be performed with a fixed source and detector while the tilted sample rotates on its axis. Compared to other types of laminography, rotary laminography is easy to implement with non-moving sources and detectors, as is the case with synchrotron facilities and many conventional CT machines [70]. Therefore, we decided to perform a rotary laminographic measurements for the BGA sample using the micro CT setup installed at IEAP. Few successful studies were found in the literature for this type of CL using the classical CT setups, which suggested tilting either the sample or the detector [70]. The following geometry in the case of a tilted sample is shown in Figure 58 (b), where the rotational axis of the sample is tilted at an angle less than 90 degrees from the horizontal. This tilt produces smaller X-ray transmission paths through the sample at all projection angles [71]. This type of geometry requires an optimized tilt angle to reduce laminographic artifacts. Therefore, simulation is required prior to actual measurement. In addition, there is a challenge in reconstructing the projection data that requires the use of a conventional reconstruction cone beam algorithm with special/modified filters to overcome the blurring caused by the Feldkamp-Davis-Kress (FDK) method, which assumes a simple circular (non-tilted) scan trajectory [71].

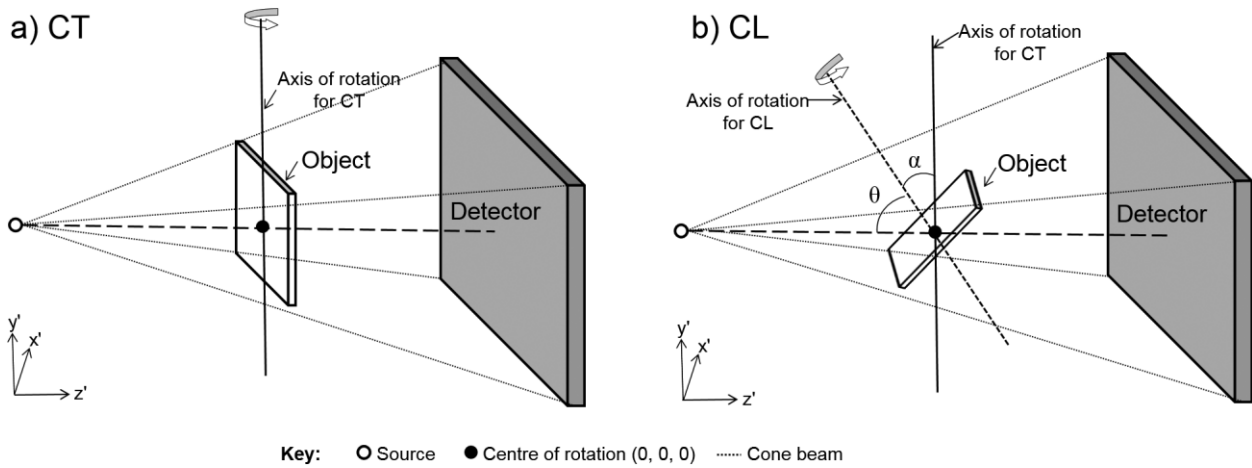


Figure 58: Illustration of (a) a conventional circular scan CT setup, and (b) laminography CL setup using conventional CT setup [71].

Reconstruction can also be performed using iterative reconstruction algorithms with standard FDK after converting the projection images to a virtual tilted detector [71]. However, such an approach leads to interpolation errors. Therefore, performing a rotational CL always demands to correct the reconstruction using various tailored iterative methods [72]. In the case of a tilted detector

geometry, the samples are parallel to the axis of the X-ray beam in the horizontal plane, while the detector is tilted with respect to the vertical plane [72]. In principle, both geometries are similar and require special reconstruction algorithms to optimize reconstruction and reduce laminographic artifacts.

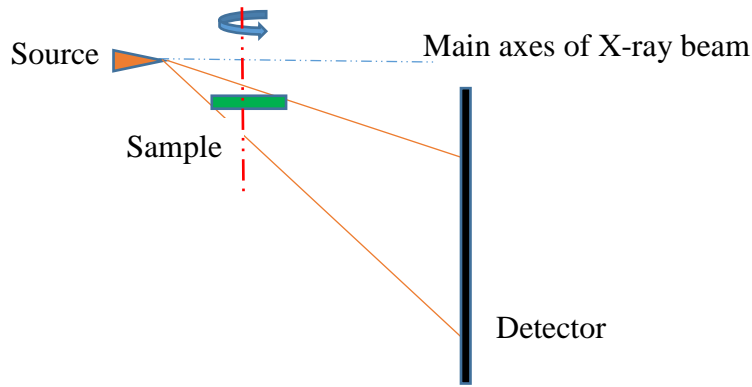
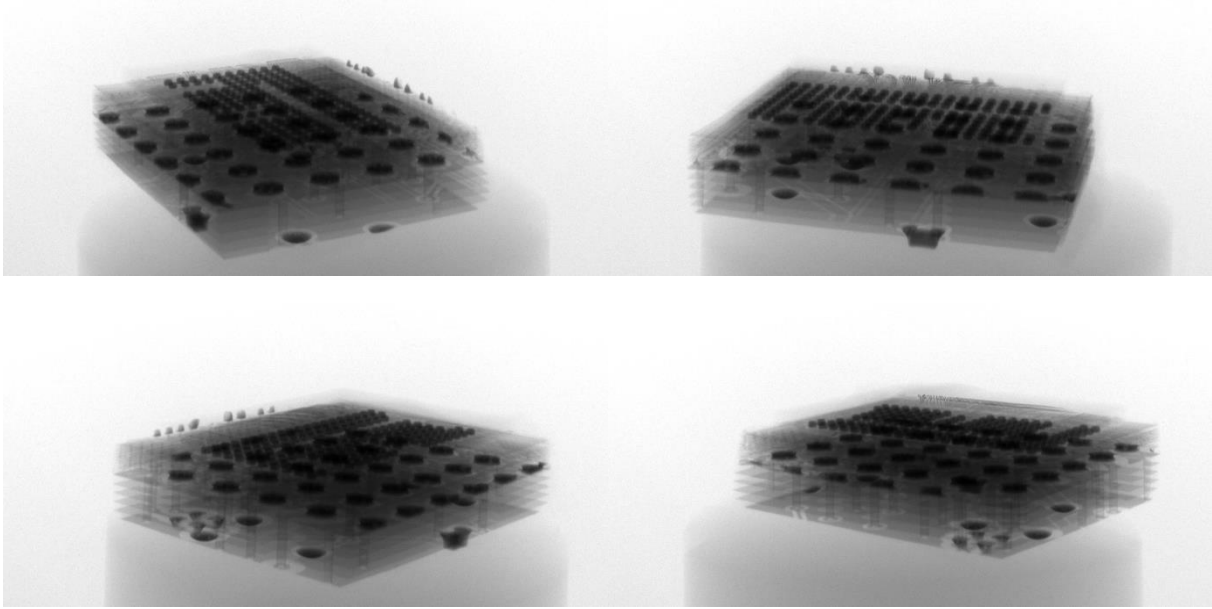


Figure 59: Illustration of the rotary computed laminography performed in IEAP setup.

### 5.9.1.1 Implemented rotary laminography using the IEAP micro CT setup

We implemented rotary CL in a slightly different geometry in order to use classical iterative reconstruction with FDK filter, Figure 59. To achieve a rotary laminography in the cone beam geometry, the sample was placed horizontally on the rotation stage below the main axis of the X-ray beam and above the center of the detector, Figure 59. Both the source and the detector are fixed during the scan, only the sample rotates around its axis. Such a geometry requires a longer acquisition time to obtain projection data with good statistics. The sample was rotated 360 degrees with 900 projections at a magnification of 6 while the tube was operated at 140 kV. Selected projections of the sample are shown in Figure 60. The projections appear as 3D in which the principal components of the sample are clearly visible, Figure 60. For reconstruction, we used the cone beam geometry with the iterative method of VGSTUDIO MAX (ART) and the FDK filter. The use of the classical algorithms resulted in a satisfactory reconstruction, except for the appearance of new types of artifacts (CL artifacts) within the slices, which has been reported with conventional reconstruction methods [70] [72]. The slices of the reconstructed volumes presented in Figure 61 show the aliasing and blurring artifacts between slices due to inadequate reconstruction algorithms and scan geometry. Figure 61 (A) shows a slice of the reconstructed volume on the plane IC. The slice shows laminographic intrinsic artifacts as black arcs next to blurred areas with high intensity on both sides. Another slice at PCB level in Figure 61 (B) reveals the CL artifacts as a white blurred area near the center. Slice C, taken at the BGA level, shows the BGA and epoxy distribution in the lower part of the slice. The slice does not have strong metal artifact streaks, as is the case with the conventional CT, but the central part is completely blurred by CL artifacts.

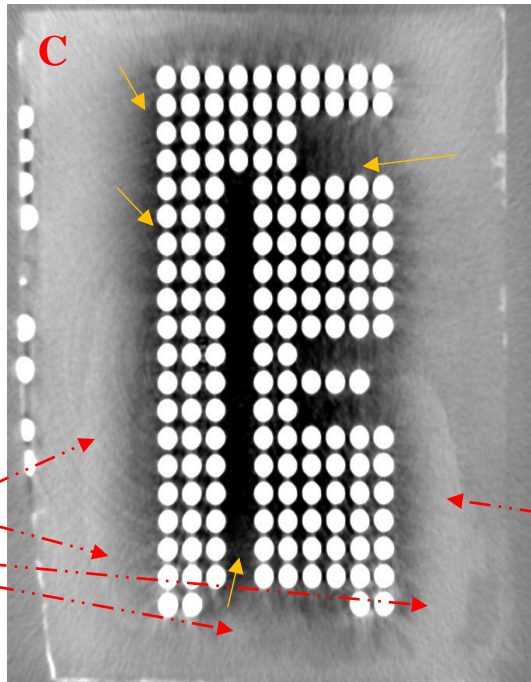
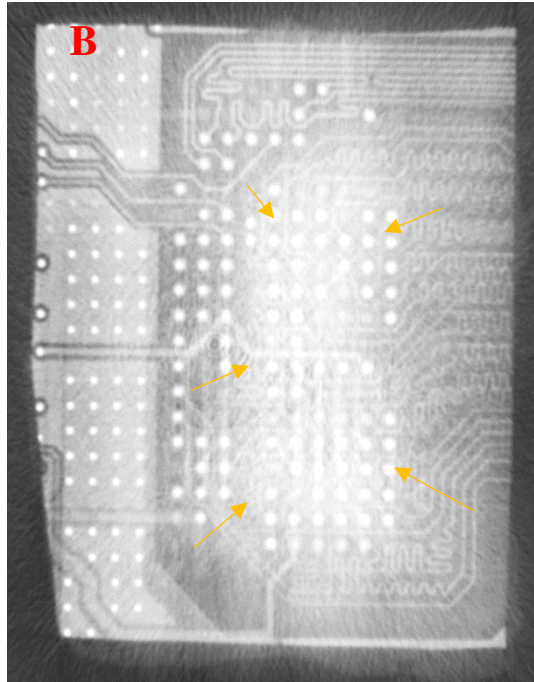
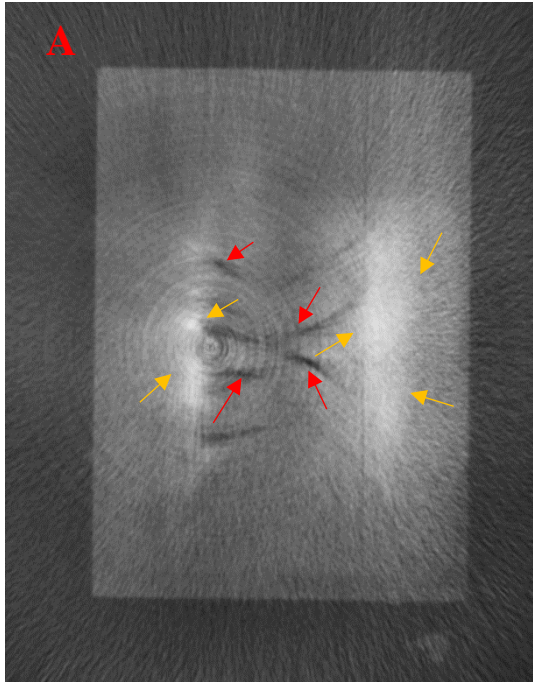




*Figure 60: laminographic projections for the BGA sample utilizing the conventional CT setup at IEAP.*

The underfill epoxy appears with a different contrast than the surrounding air; however, a data fusion measurement will show us that the sample is contaminated by an adhesive material (glue), which was used to fix the sample on the rotation stage, and the detected underfill area is a mixture of epoxy and glue.

The study of the underfill epoxy using the CL approach cannot be performed without special reconstruction algorithms due to the inner-slice and blurring artifacts that lead to miss-interpolation of the studied parts, mainly the underfill material. Focusing on new reconstruction methods is out of scope of this research and uncertain to achieve a better reconstruction with fewer artifacts. Such a solution, if it occurs, will not be available for everybody. Our goal is to find solution, accessible with instrumentation, to correct the metal artifacts caused by BGA or a similar pattern.



This area appears to be an epoxy resin, but a later accurate DFMCT measurement will prove that it is glue used to fix the sample on the rotation stage.

The detected epoxy should appear here

*Figure 61: Slices of the reconstructed volume using rotary computed laminography, yellow arcs refer to the blurring and the red ones to metal artifacts which appear as arcs. A) IC slice shows CL artifacts in the center. B) The PCB slice appears bright and blurred in the center due to artifacts from CL. C) The slice in the center of the BGA shows some detected areas of underfilling as well as complete blurring in the center.*

## 5.10 Conclusion remarks

Conventional computed tomography for samples with a specific pattern of highly attenuated materials, in our case BGA, causes the appearance of severe artifacts. Therefore, tomographic reconstruction is degraded and an investigation of epoxy underfilling between spheres is quite tricky. The classical metal artifact reduction methods such as MAR algorithms, dual-energy CT, and rotary laminography applied in this chapter were not suitable to correct the metal artifacts caused by BGA. MAR Algorithms generally correct the metal artifacts based on pre-correction of the projection data that cause these artifacts to occur. Since all MAR algorithms correct the disturbed data by interpolating from neighboring data, they partially reduce the metal artifacts but create new artifacts due to misinterpretation during the segmentation and interpolation process. This was the case with the sMART algorithm from VG studio, which caused the appearance of new structures and artifacts with an intensity similar to that of epoxy, leading to misinterpretations regarding epoxy distribution.

The dual-energy CT, on the other hand, could not meet the correction requirements due to the use of X-ray sources with limited energy. However, the use of higher energy spectra can lead to a reduction in artifacts, but the contrast of the epoxy will be reduced as well because high-energy photons easily penetrate the underfill layer. The application of the rotary CL method with a conventional CT setup did not lead to a satisfactory result, since advanced, special reconstruction algorithms are required that take into account the applied geometry (the source-sample detector does not follow the in-line geometry). Results of the CL applied to the BGA samples showed inner-slices and blur artifacts and did not contribute to successfully investigating epoxy between BGAs.

In the next chapter, a DFMCT-based methodology will be presented to successfully correct the artifacts.

## **6 Epoxy inspection utilizing data fusion of multipositional computed tomography**

This chapter presents the results of a simulation study to determine the optimal orientations for the BGA samples that produce CTs with fewer artifacts. The simulation software aRTist was used for the simulation [73]. The simulator is described in the first section of this chapter. We have described the main modules that the software executes to perform a simulated CT scan. The tested phantom was modelled to match the real BGA samples presented in the experimental section. The software performs CT scans based on a ray casting method for a 3D geometric model (CAD or STL files). The simulation showed that the best orientation at tilt angles (inclination of the vertical axes) in the range of ([5 -10] and [55-65]) degrees, Figure 67. Reconstructed volumes obtained with tilt angles in these ranges produce fewer artifacts compared to volumes obtained at random tilt angles outside these ranges. The data fusion approach was then applied to the volumes of the recommended ranges producing a fused volume with clear epoxy underfill shape and corrected artifacts. The fused volume of four carefully selected volumes was comparable to the fused volume of 19 different volumes obtained from different orientations. Results of the simulation and the experimental results were published in the author's articles [74].

### **6.1 Radiographic simulator aRTist**

The analytical RT inspection and simulation tool (aRTist) developed by BAM Berlin was used for the CT simulation [75] [76]. The aRTist simulator uses both Monte-Carlo and analytical methods to predict the radiation transport [75]. The program features acceptable processing speed, high level of realism and ease of use with a 3D graphical user interface that allows you to set all the necessary parameters before starting the simulation, Figure 62. The user interface includes a parameter panel displaying all simulated parts, a virtual scene in the center and a docking area on the right side. Different modules can be opened and attached to the docking area, e.g. image viewer and CT scan modules, all of which can be seen in Figure 62. While the image viewer window visualizes the most recently acquired X-ray images, the CT scan window allows the user to define CT parameters such as the number of projections, the angular step and the rotated objects.

Before starting the X-ray simulation, the user should define a radiation source, a detector and a scanned object. aRTist provides tools and modules that allow the user to construct, position and manipulate the simulation components in the virtual scene. The most important modules are explained in the following subsections [76]:

#### **6.1.1 The source/spectrum module**

The spectrum calculation module allows the calculation of a realistic spectrum based on the given parameters of the X-ray tube. Figure 63 shows the source module with all the required parameters, such as tube type, target material and thickness, window type and thickness. The profile of the focal spot can also be modeled after the type and size of the focal spot are specified, Figure 63

(left-bottom). The X-ray spectrum shown in Figure 63 (right) was calculated at 140 kV from a transmission tube with a W target and only one type of inherited filtering. The parameters were

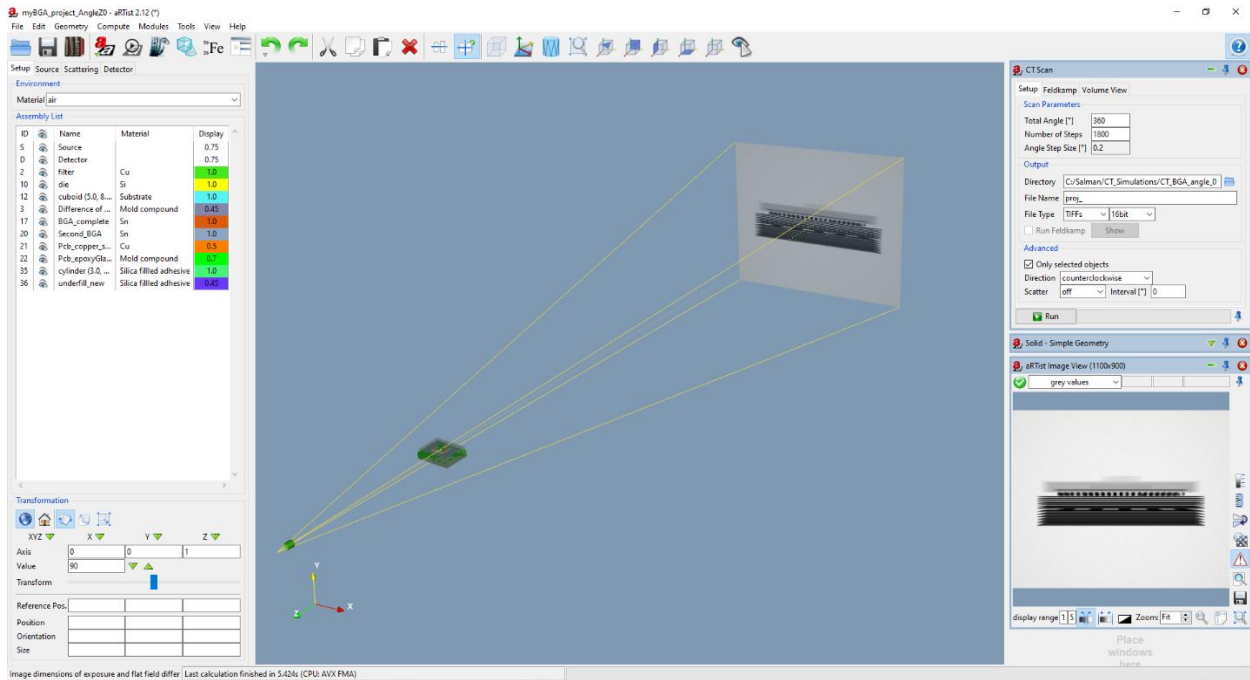


Figure 62: The user interface of the X-ray simulator aRTist shows the parameter panel on the left, the virtual scene with a displayed object in the middle, CT scan and Image Viewer windows on the right.

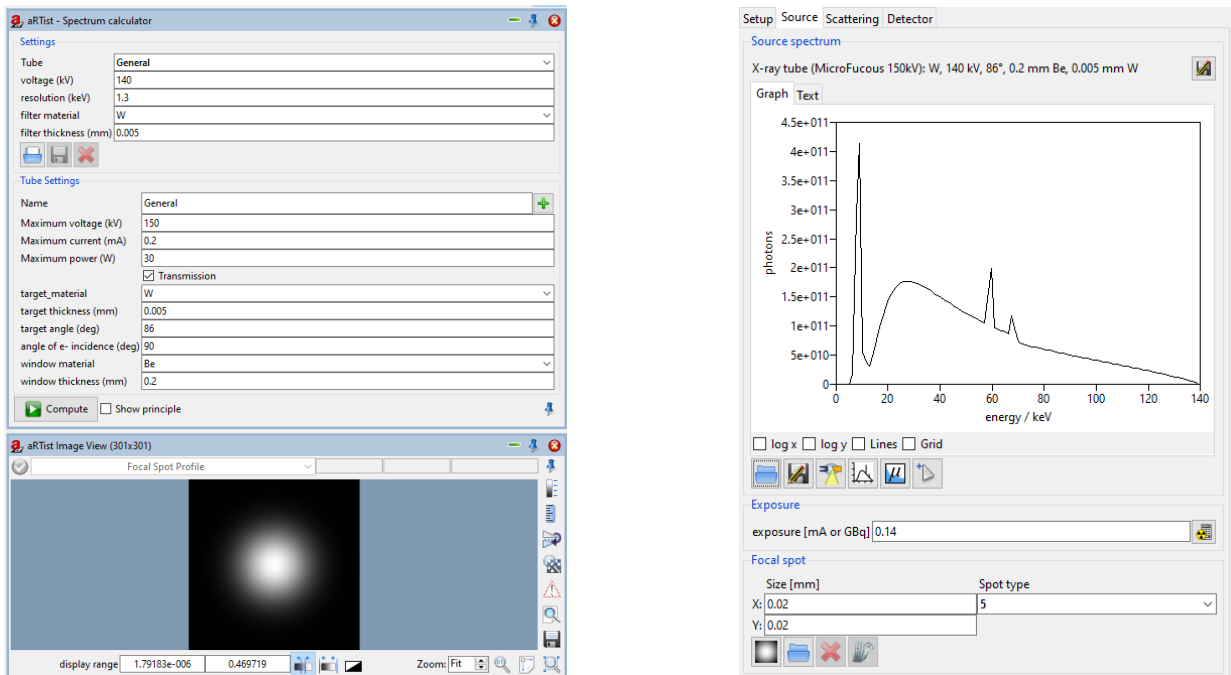


Figure 63: Illustration of the main supported modules in aRTist. Left) Spectrum calculation plugin with a focal spot profile displayed in the image viewer. Right) X-ray spectrum calculated using the parameters of the spectrum calculation module.

Set similarly to the microfocus tube operated in the IEAP laboratories to obtain an X-ray spectrum similar to that used in the experiments. Alternatively, it is possible to load a measured spectrum for simulation.

### 6.1.2 The detector module

A digital detector for virtual imaging can be easily modeled using the detector calculator plugin Figure 64 (left). Modeling a detector involves determining the number of pixels, pixel pitch, sensor material, and thickness. After setting all required parameters, a calibration routine is provided to accurately characterize the detector. The routine requires experimental reference image (reference shot). A reference shot with the required values is provided in aRTist and was used to calibrate the modeled flat panel detector used in the simulation for this work, Figure 64 (left) [73]. The modeled detector can be selected in a separate window in the parameter panel, Figure 64 (right). It is also possible to define the maximum gray level, exposure time, and number of frames per acquisition, and to apply flat-field correction.

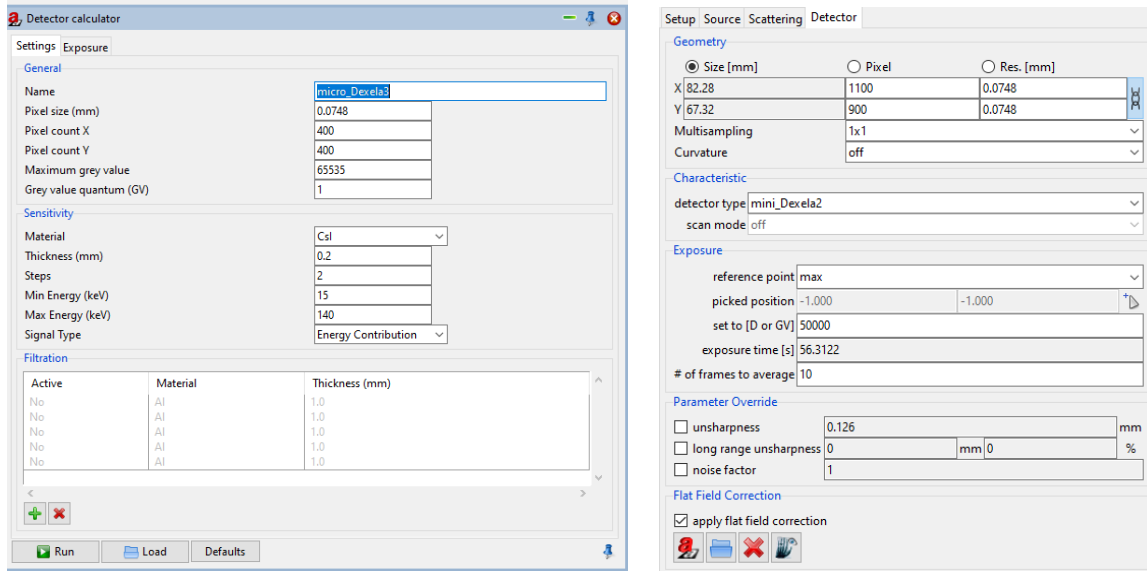


Figure 64: Left) Detector calculator module with all necessary parameters to define a detector. Right) Parameter panel with the "Selected Detector" tab showing the selected detector and the possibility to apply different correction methods to the calculated image.

### 6.1.3 The geometrical model

aRTist simulator supports CAD oriented object descriptions, especially files in .stl format, therefore the scanned object can be modeled in different modeling programs and imported into aRTist. Non-complex geometric objects can be constructed directly in aRTist from primitives such as cuboids, cylinders and spheres using Boolean operations. An object can have different parts modeled by triangulated boundary representations that separate regions of homogeneous material [75]. The attenuation of the beam is calculated based on the penetration lengths within the material in linear connection between the source points and the detector pixels [75]. The user defines the

material of the object in the parameter panel from a predefined list of the most commonly used materials, to which a new material can also be added.

## 6.2 Radiographic simulation to evaluate workpiece orientation

To estimate the best orientation for the BGA sample on the rotary, we performed a radiographic simulation similar to the planned experimental measurement. A modeled phantom that had the same attenuation characteristics as the real BGA sample was performed for the simulation. As well, the Dexela flat panel detector and the X-ray spectrum of the Hamamatsu tube at 140 kV and using a 2 mm copper filter were modeled using the source and detector model of aRTist. Then we started the simulation by investigating two types of tilt orientations for the sample on the rotational stage. The following subsections describe the simulation study and the results obtained.

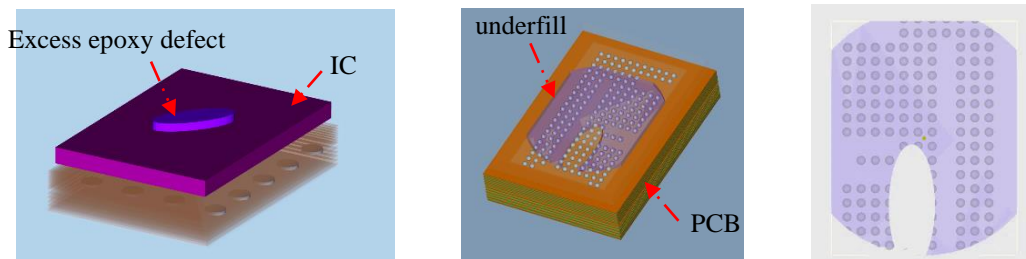


Figure 65: 3D illustration of the BGA phantom used for the simulation, left) shows the PCB, IC and excess epoxy on top. Right) shows the BGA and the shape of the epoxy underfill.

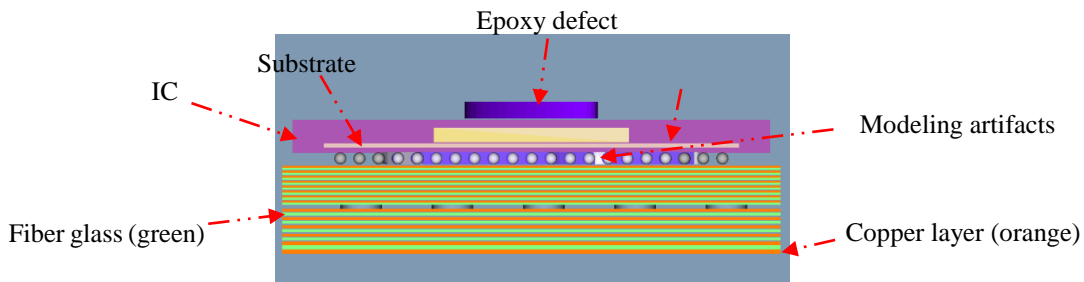


Figure 66: A cross-section shows all the components of the phantom. The following color coding was used to differentiate between different components, purple for epoxy, pink for the IC, gray for the BGA, orange for copper and green fiber glass.

### 6.2.1 Phantom description

The simulated phantom is approximately identical to the BGA sample studied in terms of geometry and composite materials. The overall structure of the phantom can be seen in Figure 65 and as well in Figure 66. The phantom combines various electronic components made of different materials and was created using the aRTist construction tools. The IC component was modelled from two different parts: a chip and a substrate of silicon encased in a casting material. On the top of IC, we simulated an ellipse-shaped excess epoxy defect centered on the surface of IC, Figure 65 (left).

The PCB was modelled as a set of copper layers with different thicknesses separated by layers of glass fiber, with a size of 8 mm × 12 mm and an overall thickness of 3 mm, Figure 65 (middle). The BGA consists of 162 tin spheres arranged in a rectangular pattern with some empty spaces, similar to the real BGA pattern. The diameter of each ball is ~400 μm and center to center distance between the balls is ~800 μm. A simulated underfill layer of 400 μm thickness was inserted between the BGAs. The underfill layer was simulated smaller than the bottom surface of the IC, taking into account the probability of partial underfilling, Figure 65 (right). Since we could not know the exact composition of the used epoxy compound (type LOCTITE ECCOBOND FP4531), we choose a silica filled adhesive material, which is widely used as an underfill material, to perform the phantom calculation. A second-level connection compound (big tin balls) was also inserted between the PCB layers as it is present in the real sample. However, the real sample contains several components that were not modeled for the phantom, such as wire bonds and vias. Modeling these components takes a lot of time and does not contribute to the artifacts created by the BGA. It is worth noting that the modeled underfill contains modeling defects caused by aRTist, since few logical operators were used to avoid the overlap between the underfill layer and the BGA assembly, Figure 66.

### 6.2.2 Simulation strategy and parameters

The simulation was performed to the phantom in different orientations in the Euclidean space. The orientations included two different tilt configurations, T1 and T2, for the tilt angle  $\beta$  in the range (0-90) degrees of the major axis of the phantom with respect to the CT rotation axis (Z). To clarify the T1 and T2 configurations, we define the plane containing the BGA pattern as the BGA plane. This plane is parallel to the phantom surface and perpendicular to the phantom edge. Figure 67 illustrates the T1 tilt orientation of the phantom, where the phantom surface/BGA plane remains perpendicular to the horizontal plane despite the tilt. With this type of tilt, the sample is at an angle 0 in the portrait orientation and 90 degrees in the landscape orientation, Figure 67 (A and B). With the T2 configuration, the phantom surface/BGA plane forms an angle with the horizontal plane equal to the tilt angle. At 90 degrees, the BGA plane becomes parallel to the horizontal plane, Figure 68. Both the T1 and T2 orientations are examined in detail in the next sections. A CT scans with 1800 projections were simulated for the phantom in each tilt position, resulting in a total of 19 CT scans for the T1 orientation and 19 CT scans for the T2 orientation.

All the simulated CT scans were performed with the same geometry and irradiation parameters (tube voltage+tube current) at magnification  $M=5$  and using a 2mm copper filter. Table 5 lists all parameters related to the simulated CT scans. The projections obtained from the simulation are flat-filed corrected using aRTist software, and the filtered back projection method from VGSTUDIO MAX was used for reconstruction. After reconstruction, we initiated a registration process to align the reconstructed volumes, which have different orientations due to the different scan orientations. The registration is necessary to combine voxels with the same coordinates from different volumes. Dragonfly software for 3D visualization provides advanced tools for



registration, which was used in our study [15]. The registration involved rotation, translation, and scaling using the mutual information method and linear interpolation.

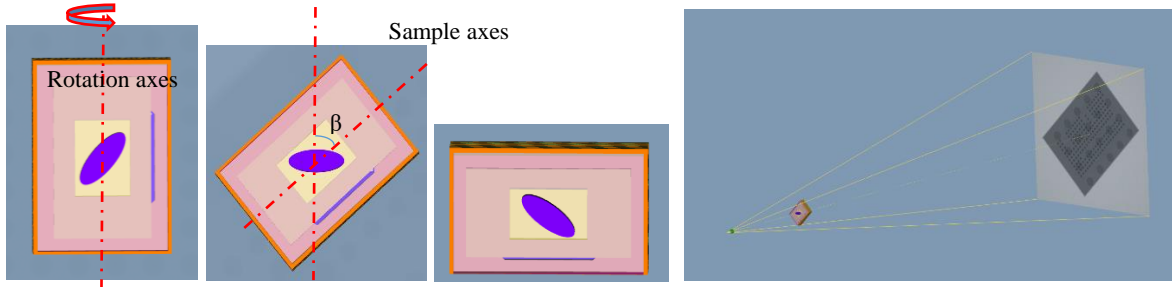


Figure 67: Tilt orientations of the phantom (T1). A) Portrait position 0 degrees, B) tilted 45 degrees, C) landscape position 90 degrees, D) Scene view of an RTist simulator with source, detector and the phantom tilted 45 degrees (T1 orientation).

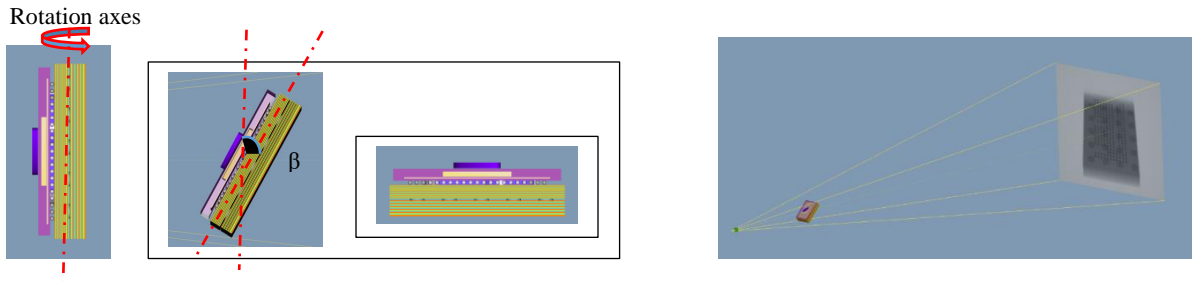


Figure 68: Tilt orientations of the phantom (T2). A) The surface of the phantom is parallel to the detector, B) tilted 45 degrees from the vertical plane, C) Parallel to the horizontal plane, D) Scene view of the RTist simulator showing source, detector, and the phantom tilted 45 degrees (T2 orientation).

Table 5. Simulation parameters for T1 and T2 orientation.

Orientation	M	V(kV)	Filter(mm)	Projections/scan	Time/scan	correction	Spot size
T1	4.6	140	Cu 2.0	1800	5 hours	Flat field	20
T2	4.6	140	Cu 2.0	1800	5 hours	Flat field	20

### 6.2.3 Evaluation of T1 orientation

As we mentioned, the CT scans were acquired under the same irradiation parameters (tube current+ tube voltage) except for the phantom tiling angle, which varied between 0 degrees and 90 degrees with an angular step of 5 degrees. We performed 19 simulated CT scans for the phantom at 140 kv and magnification 4.6. First, the phantom was mounted in portrait position (0 degrees), then it was rotated around the vertical axis (360 degrees), collecting 1800 projections. For the next CT scan, the phantom was tilted 5 degree and rotated around the vertical axis to obtain the same number of projections. Figure 69 (A), represents a projection of a CT scan at a tilt angle  $\beta$ . The scanned projections at each tilt angle were then reconstructed. For the comparison between the different volumes, a slice image at the BGA level is considered, see Figure 69 (B). The selected slice shows

the epoxy layer with higher contrast than the surrounding air, and the streak artifacts are also visible parallel to the central X-ray beam axis. The registered slice, aligned to the same slice acquired at the portrait position, is shown in Figure 69 (C). Since the registration involved rotating the slice by an angle  $\beta$ , the streaks in the registered slice are tilted by the same angle  $\beta$ . The same registration process was performed for all reconstructed volumes.

Basically, three main processes were applied for each tilt angle, including data acquisition, reconstruction and registration, resulting in 19 different reconstructed volumes.

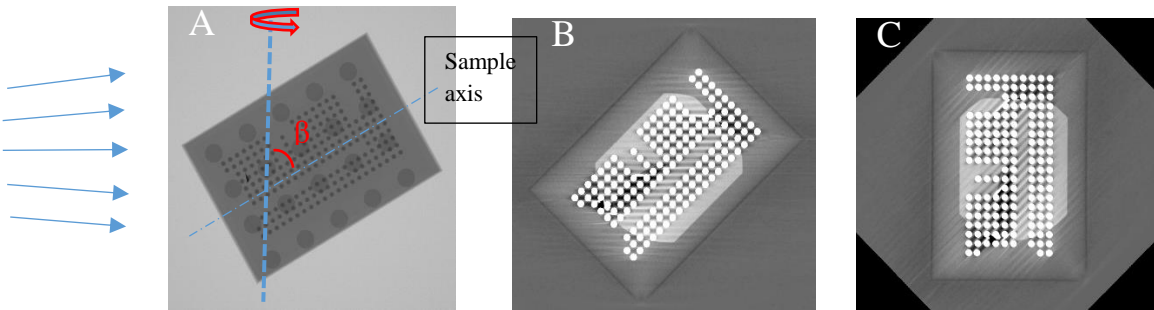


Figure 69. The main process applied to the phantom at each tilt angle. A) Projection (represents the data acquisition process), B) volume slice (represents the reconstruction process), C) Registered slice (represents the registration process).

### 6.2.3.1 Traversal-path lengths

The intensity of the generated metal artifact streaks depends on the traversal-path lengths (transmission lengths) through the BGA, which in turn is dependent on the tilt angles [77]. Therefore, the calculation of the transmission lengths through the BGA spheres for each tilt angle was modeled using a Matlab code. For the calculation, we calculated the maximum traversal-path length ( $\max(\text{TPL})$ ) and the average difference between the traversal-paths ( $\text{avg}(\text{TPL})$ ). Both parameters play a role in beam hardening effects that lead to distortion during reconstruction and cause the formation of metal artifacts [78]. The curves of the calculated parameters  $\max(\text{TPL})$  and ( $\text{avg}(\text{TPL})$ ) are shown in Figure 70. At angle 90 degrees, where the number of spheres in a row facing the X-ray beam is 20, the value of ( $\max(\text{TPL})$ ) is twice as large as the value at angle 0 degrees, where the number of spheres in a row is 10. The parameter ( $\max(\text{TPL})$ ) increases with the angle of inclination, with two ranges of low values between [5-10 and 20-30] and a notable peak at 45 degrees.

On the other hand, the average differences parameter ( $\text{avg}(\text{TPL})$ ) has the highest values at 0 and 90 degrees, with a peak at 45 degrees, similar to the ( $\max(\text{TPL})$ ) plot. The lowest ( $\text{avg}(\text{TPL})$ ) values are in the range of (50-65) degrees. Since both parameters affect the generated streaks, it is clear that the volumes obtained at 0, 45 and 90 degrees should suffer from severe artifacts. Basically, minimizing these parameters by choosing the right mounting position/tilt angle will reduce the artifacts and improve the accuracy of the CT method. Therefore, volumes in the ranges [5-30] and [50-65] are expected to give good reconstructed volumes. The intensity of the artifacts

is also affected by the existence of an underfill layer, which modify the intensity values of the disturbed voxels by the reconstruction algorithms. However, this effect is observed in the artifacts generated in the epoxy- filled and non-filled regions, respectively.

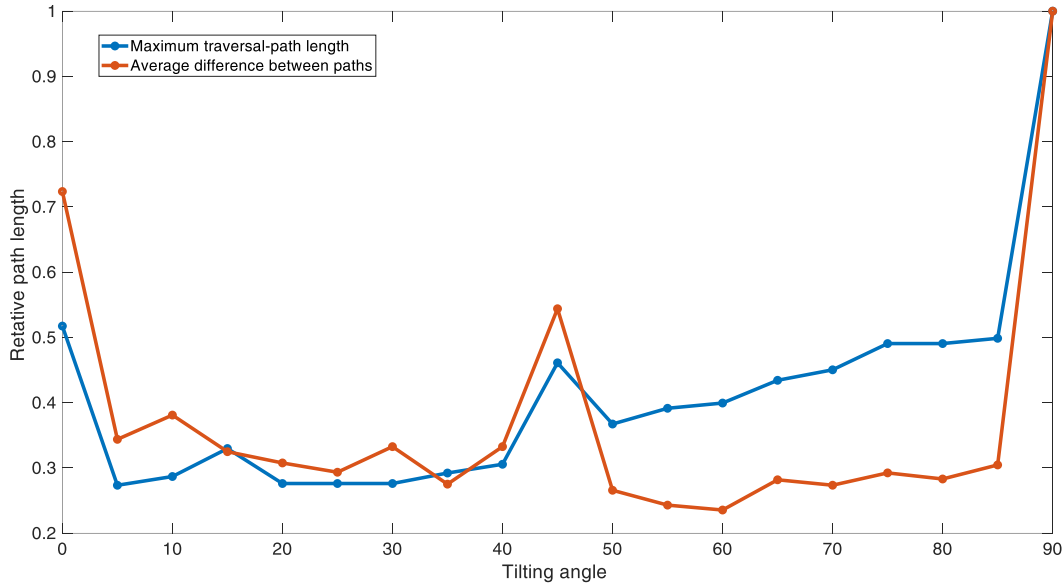


Figure 70. Traversal-path lengths through the BGA calculated for each tilt angle. Blue) maximum traversal-path ( $\max(TPL)$ ), Red) Average difference between the traversal-paths ( $\text{avg}(TPL)$ ).

### 6.2.3.2 Results and discussion

A radiologist is able to visually assess the quality of reconstructed images based on image contrast, the amount of noise generated, and artifacts. Therefore, visual comparison is used as an important criterion for evaluation. In our case, we should distinguish between two main factors in the visual evaluation: first, the number and intensity of the generated streaks, and second, the overlap between the streaks which causes deterioration of the shape of the epoxy, especially at the edges.

Slices of the registered volumes of T1 orientations are shown in Figure 71. For visual comparison, only slices of volumes obtained at 15 degrees angular step are shown because slices at finer angular step are difficult to be visually compared. The slices were normalized to reveal the underfilling epoxy layer with the same contrast comparing to the open beam (surrounding air). The slices demonstrate the BGA, the underfill epoxy layer, and the metal artifacts created by the BGA. In addition to metal artifacts, the slices show modeling artifacts caused by the modelling defects, Figure 71 (B) inside yellow boxes. The metal artifacts appear as black (negative) and white (positive) streaks at different locations affected by the tilt angle. The intensity of the streaks increases with the number of spheres in a row facing the incident X-ray beam as the maximum traversal- path increases, Figure 71 (portrait and landscape).

On the other hand, the streaks on the images are placed in different places. For example, while the volume obtained at 0 degrees features the black streaks horizontally, the volume obtained at

90 degrees features the black streaks vertically. The streaks are most pronounced at volumes 0, 45, and 90, which is consistent with the result of the traversal path calculation, where both traversal parameters are high. The number of streaks at 45 degrees is higher due to the higher average difference value ( $\text{avg(TPL)}$ ), which in turn leads to an overlap between the streaks. The high frequency of generated streaks at the volume 45 degrees leads to misinterpretations of the epoxy layer. For example, it is not clear whether epoxy is present in region 1 and region 2; moreover, the edges of the epoxy are not well visible in regions 3 and 4, Figure 71. At volume 60 degrees, despite the overlap with the streaks, the contrast of the epoxy resin is high enough to confirm the existence of the epoxy resin in region 1 and region 2. At volume 30, the streaks in regions 1 and 2 can be seen with low intensity, while the intensity in region 4 appears higher.

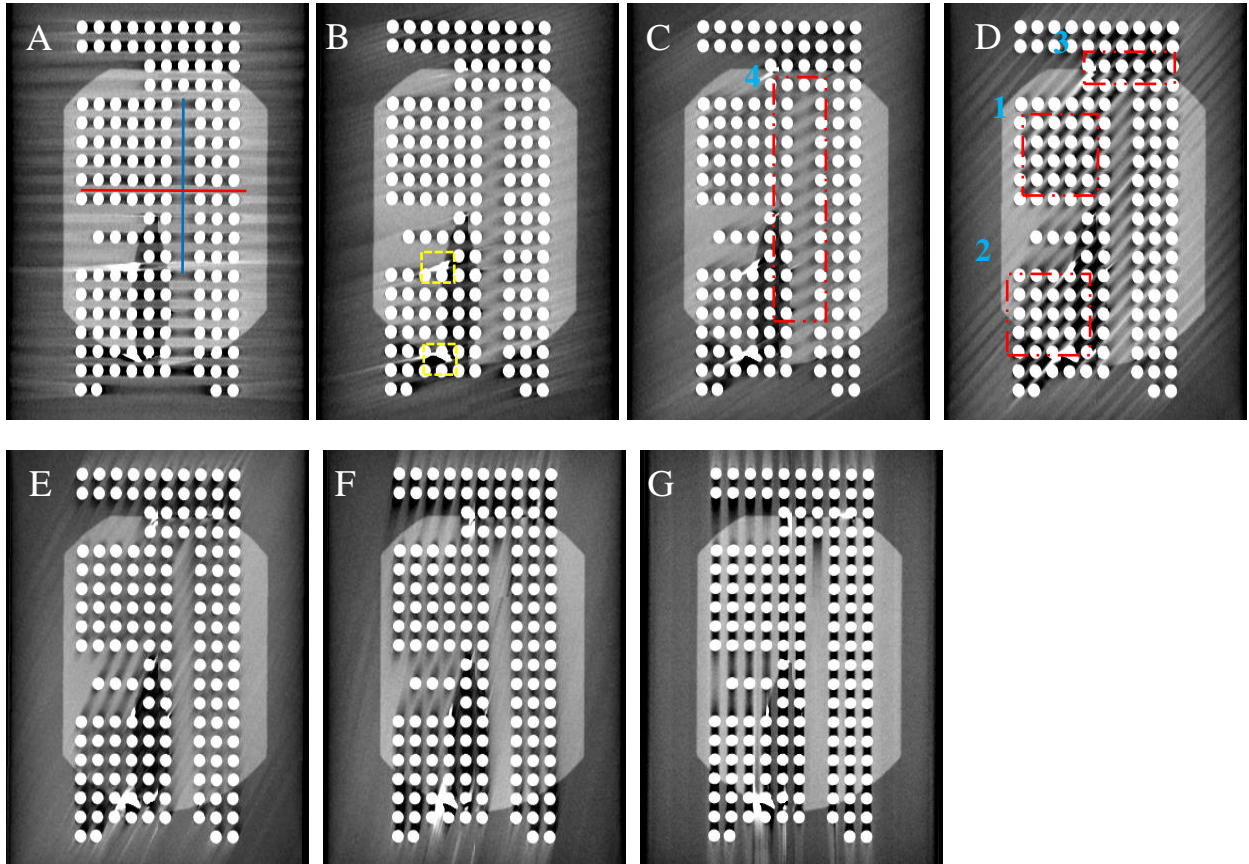


Figure 71: Registered and normalized slices of the reconstructed volumes at different tilt angles. A) 0 degrees tilt, B) 15 degrees, yellow boxes refer to modeling artifacts C) 30 degrees D) 45 degrees E) 60 degrees F) 75 degrees G) 90 degrees.

Quantitatively, we considered the calculation of intensity profiles for two perpendicular lines of voxels in the reconstructed volumes to measure the effects of artifacts on the gray levels, Figure 71(A). Choosing sub-regions over intensity lines for computation is insufficient because the positions of the streaks change depending on the angle of inclination. The intensity profiles measure the intensity/strength of the artifacts alongside the average deviation of the voxels from the mean intensity value (which is assumed to be the true value). In an ideal reconstruction and

without the influence of artifacts, the intensity gray values of voxels of the same material should not show significant deviations (highly dispersive). Figure 72 shows the intensity profiles for the marked row and column in Figure 71 for all reconstructed volumes. The blue lines represent the selected column of voxels, and the red lines belong to the selected row of voxels. The effect of streaks on the intensity profiles is visible for plots with sinusoidal waves, e.g. Figure 72 blue line at 0 and red line at 90.

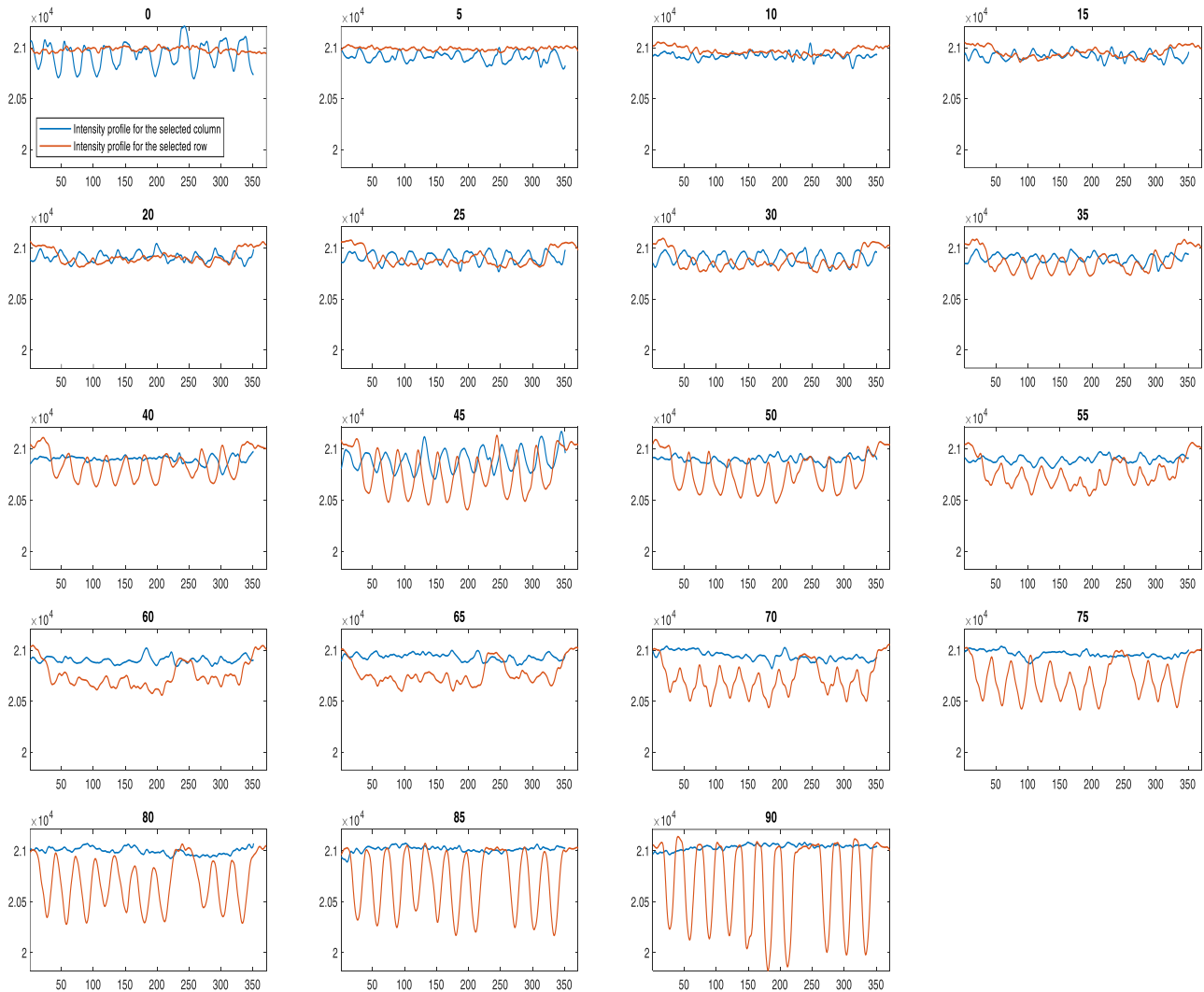


Figure 72: Plots of intensity profiles for the defined column (blue) and row (red) of voxels within the underfill epoxy. The diagrams belong to the volume slices at all tilt angles.

While the blue line at volume 0 is sinusoidal due to the horizontal streaks and has a deviation of 120, the red line averages around  $2.1 \times 10^4$  with a deviation of only 21. The streaks increased the intensity deviation by 5.7 for the column voxels. In contrast, the intensity line for the row of voxels at 90 degrees (Figure 72, volume 90) is sinusoidally affected by the streaks with a deviation of 400, the intensity line for the column of voxels (blue plot) is on average about  $2.1 \times 10^4$  with a

deviation of 27, the streaks increased the deviation by 14.7. The intensity lines at 45 degrees show the effect of the white and dark streaks overlapping on the true gray values. This volume shows a higher deviation around the average value. In general, the amplitude of the red curves is larger than the amplitude of the blue curves because the X-ray beam passes through a larger number of spheres in the longitudinal direction, Figure 72 (red lines of the plots at (70-90)).

To clarify the comparison, in addition to the standard deviation for voxel of each line separately (row and column voxels), we also calculated the standard deviation of the voxels of both lines together, see Figure 73. While the blue-dashed curve represents the deviation of the column voxels (longitudinal direction), the red-dashed curve shows the standard deviation of the row voxels. The blue curve seems to be more stable than the red line. It takes low values in the ranges (5-20) and (50-65), with a high peak at 45 degrees. On the other hand, the deviation of the voxels in the transverse direction (red line) increases gradually, with a strong peak at 45 degrees. The curve shows a decrease in the range (55- 67)).

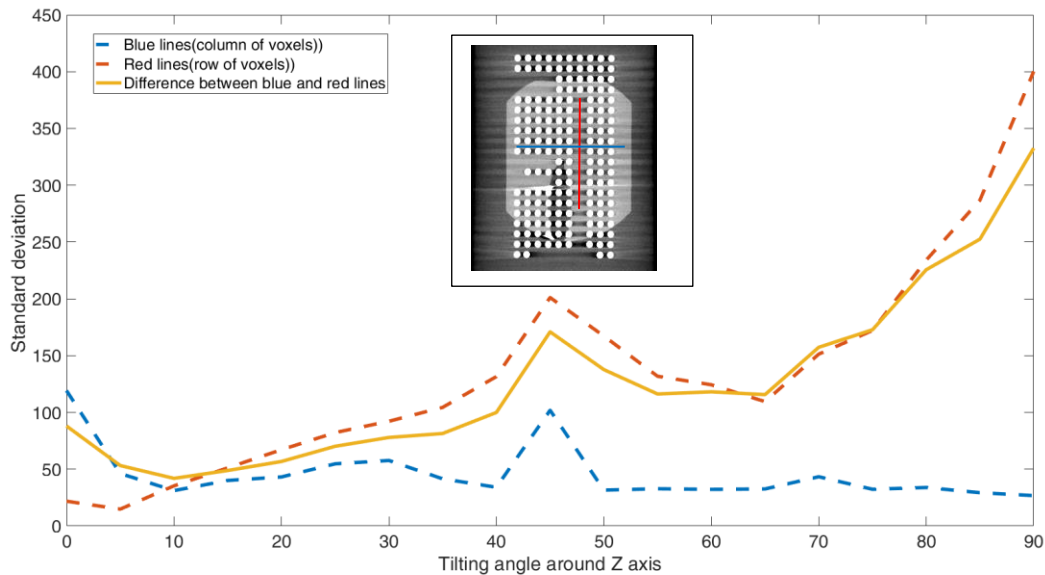


Figure 73. Standard deviation for voxels in the selected intensity profile lines at each tilt angle. Blue) Calculation for the voxels of the row pixels. Red) calculation done for the voxels of the column, Yellow) calculation for voxels in both the row and the column.

The yellow line in Figure 73 represents the total standard deviation for the voxels in the selected row and column; it provides a comprehensive comparison to the effect of the streaks at all angles. While a peak is visible in area (40- 55) degrees, two valleys can be seen surrounding the peak in areas (5- 15) degrees and (60- 67) degrees. To confirm the effects of the streaks on the gray levels throughout the epoxy, a similar calculation of the intensity profiles was performed for two other lines selected in a different area, Figure 74. While the standard deviation of the line voxels behaves almost the same as in the previous study shown in Figure 73, the column voxels behave differently with lower values of the standard deviation. The yellow line, on the other hand, which represents

the total deviation of both lines, behaves similar to the yellow curve to the previous lines presented in Figure 73, with a peak at [45-50] and two valleys with low values in the [5-10] and [60-70] ranges.

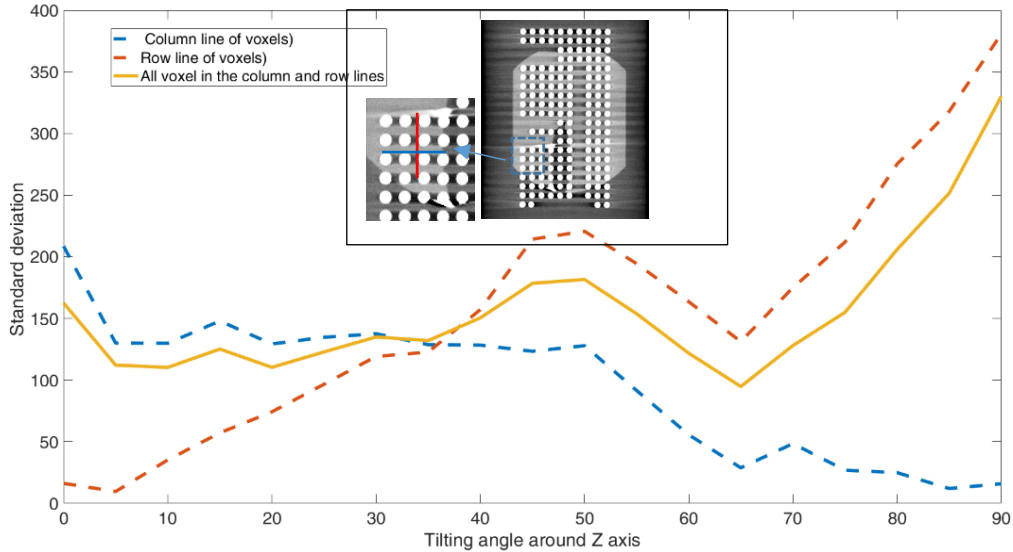


Figure 74. Standard deviation for voxels of the second selected intensity profile lines at each tilt angle. Blue) Calculation for voxels in the row. Red) Calculation for the voxels of the column, Yellow) Calculation for all voxels in the row and in the column.

Considering all the selected intensity profile lines, the standard deviation calculation shows the best results in the ranges between (5- 10) degrees and (60- 67) degrees, where the obtained volumes provide more reliable information about the epoxy layer. However, the highest standard deviation values are in the range of (35- 55) degrees. This conclusion is consistent with the visual observation of the slices presented in Figure 71, which show that the volumes at 15 degrees and 60 degrees have lower artifacts than other volumes. For further evaluation, the fused volume of all volumes is compared to the fused volume obtained from the combination of volumes in the ranges (05- 15) degrees and (55- 65) degrees.

### 6.2.3.3 Data fusion of multi-positional volumes

As can be seen in Figure 71, the "tilted" CTs of the same object have complementary information as far as metal artifacts are concerned. Therefore, a combination between these volumes results in a fused volume with corrected artifacts and lower noise Figure 75 (A). Data fusion is performed at the voxel level after a precise registration process in which the voxels of the reconstructed volumes are matched. The simplest combination to form a fused volume can be achieved by averaging the volumes, using either the main values as in the following formula.

$$Vol_{(fused,x,y,z)} = Mean(vol_{1,x,y,z} , vol_{2,x,y,z} , \dots \dots , vol_{n,x,y,z}) \quad 6.1$$

$vol_{(i,x,y,z)}$  is the voxel value of volume I at x, y, z coordinate, n total number of volumes. Using the median may give better results than the main value in the case of extreme intensity streak values, especially when combining a smaller number of volumes [61]. For an optimal combination, volumes with low intensity streaks located at different locations provide a fused volume with corrected artifacts. Therefore, the data fusion approach does not work for regions that have streaks in all combined volumes. Moreover, the degree of correction depends on the number and quality of the combined volumes, see Figure 75.

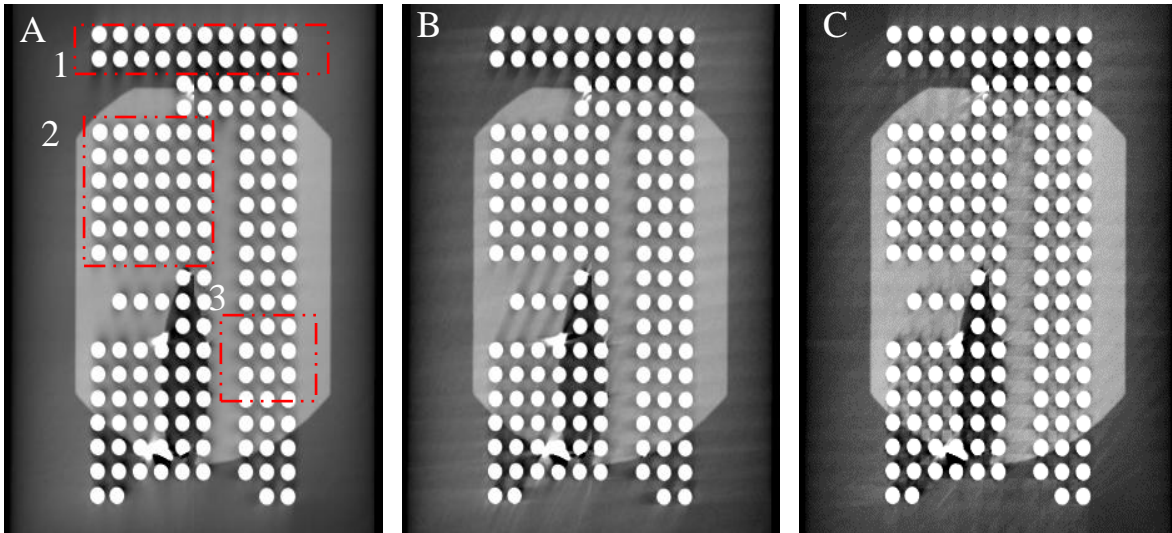


Figure 75. Slices of the fused volumes obtained from different combinations. A) Averaging of all volumes (19 in total), B) averaging of volumes at 5, 10, 60, and 65 tilt angles, C) averaging of volumes at 0, 30, 50, 85.

Figure 75 shows 3 combined volumes obtained from different combinations. The first combination includes all volumes, the second combination for volumes at (5 degrees, 10 degrees, 60 degrees, and 65 degrees), and the third combination for a randomly chosen volumes at (0 degrees, 30 degrees, 50 degrees, and 85 degrees). The fused volume of all volumes seems to be the best, the streaks are completely eliminated, the noise is reduced and the epoxy layer appears without any degradation, even in the area between the spheres where the streaks appeared strongly in the single volumes. In the case of the fused volume of the recommended combination, the streaks are slightly visible, but to a very small extent, so that a radiologist can be sure of the existence of the epoxy in this area. On the other hand, this volume looks better than the fused volume of a randomly chosen volumes, where the streaks are still pronounced despite the correction.

Quantitatively, the standard deviation of 3 selected regions of the fused volumes was calculated, see Table 6. While regions 2 and 3 have close values, region 1 has higher standard deviation values due to the highly pronounced artifacts in the open beam region. The averaged standard deviation for the three regions is reduced by 50% for the fused volume compared to individual volumes, while it is reduced by 41% for the fusion of selected volumes and by 27% for the fusion of random



volumes. Noise reduction is an additional advantage of the fusion method. According to fusion formula, the higher the number of combined volumes, the better the results.

Table 6. Standard deviation calculated for 3 different regions in the fused volumes

Std	Fused of all volumes	Fused of volumes at 5, 10, 60, 65	Fused of volumes at 0, 30, 50, 85
Region1	57	67	80
Region2	22	26	35
Region3	17	22	30
Average	32	38	48

The fused volume of the recommended combination proves the efficiency of selecting volumes in the recommended ranges. The visual comparison and noise calculation have shown that the fused volume of volumes from the recommended ranges is comparable to all volume combinations, considering the measurement time and the effort for alignment of the combined volumes.

#### 6.2.4 T2 orientation

The second type of orientation tilt (T2) is shown in Figure 68 and Figure 76 (left), where the phantom forms an angle with the horizontal plane. At 90 degrees, the BGA plane becomes parallel to the horizontal plane. The simulation was performed similarly to the T1 configuration with an angular step of 5 degrees. For visual comparison, only slices from registered CT scans with an angular step of 15 degrees are shown, since it is difficult to visually compare slices with a finer angular step, Figure 77.

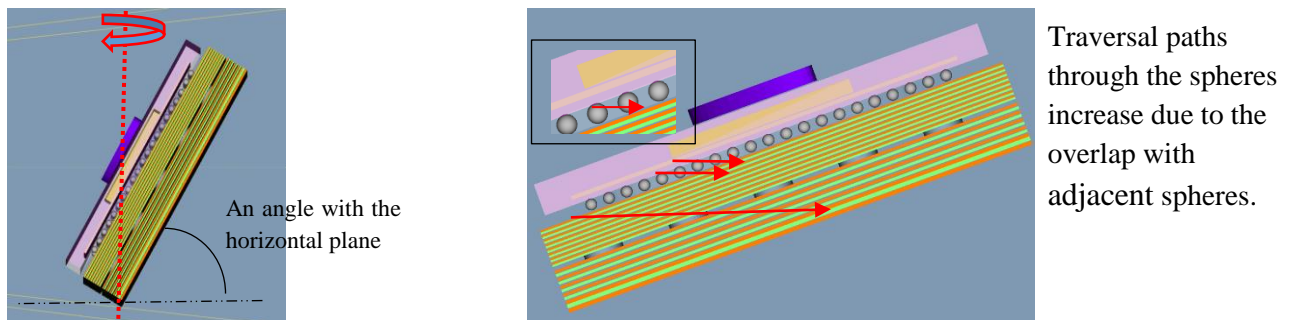


Figure 76. Left) T2 configuration. Right) Traversal-path length through the PCB and BGA spheres increases with the tilt angle. The enlarged sketch shows the increased path through 2 balls of different rows.

The black artifact streaks are in the same location for volumes obtained at (0-30) degrees, Figure 77 (A, B, C). However, the intensity of the streaks increases with increasing tilt angle besides the appearance of the white streaks. For volumes acquired with higher tilt angles, the overlap between the streaks increases the noise level and degrades the quality of the obtained CTs, see slices (D-

H). In addition to the overlap between the streaks, the frequency of generated white and black streaks also increases, affecting the gray levels in the whole image. At a tilt angle of 90 degrees, where the phantom is parallel to the horizontal plane, the overlap of the black and white streaks forms a checkerboard like pattern throughout the image. If we increase the tilt angle, the transmission paths through the BGA increase for a large number of projections. The fused volume of all volumes shown in Figure 77 (H), does not correct the streaks completely, but only the secondary streaks created by the overlap, while the main streaks are still clearly visible.

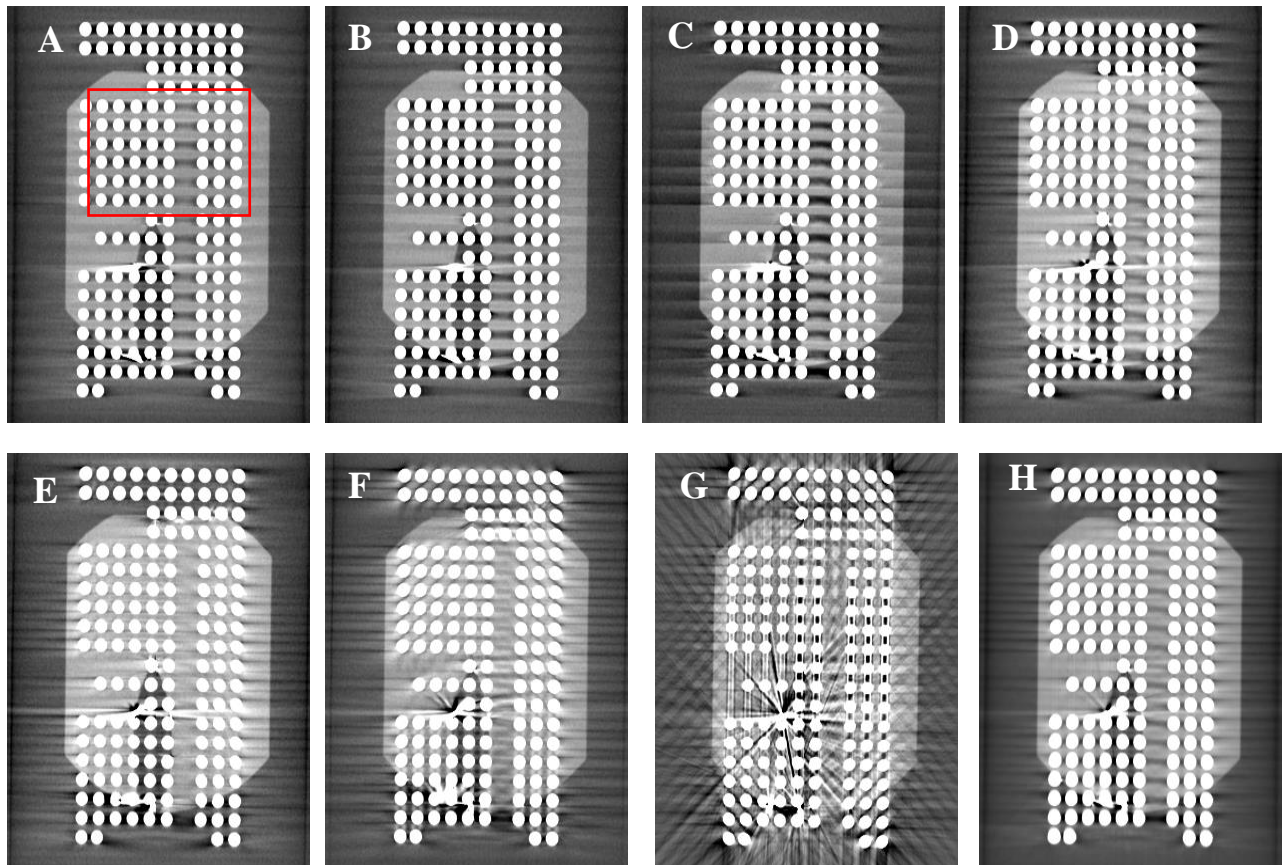


Figure 77. registered and normalized slices of the reconstructed volumes at different tilt angles. A) 0 degrees tilt, B)15 degrees C)30 degrees D)45 degrees E)60 degrees F)75 degrees G) 90 degrees, H) fused volume.

This type of tilt orientation does not change the traversal-path lengths through the BGA for projections obtained when the edge of the phantom facing the X-ray beam. However, for projections obtained with the side of the phantom facing the X-ray beam, the lengths of the transverse paths through the BGA increase due to the overlap of spheres from different rows, which hardens the spectrum, see Figure 76 on the right side.

Statistically, due to the complex shape of the artifacts caused by the overlap of the streaks, it is insufficient to use the profile intensity calculations to compare the reconstructed volumes. Therefore, the effect of the artifacts was measured by calculating the "Error" i.e., the average total deviation of each voxel from its true value using the following formula [61].

$$Error = |V_{x,y,z} - V_{True}| \quad 6.2$$

Where  $V_{x,y,z}$ : gray value of voxel (x, y, z) and  $V_{True}$  is the true voxels value.

The mean value of a region of epoxy voxels which are not affected by artifacts was chosen as a true voxels value. The region was chosen in the upper part of the epoxy layer to cover a large area of the generated artifacts at all angles. Only the epoxy voxels were considered for the "Error" calculation, the voxels related to the spheres were separated by a segmentation process. The calculated "Error" over all tilting angles values are shown in Figure 78. As can be seen in the curve, the "Error" increases slightly in the range (0-20) degrees and then increases significantly to a maximum value at 90 degrees. The overlap between two adjacent spheres from two different rows occurs at angles greater than 15 degrees, therefore the "Error" values are close to each other between (0-15) degrees with minimal value at 0 degree. The Visual comparison and the quantitative calculations show a reconstruction degradation by this type of tilt configuration. To this add, a combination of the two tilt orientations showed nosier data due to the appearance of artifacts from the both orientations. Therefore, we decided not to perform the T2 configuration on the BGA samples to implement the data fusion approach.

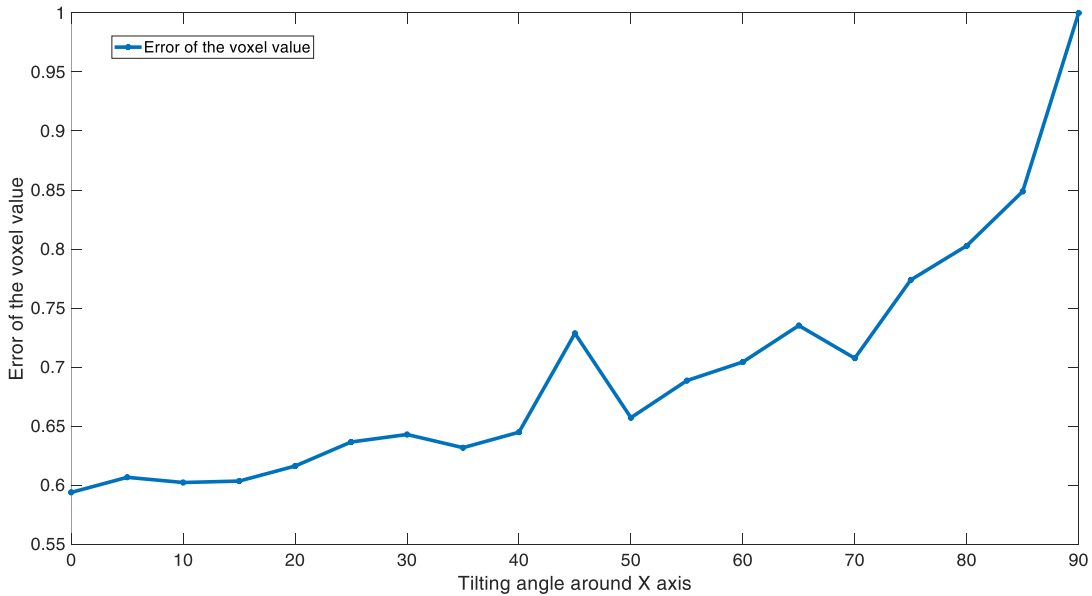


Figure 78: Error values calculated according to formula (6.2) for the selected region of epoxy in Figure 77(A).

### 6.3 Concluding remarks

Minimizing the effect of metal artifact streaks created by BGA on the contrast of an adjacent material with low attenuation (epoxy) is possible by choosing an appropriate angular orientation for the workpiece during the CT scan. Optimal orientation increases the contrast of the epoxy while reducing the intensity and frequency of the artifacts that arise. In this chapter, we presented the

results of CT simulation on a phantom resembling real BGA samples using ray casting and Radon-space analysis with a simulator called aRTist. We introduced two different tilt configurations for the phantom (T1 and T2). While T1 creates an angle between the rotation axis and the center axis of the phantom, the T2 configuration creates an angle between the center axis of the phantom and the horizontal plane. The T1 tilt configuration manipulates the traverse lengths through the BGA, resulting in improved results, while the T2 tilt configuration complicates the generated artifacts by increasing the traverse paths within the BGA. To evaluate the results, we calculated the standard deviation of selected row and column voxels, as well as the error and standard deviation for selected regions within the epoxy layer. Based on the obtained results, the best CT reconstruction can be obtained when the phantom is tilted by an angle in the ranges [5-10 or 55-65] of the T1 configuration. The fused volume of the volumes obtained from the recommended ranges emphasized the improvement obtained by comparing with fused volumes of different combinations. With the goal of minimizing the effects of metal artifacts and performing successful fusion, a choice was made between T1 and T2 orientation configurations, with only the T1 orientation used for the experimental study. For this purpose, CT scans were performed for the studied samples at angles 5, 10, 60 and 65 degrees.

## 7 Experimental part

### 7.1 Samples description and preparation

The investigation of underfill epoxy defects was performed on 9 different BGA samples. The samples were cut from different PCBs, Figure 79 (left). While some of the samples show excess epoxy on the top surface, other samples such as (2, 6 and 9) do not show excess epoxy defects on the top surface. The shape of the epoxy defects is similar for samples (1, 3, 4, and 8) and follows the underfill pattern used by the company (L-pattern, where the epoxy is applied on two perpendicular edges). The shape of the excess defects indicates unsuccessful underfilling; however, examination is required to confirm this. On the other hand, the epoxy defects of samples (5 and 7) are located on only one edge of the ICs, suggesting that underfilling may have been only partially performed (successful on only one edge). The aim of the examination of 9 samples is to correlate the shape and size of the visible epoxy defects with the invisible underfilling layer.

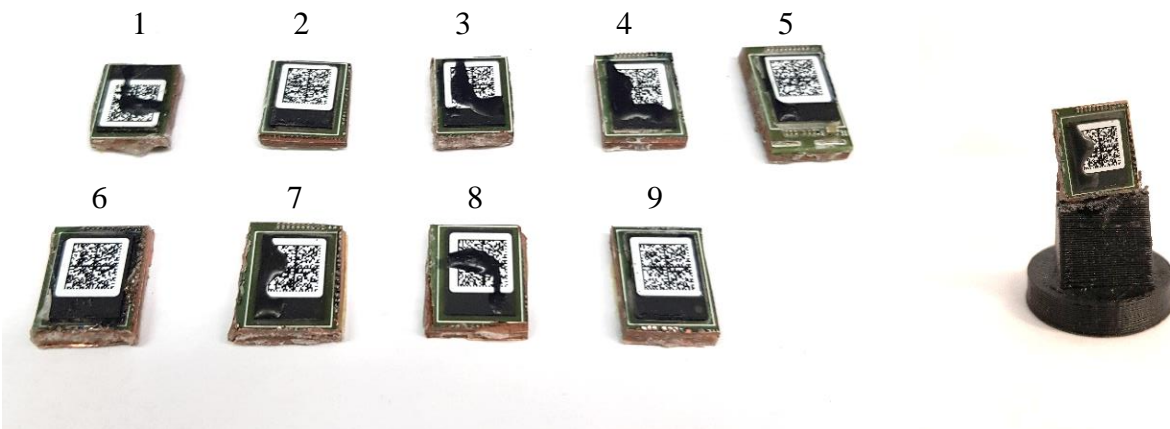


Figure 79: Left) BGA samples are ready for CT scans. Some samples show no excess epoxy on the top surface (samples 2, 6, and 9), while the others show excess epoxy defects on the top surface of the ICs. Right) The sample is mounted on a printed sample stand with a tilt angle of 10 degrees.

### 7.2 Preparation of samples and tilt stands

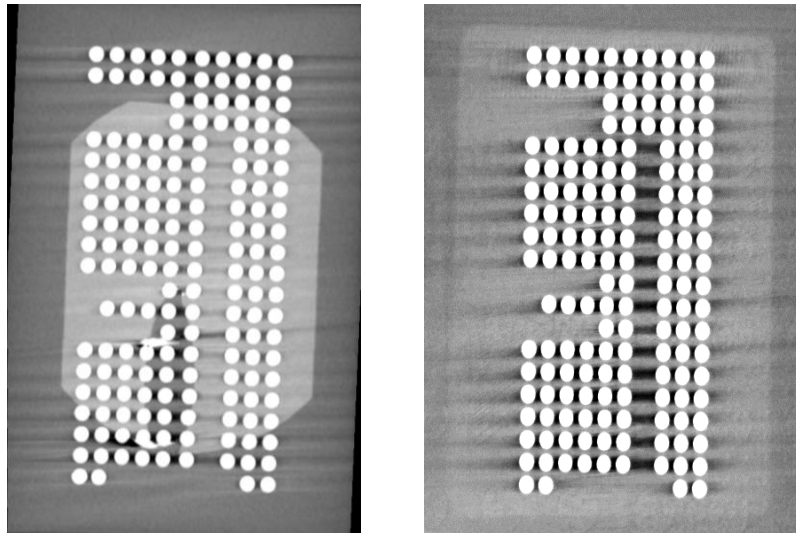
Samples were cut from large PCBs because performing CT scans for large PCBs with low-power X-ray sources is limited due to the high metal content. Nevertheless, the presented methodology allowed us to validate efficiency of the used underfilling technology. As previously mentioned, using high-power X-ray sources to perform a CT for the entire PCB is possible, but only metal parts will be visualized, while light materials such as epoxy will be omitted. Since there was no need for precise cutting, the cutting was done in the IEAP workshop using classical cutting tools, therefore the dimensions of the PCB components for the samples are in the order of a few millimeters. In order to obtain CT scans for the samples at different tilt angles, four tilt stands were printed with tilt angles (5, 10, 60 and 65). Figure 79 on the right shows a BGA sample mounted

on a 10 degree tilt stand, which in turn can be mounted on the rotation stage to obtain the desired CT scan.

### 7.3 Measurements strategy

CT scans were performed for all samples with the same geometry and irradiation parameters using IEAP's micro CT setup. The Dexela flat panel detector was chosen for these measurements because of the need to use high energy spectra. Such irradiation parameters produce high-energy photons that are difficult to detect with the silicon sensor  $Widpix_{5\times 4}$  detector.

The CT scans were done consecutively, with each sample scanned four times at different sample stands. The scans were taken at a magnification of 5 with 140 kV spectra, 165  $\mu$ A, 2mm copper filter and 1800 projections/scan (360 degree scan). The measurement was performed in a few days, with each scan lasting one hour and each sample scanned 4 times. For the reconstruction we used the filtered back projection method of VGSTUDIO MAX. Dragonfly software was used for registration that was explained in the simulation section.



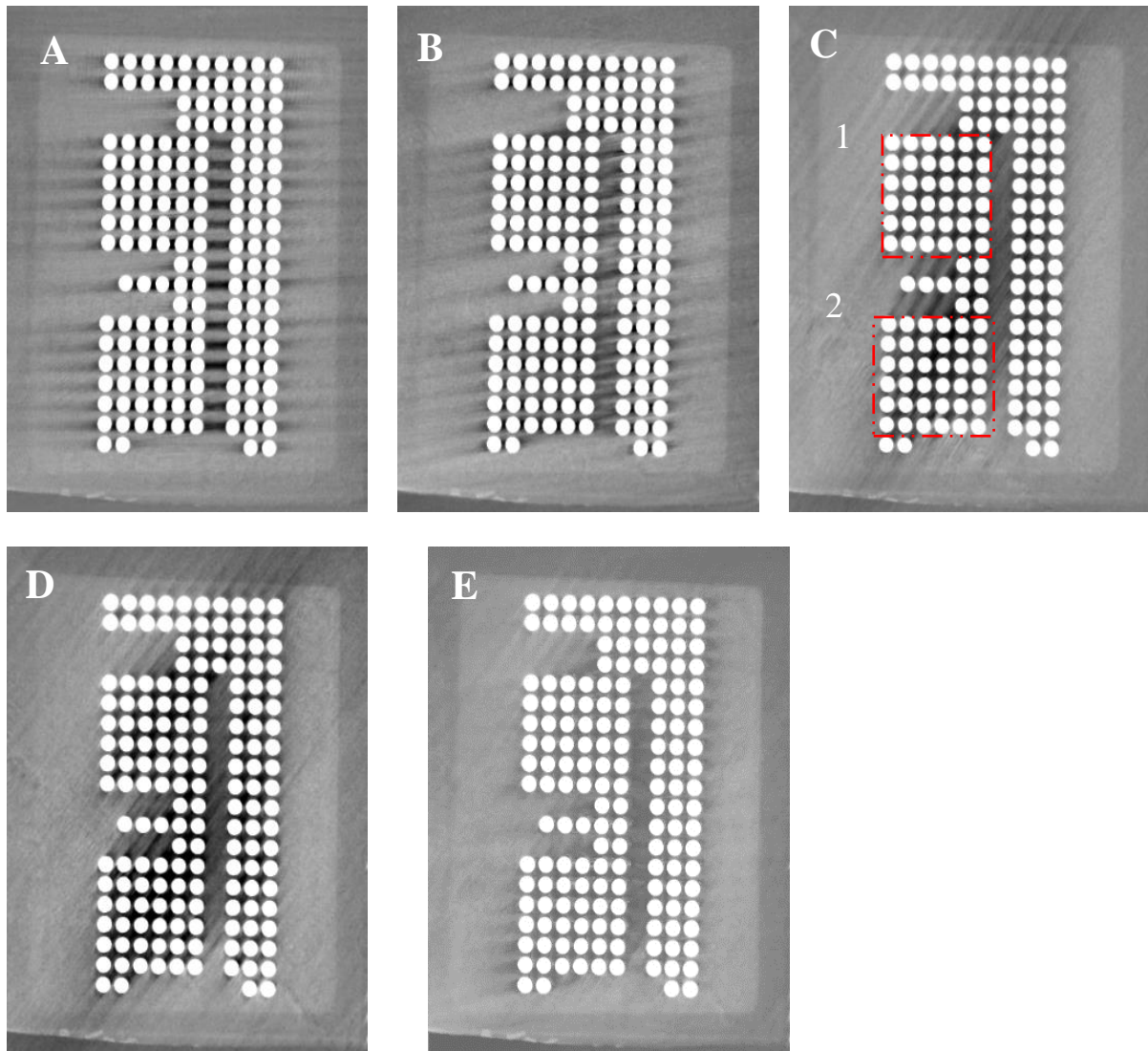
*Figure 80: Slices of the simulated phantom (left) and sample 2(right) show a higher contrast for the simulated epoxy compared to the epoxy used in the real samples.*

#### 7.3.1 Experimental results vs simulation

Although the simulated phantom was modeled similarly to the real samples, few differences were found when we analyzed the reconstructed volumes of the experimental data. First, the contrast of the epoxy resin is higher in the simulated results than in the experimental results, which is due to the fact that a silica-filled adhesive resin was chosen for the phantom calculation beside the scattered photons which could not be calculated by the simulation, Figure 80. For comparison, we calculated the CNR values for selected areas of the epoxy resin for the reconstructed volumes of the phantom and sample 2. The CNR value for the epoxy resin in the phantom is 16.8, while the CNR value for the detected epoxy resin in sample 2 is 6.6. This value is 2.5 times lower than the

simulated results. Nevertheless, to obtain a complete shape of the epoxy resin, a fusion approach is required to increase the contrast of the epoxy resin, especially at the edges.

CT scans of the real samples are noisier than the simulated CT scans, which did not take into account the scattered photons among other noise sources. Finally, the spacing between the spheres in the real samples is tens of microns less than in the phantom due to the imperfect soldering process. All the above differences have affected the quality of the results of the real measurements compared to the simulated results.



*Figure 81. Slices of the reconstructed volumes for the sample 2 at different tilt angles. The slices show the BGA and the underfilling epoxy layer. A) 5 degrees, B) 10 degrees, C) 60 degrees, D) 65 degrees, E) fused volume.*

### 7.3.2 CT Reconstruction enhancement using DFMCT

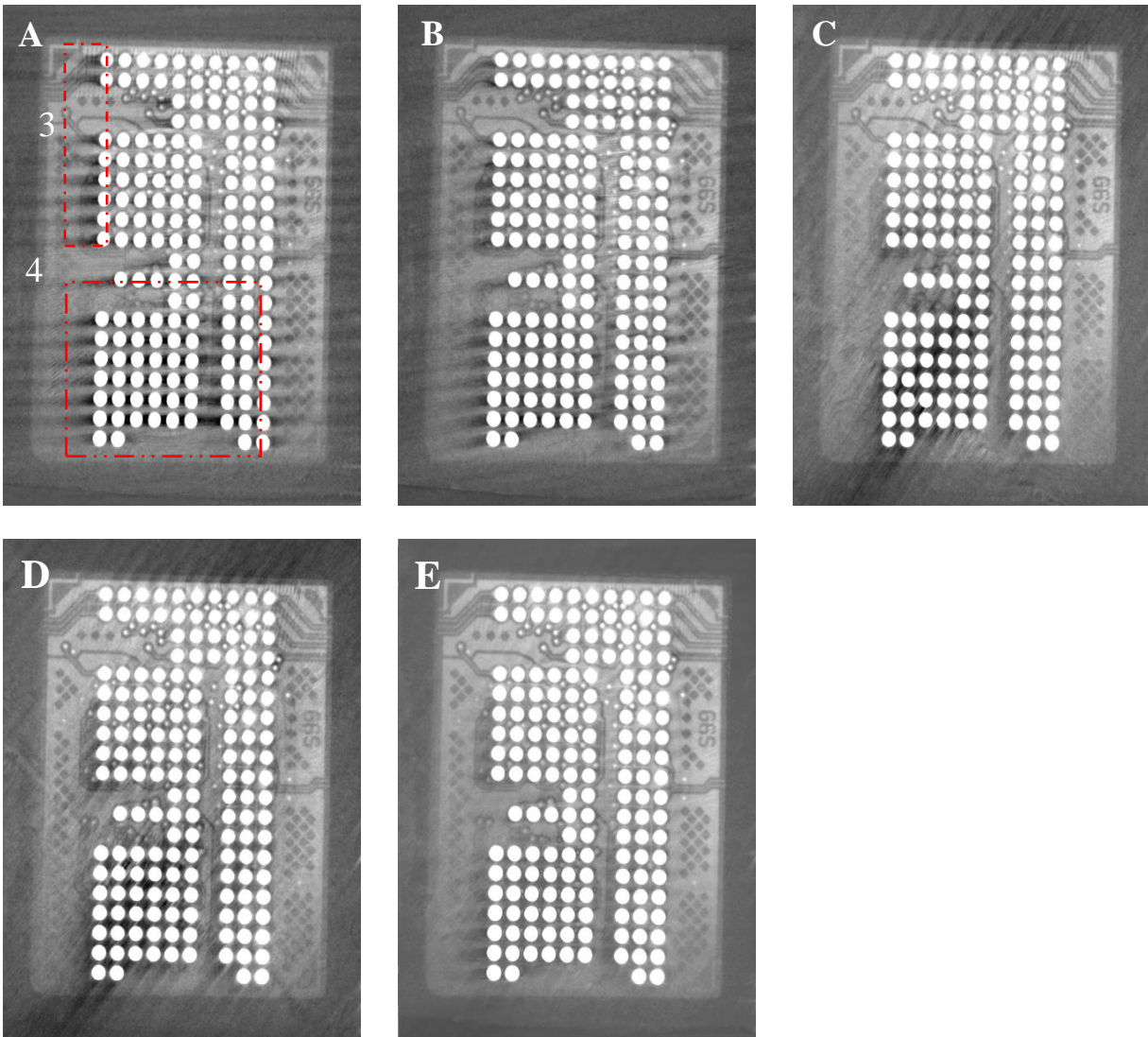
To demonstrate the differences between the reconstructed volumes at different mounting positions and the enhancement achieved by the fusion approach, we will present slices of the reconstructed volumes for sample 2 at angles 5, 10, 60, and 65 for discussion. The other scanned samples behave the same way, so we choose only one sample for comparison. However, the final fused volumes alongside the segmented volumes of all samples are presented in the next section.

Figure 81 shows slices of the reconstructed volumes at the BGA level. The slices show the BGA, the detected epoxy layer with low contrast compared to the surrounding air regions (air+PCB), and the metal artifact streaks at various locations. Despite the artifacts, the volumes show complementary information about the distribution of the epoxy. The difference between volumes 5 and 10 is clearly visible in terms of intensity and location of the generated streaks. The streaks in volume 5 tend to appear stronger but concentrated in narrow bands, while the same streaks in volume 10 appear weaker but more frequent, Figure 81 (A and B). Volumes 60 and 65 show streaks with higher intensity in the upper left and lower left blocks of the spheres, regions 1 and 2 in Figure 81 (C and D). However, the contrast in these regions is corrected using the intensity values of the volumes (5 and 10). For volumes 60 and 65, the streaks disappear far from the above mentioned block of spheres, which corrects the streaks in these regions for volumes 5 and 10, Figure 81 (A and B).

For all volumes, the epoxy contrast on the left side of the BGA is very low, especially for volumes 60 and 65, where the epoxy edges are not clearly visible. Therefore, data fusion of several volumes is necessary to visualize the final shape of the underfill epoxy and to correct the streaks. The fused volume is shown in Figure 81 (E), in which the noise was reduced, the streaks were corrected, and the epoxy contrast was increased. Since the real measurements showed stronger artifacts than the simulation, the fusion was performed in a slightly different way. First, we calculated the median volume of all volumes and then corrected the disturbed voxels between the spheres by interpolating from the non-disturbed surrounding voxels. For the interpolation, we used a 3-D kernel of size (3×3 voxels) and only voxels with values above a predefined threshold were considered for the calculation. The threshold was taken as the mean intensity value of voxels of epoxy without artifacts. Despite the increased contrast in the region between the spheres, confirming the existence of epoxy comes with relative uncertainty.

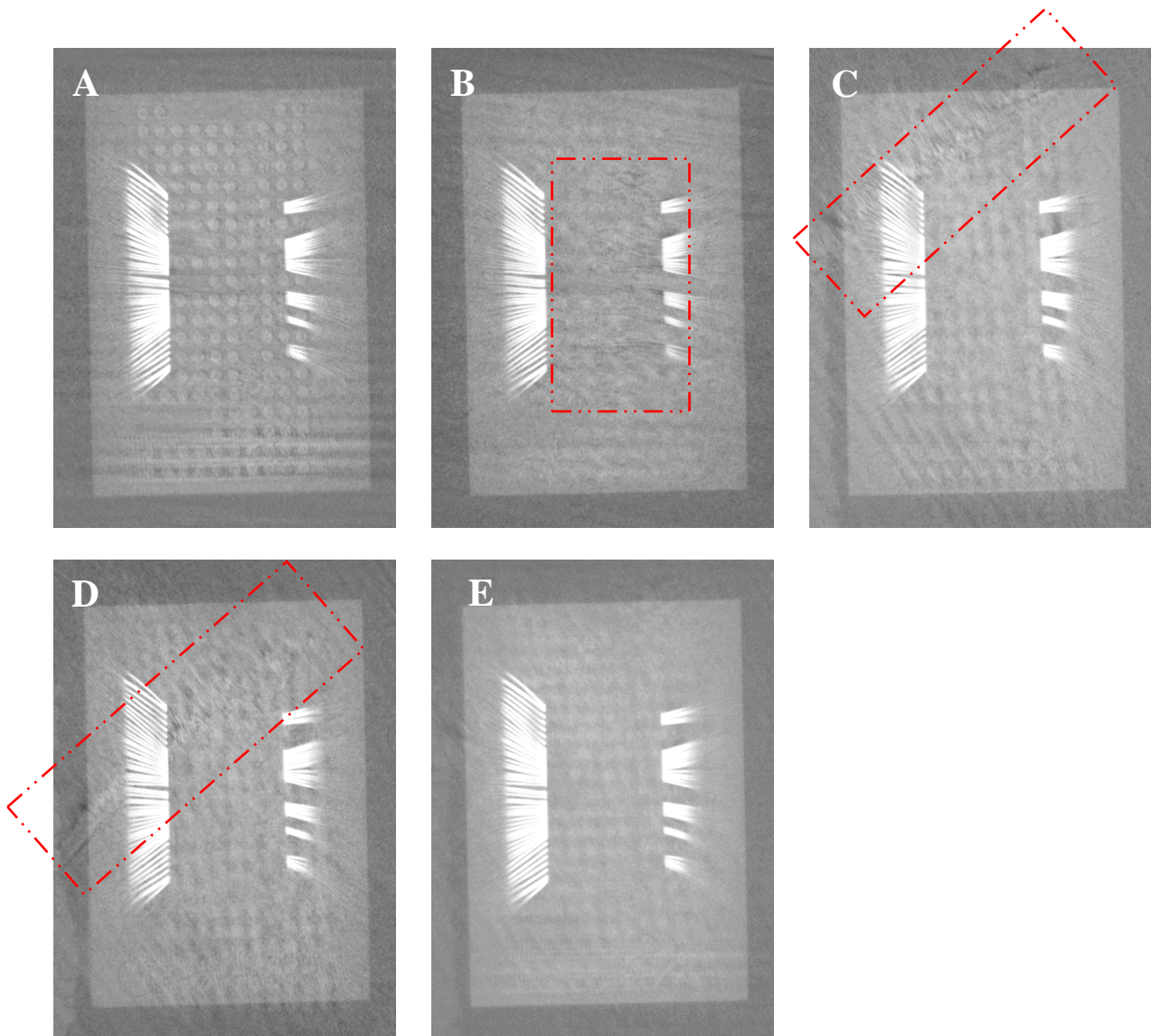
Another set of slices is shown in Figure 82 to demonstrate the improvement achieved by the fusion. The slices were taken at the interface between the BGA and the IC substrate. The effect of the metal streaks is remarkable, especially in region 3 and region 4 for all slices. The streaks in the fused slice are corrected, and the slice appears smooth and less noisy, even in regions 3 and 4.





*Figure 82: Slices of the reconstructed volumes for the sample 2 at different tilt angles. The slices show the BGA and the IC substrate. A) 5 degrees, B) 10 degrees, C) 60 degrees, D) 65 degrees, E) fused volume.*

The last selected set of slices are demonstrated in Figure 83. The slices were taken at the upper part of the IC substrate, they show wires besides the IC casting. Different types of artifacts are visible in the slices, for instance slice A demonstrate metal artifacts which appear similar to the BGA pattern. On the other hand, slice B appears noisy in the region defined by the rectangle. Slice C and D demonstrate same type of a noise as frequent waves in the defined regions by the rectangles too. The fused slice on the other hand shows significant improvement in the contrast where all the artifacts demonstrated in the single slices were eliminated.



*Figure 83: Slices of the reconstructed volumes for sample 2 at different tilt angles, the slices show the upper part of the IC and the wire bonding. A) 5 degrees, B) 10 degrees, C) 60 degrees, D) 65 degrees, E) fused volume*

The contrast enhancement is also visible in sample No. 1, the first sample examined for epoxy resin. The sample was contaminated by the adhesive material (glue) used to attach the sample to the stands. Although we knew that the adhesive had leaked between the balls, we arranged for the DFMCT measurement to see if we were able to distinguish between the adhesive and the epoxy underfill. The results obtained by the DFMCT approach proved that the contrast can be improved for materials with low attenuation to be able to distinguish them.

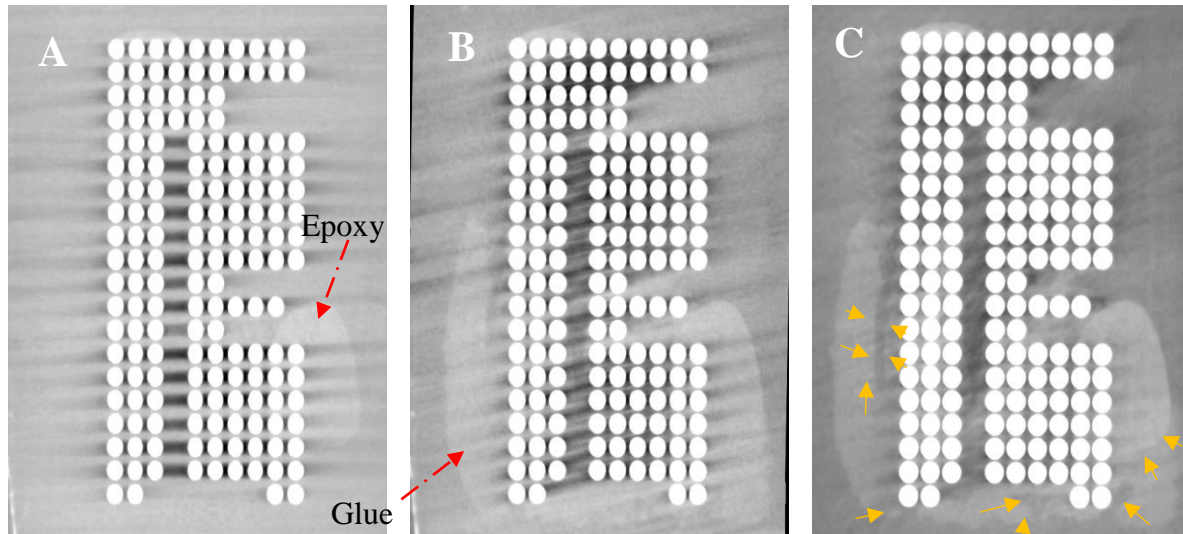


Figure 84: Slices of sample 1 showing the contrast enhancement achieved by the fusion approach. A) Uncontaminated sample in which the epoxy resin is visible as a drop on the right side. B) Sample contaminated with adhesive (glue). The glue has the same contrast as the underfill. C) Fused slice showing a slight difference in contrast between the epoxy underfill and the glue (yellow arrows point to both materials).

Figure 84 shows slices of the sample 1 before and after contamination. Slice (A) shows the results of the sample before contamination, where the epoxy underfill appears as a drop on the right side of the BGA.

On the other hand, slice (B) is contaminated by the glue, which has a similar contrast to the epoxy underfill. It is difficult to distinguish the epoxy from the glue in slice B. The fused slice (C) shows the epoxy droplet with higher contrast than the glue, and an air pocket can also be seen in the glue. Later, we performed a destructive planer cut to verify our inspection. Visual inspection of the underfilled epoxy after the cut is consistent with the data fusion results.

#### 7.4 Fused volumes of the scanned samples.

After the success of the fusion approach to correct the metal artifact streaks and visualize the underfilling epoxy, the samples were measured and processed by repeating the following steps:

1. Four CT scans at tilt angles (5, 10, 60, and 65) degrees under the same irradiation geometries.
2. Reconstruction of the CT scans using filtered back projections method.
3. Registration of the volumes using Dragonfly software. Registration includes rotation, scaling, and transformation using mutual information and linear interpolation.
4. Normalization of the reconstructed volumes to compensate for differences caused by the reconstruction algorithms due to different geometries. The normalization was done by scaling the intensity values for air and epoxy areas.

5. Combining the registered volumes by finding the median voxel-wise and then correcting perturbed voxels by interpolation.
6. Segmenting the fused volumes to demonstrate the distribution of the epoxy layer and visualize the excess epoxy defects.
7. Calculating the size of the underfilling epoxy and the excess epoxy on the top of the IC.

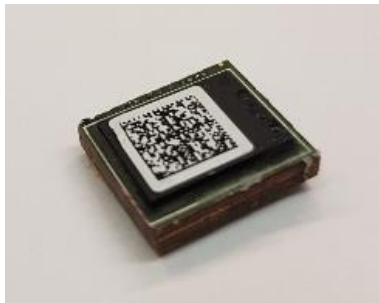
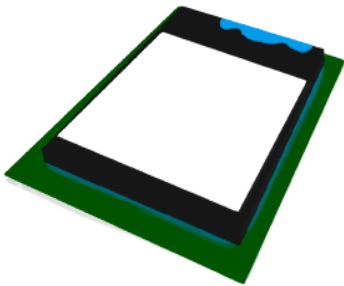
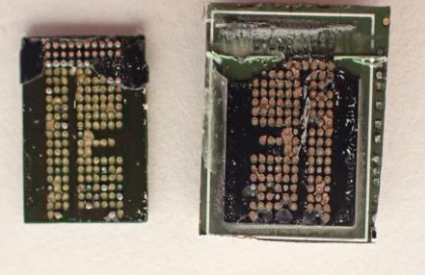
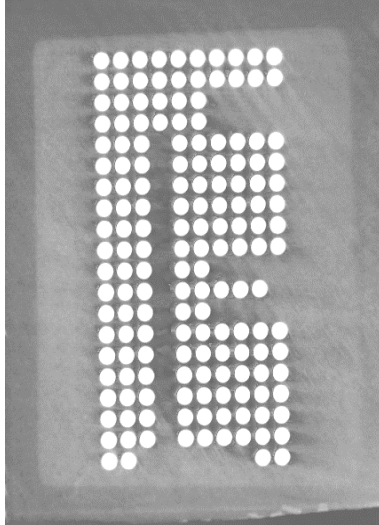
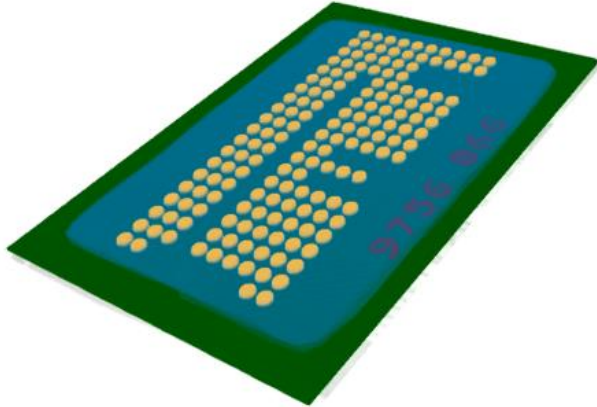
## 7.5 Experimental results and segmented-fused volumes

The measurements aimed to study the underfilling process and to establish a correlation between the excess epoxy on the top surface and the quality of the underfilling. Therefore, we divided the samples into two main groups, the first group for samples with no/with little excess epoxy on the top surface and the second group for samples showing excess epoxy on the top surface. For each sample, we presented a slice of the fused volume, 3D volumes manually segmented using human inception, and for some of the samples, a destructive planar cross-sectional photograph. For segmentation, we followed the same color coding, with the epoxy labeled in light blue, the PCB in green, the chip number in red, IC in black, the BGA in dark yellow, and the top label in white. It is worth noting that the segmentation was done manually with Dragonfly software, using human intelligence to distinguish the surrounding materials based on contrast information. In this section, the numbering used in Figure 79 was used; however, the samples are also defined by the chip number visible in the reconstructed volumes.

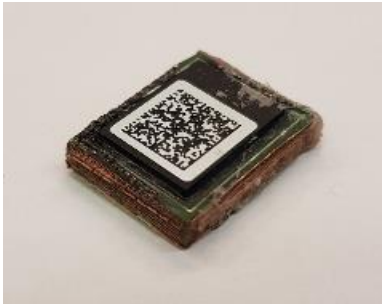
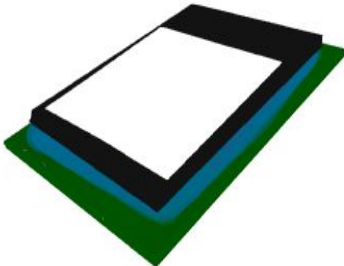
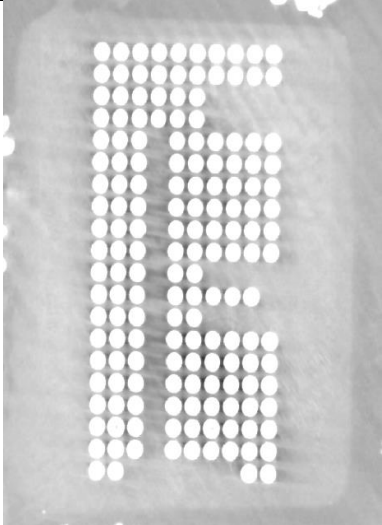
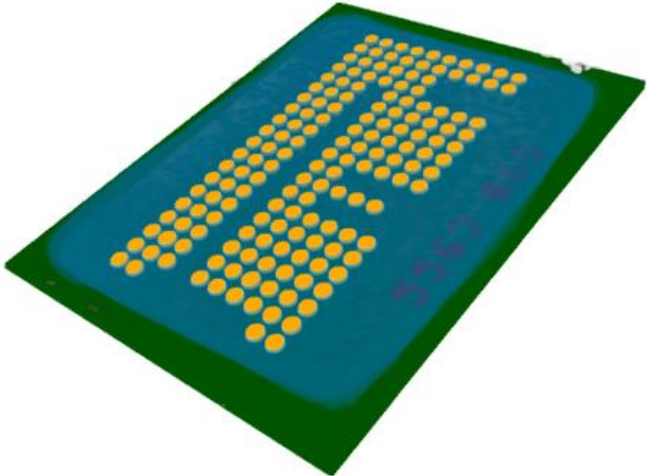
### 7.5.1 Samples without excess epoxy resin (negligible amount of epoxy resin)

Only samples (2, 6, and 9) show no epoxy defects on the top of the ICs. However, the CT reconstruction for these samples revealed a negligible amount of epoxy on the top surface, especially at the edges of the IC.


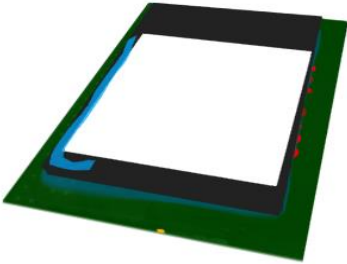
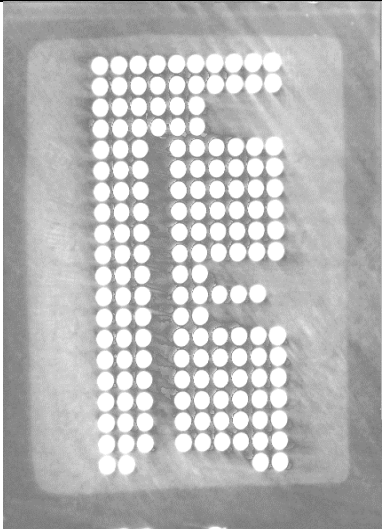
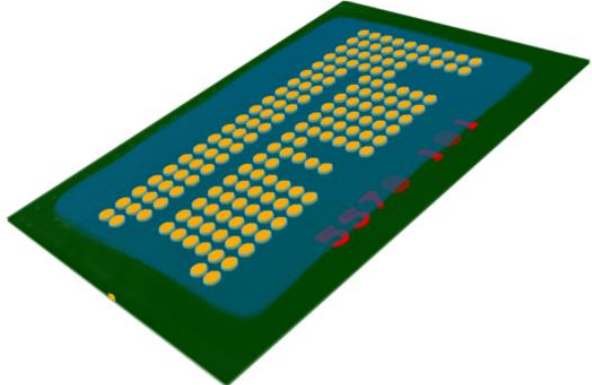
**Sample 2**, chip number 9756066, is completely underfilled, with the entire area below the IC filled with epoxy. There is a small amount of excess epoxy on the top surface, representing 2% of the underfill layer. The epoxy defect is only on one edge, indicating contact between the probe and IC during the movement of the probe to deliver the second edge. The fused volume showed the epoxy layer in a rectangular shape with dimensions of 6.9 mm × 11 mm, which corresponds to the dimensions of IC. The epoxy layer was visible in six consecutive slices, which resulted in a total thickness of ~120 μm. Further information on the epoxy distribution is given in Table 7.

Photography	3D manually segmented tomography	Destructive cross-section
		
<p>Slice of the fused volume</p>	<p>Cross-section in the segmented tomographic volume</p>	
		

**Sample 6**, chip number 5569068, is completely underfilled with no excess epoxy on top. The underfilled epoxy extends over the entire circuit board on the left side, which can be seen in the fused slice. The 3D representation, on the other hand, has been cropped to avoid the metal parts on the left side. The length of the underfill layer is 10.7 mm and the width is 8.4 mm, which is 1.4 mm more than the width of IC. The average thickness is 140  $\mu\text{m}$ . For more information about the epoxy resin distribution, see Table 7.

Photography	3D segmented manually tomography
	
Slice of the fused volume	Cross-section in the segmented tomographic volume
	

**Sample 9**, chip number 5570101, completely filled with epoxy, with the entire area below the IC filled. A bar of excess epoxy can be seen on the left edge of the IC (~3% of the demonstrated underfill epoxy). The dimensions of the underfilled epoxy are 7.1 mm × 11 mm with a total thickness of 120 μm. More information about the epoxy distribution can be found in Table 7.

Photography	3D segmented manuallytomography
	
Slice of the fused volume	Cross-section in the segmented tomographic volume
	

### 7.5.2 Samples with excess epoxy defects:


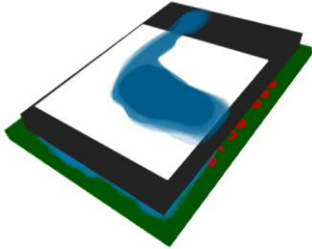
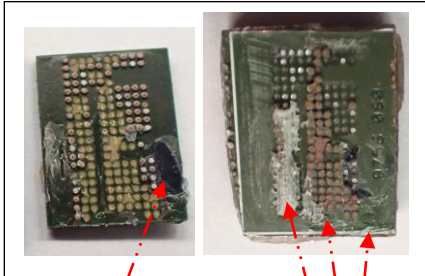
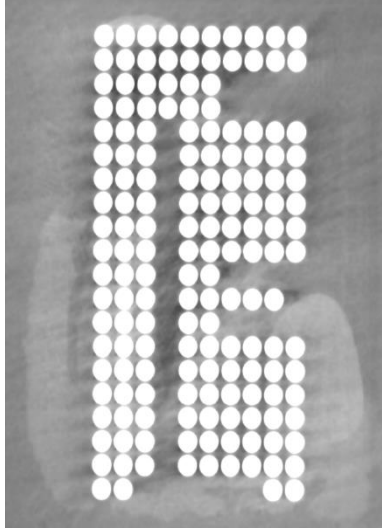
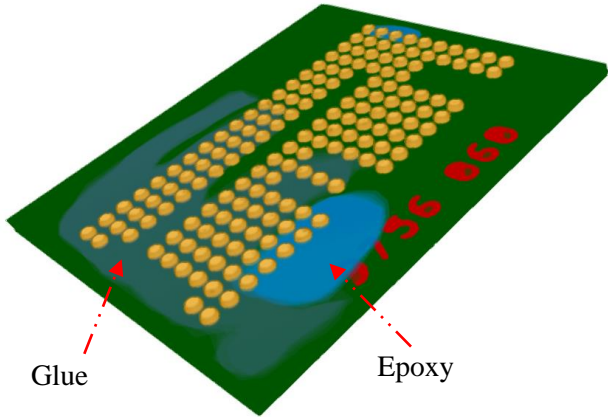
This group is divided into two subgroups with respect to the amount of filling, since the results show that some samples have a small amount of underfilled epoxy that is not related to the underfilling process.

#### 7.5.2.1 Non-filled samples:

This subgroup of samples shows that the excess epoxy defects have the same shape (L-shape), indicating that the probe dispensed the entire amount of epoxy on the top surface. The fused

volumes of the samples showed a small amount of epoxy between the IC and the PCB, later the 3D rendering showed that the epoxy flowed down from the top and covered small areas under the ICs. Therefore, underfilling is considered a failure for these samples.

**Sample 1**, chip number 9756060, unsuccessful filling procedure, and the sample was contaminated by the glue used to attach the sample to the stands. Thanks to data fusion, we were able to distinguish the epoxy underfill from the glue. The epoxy droplet in the center of the right side of the BGA leaked from the excess epoxy on the top. The shape of the excess epoxy is L - shaped and the amount of epoxy on the top is ~57% of the free space between the BGAs, For more information about the epoxy resin distribution, see Table 7.

Photography	3D manually segmented tomography	Destructive cross-section
		 <p data-bbox="998 1119 1161 1150">Drop of Epoxy</p> <p data-bbox="1239 1119 1372 1150">White glue</p>
Slice of the fused volume	Cross-section in the segmented 3D volume	
	 <p data-bbox="797 1696 857 1728">Glue</p> <p data-bbox="1138 1696 1214 1728">Epoxy</p>	

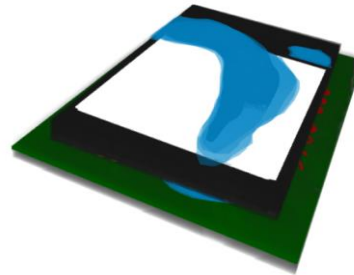


**Sample 3**, chip number 9756060, unsuccessful filling process, and the BGA area is empty except for a few drops of epoxy resin on the edges of the IC. The drops of underfilled epoxy have leaked from the excess epoxy resin on the top of IC. The shape of the epoxy defect is L-shaped and the amount of epoxy on the top corresponds to ~50% of the free space between the BGAs. The rest of epoxy are distributed on the PCB.

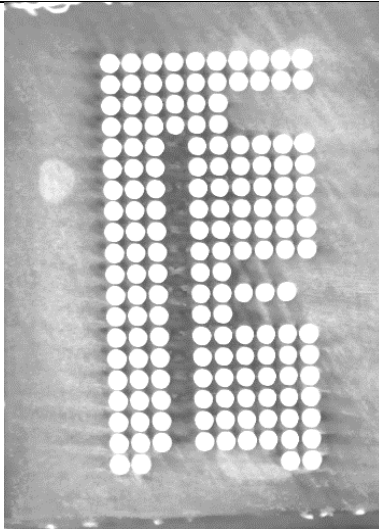
**Photography**



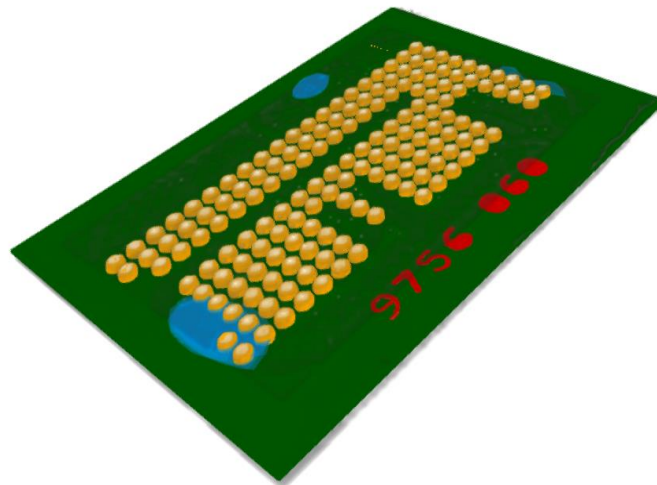
**3D manually segmented tomography**



**Slice in the fused volume**

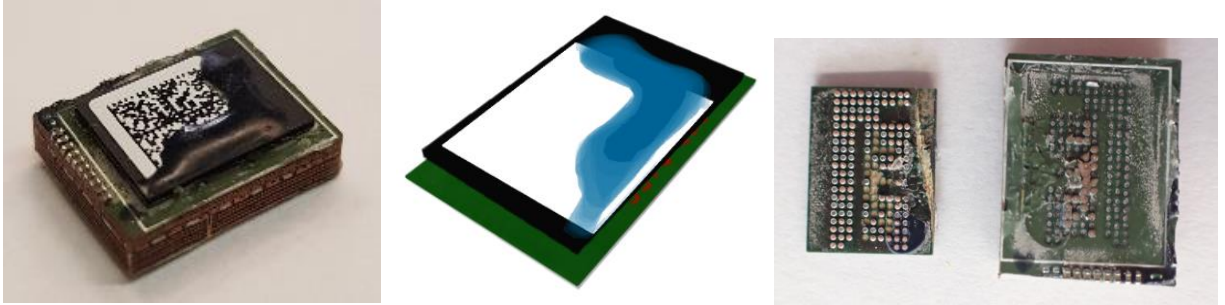


**Cross-section in the segmented tomographic volume**

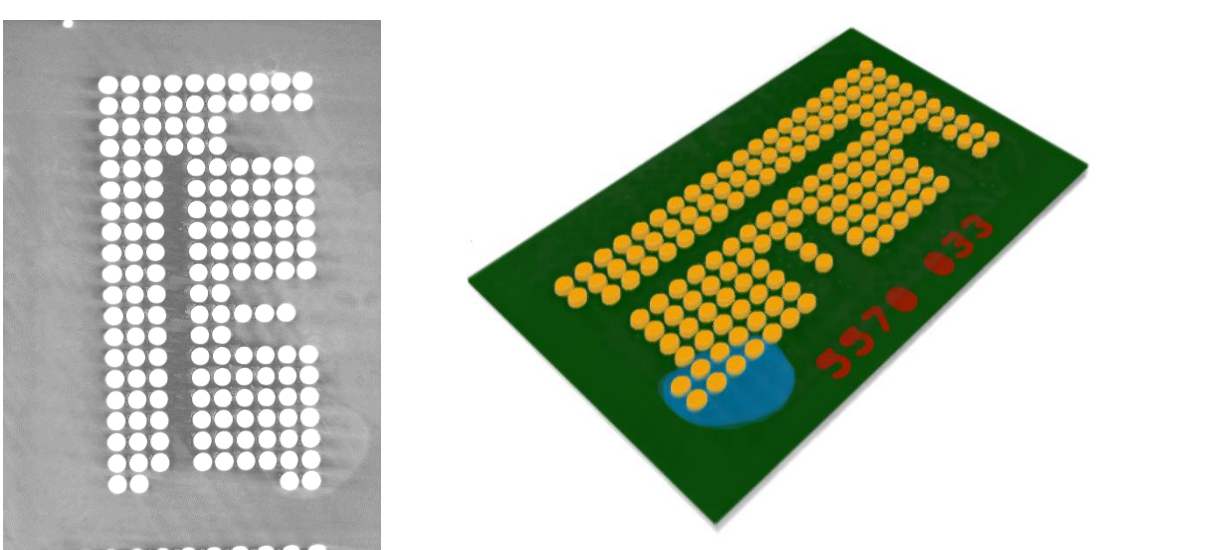


**Sample 4**, chip number 5570 033, unsuccessful filling procedure, the BGA area is empty except for a drop of epoxy at the lower right corner of IC. The underfilled epoxy drop has leaked from the excess epoxy at the top of the IC. The epoxy shape is L and the amount of epoxy at the top is ~81% of the free space between BGA.

<b>Photography</b>	<b>3D manually segmented tomography</b>	<b>Destructive cross-section</b>
--------------------	---	----------------------------------



<b>Slice in the fused volume</b>	<b>Cross-section in the segmented tomographic volume</b>
----------------------------------	--

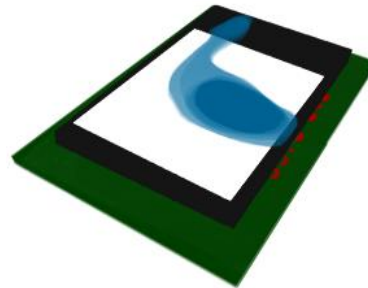


**Sample 8**, chip number 5570048, unsuccessful filling process, and the BGA area is empty except for one drop of epoxy on the middle to the right side of the IC. The underfilling epoxy drop has leaked from the excess epoxy on the top of the IC. The epoxy shape is L and the amount of the epoxy on the top is ~49% of the free space between BGA.

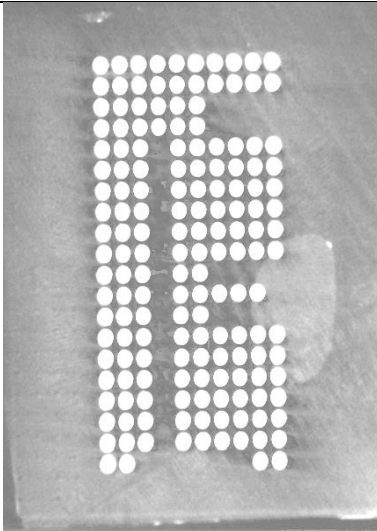
**Photography**



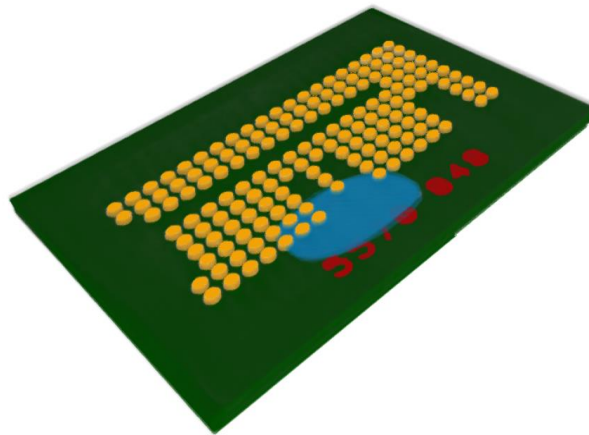
**3D manually segmented tomography**



**Slice in the fused volume**



**Cross-section in the segmented tomographic volume**


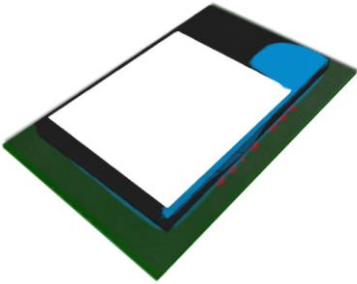
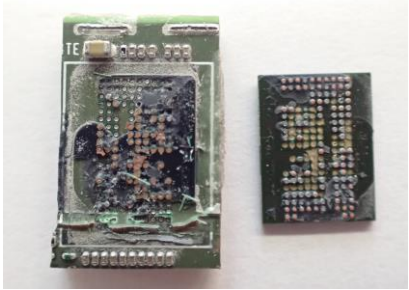
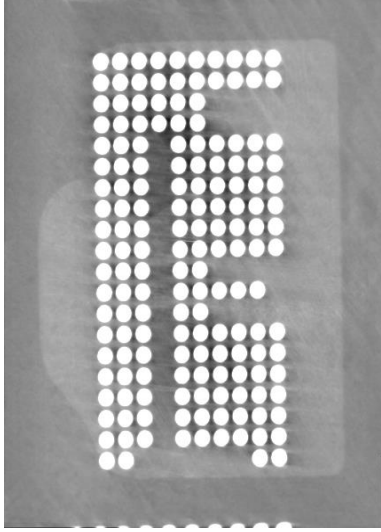
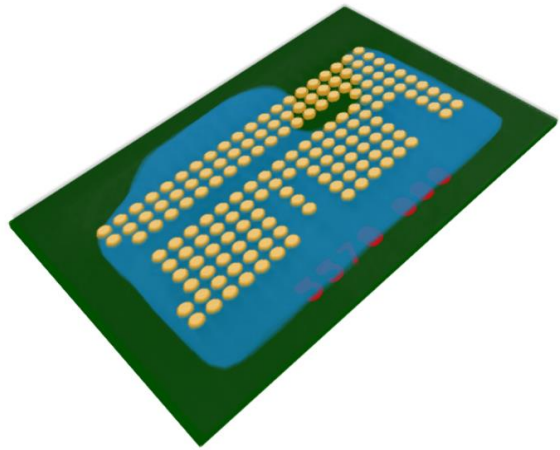


### 7.5.2.2 Samples with partial filling

This subset of samples shows the excess epoxy defects on one edge of the IC. The (I) shape of the epoxy defects indicates that the probe dispensed the epoxy correctly to one edge, while the remaining amount of epoxy was applied to the top of the IC. However, the samples showed that

the amount of excess epoxy and detected epoxy between the BGA is almost equal to the space between the IC and the PCB.

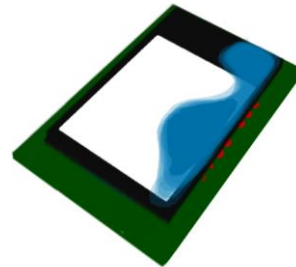
**Sample 5**, chip number 5570 088, is partially filled with epoxy, with the underfill on the left side of the BGA missing from the top and bottom corners. The excess epoxy resin follows the (I) shape and is heavily present on the upper right corner of the IC with a long epoxy resin strip on the vertical edge where the probe should apply the epoxy resin. The amount of epoxy on the top is ~25% of the free space between the BGAs and the fill ratio is 72%.

Photography	3D manually segmented tomography	Destructive cross-section
		
Slice in the fused volume	Cross-section in the segmented tomographic volume	
		

**Sample 7**, chip number 9756 002, is partially filled with epoxy resin. The lower and upper parts of the BGA are underfilled with epoxy, while the middle part is empty. The shape of the excess epoxy resin is (I), and the epoxy resin is strongly located at the right edge of the IC. The amount of epoxy on the top is ~56% of the free space between the BGAs and the filling ratio is 49%.

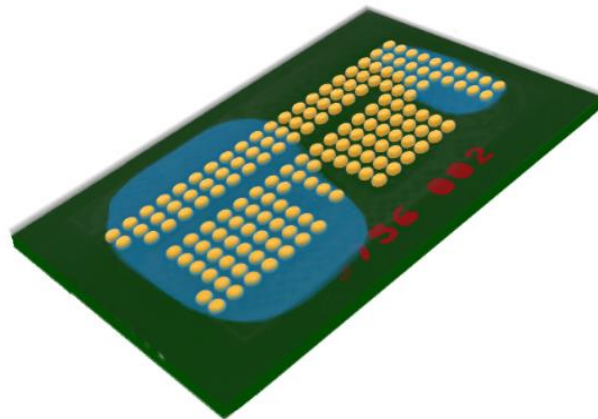
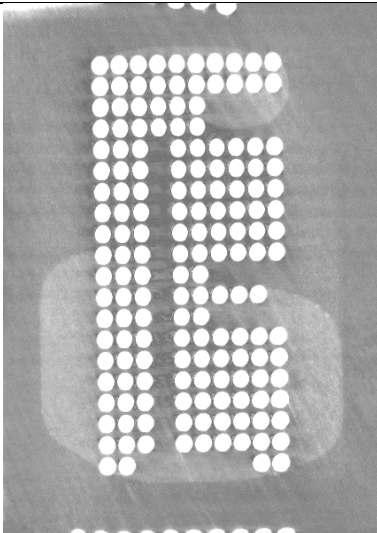
**Photography**

**3D manually segmented tomography**



**Slice in the fused volume**

**Cross-section in the segmented tomographic volume**



## 7.6 Discussion and interpretation about the excess epoxy defects

Using the data fusion approach, we successfully investigated the underfilling epoxy resin for nine different BGA samples. The results showed a correlation between the shape of the epoxy defects on the top surface of the ICs and the success of the applied underfilling process. Depending on the

shape of the excess epoxy defects, the samples were divided into three groups. The first group includes the samples (2, 6, and 9) that do not show any epoxy defects upon visual inspection. However, the reconstructed volumes of the samples (2 and 9) showed a small bars of epoxy defects at the edges of the ICs. The calculation of the volume of the detected epoxy defects and the underfilled epoxy showed that we can neglect the detected small amount of excess epoxy defect (both are less than 2%). Sample 6 also has no defects on the top surface in the reconstructed volume. This group of samples (2, 6, and 9) was successfully underfilled with epoxy; consequently, the percentage of underfilling is 105%, 111%, and 101%. For the underfill calculation, we took the space between IC and the PCB, which should actually be underfilled, as a reference; therefore, the percentage of underfill for these samples is over 100%.

*Table 7. underfilling parameters obtained from the experimental study for nine different BGA samples*

Sample number	Type of filling	Shape of the defect	Epoxy defect(mm <sup>3</sup> )	Underfilling epoxy(mm <sup>3</sup> )	Volume between IC and PCB (mm <sup>3</sup> )	Fill percentage
1	<b>Not filled</b>	L	4.64	0.42	7.7	5%
2	<b>Completely</b>	~	0.225	7.78	7.40	105%
3	<b>Not filled</b>	L	3.82	0.252	7.67	3%
4	<b>Not filled</b>	L	6.1	0.301	7.55	4%
5	<b>Partially</b>	I	1.89	5.46	7.48	72%
6	<b>Completely</b>	~	~	8.4	7.55	111%
7	<b>Partially</b>	I	4.313	3.78	7.6	49%
8	<b>Not filled</b>	L	3.78	0.632	7.71	7%
9	<b>Completely</b>	~	0.234	7.65	7.55	101%

The second group of samples are unsuccessful underfilled samples (1, 3, 4, and 8) where the process did not occur, but the probe deposited the epoxy resin on the top of the ICs as excess epoxy defects. The epoxy defects on these samples look similar to the (L) shape used as the dispensing sample, indicating a miss-dispensing process on both edges of the IC. The fused volume of these samples shows the existence of some drops of epoxy under the ICs at the edges, the drops have flowed from the excess epoxy defects on the surface. The amount of epoxy on the top surface of the samples (3 and 8) is 50% of the space between the spheres, while the amount of excess epoxy on samples 1 and 4 is consequently 60% and 80%. In some cases, the probe dispenses the epoxy resin on different components of the board next to the ICs.

The third group of samples includes the samples (5 and 7) that are partially underfilled with a filling ratio of ~49% and ~72%, respectively. The calculation for each sample showed that the amount of excess epoxy next to the underfilled epoxy corresponds to the empty space between IC and the PCB. The samples have bars of epoxy on only one edge, indicating that the underfilling was done correctly on one edge, while the rest of the epoxy was incorrectly distributed on the surface.

The main conclusion from the measurements is that visual inspection of epoxy defects can be considered an indicative of an unsuccessful underfilling procedure. Such conclusion is important for practice after careful checking as was shown in this study. While large defects indicate that there is no epoxy layer between the BGAs, the small defects in bar form indicate partial filling with epoxy [74].

## 8 Conclusions

This work deals with new methods for the inspection of complex objects using X-ray computed tomography. The objective was to improve the performance of X-ray imaging modalities by enhancing the capabilities of computed tomography in combination with appropriate approaches and data processing techniques. Improved results were presented in terms of material separation and defect inspection for the microelectronic industry that can be applied in production lines.

This work was initially devoted in part to the advanced features of Timepix's photon-counting detectors, which enable energy-sensitive imaging to distinguish the material components of objects. Multi-bin computed tomography was selected for material resolving of limited size samples. Here, the sample was scanned several times with different thresholds to obtain reconstructed volumes as a function of different bins of the X-ray spectrum. For this purpose, we proposed two calibration methods to correct the pixel mismatch of the Timepix chip. Such correction is useful for applications requiring high spatial resolution at high energies, where mismatch between pixels increases.

It was proven that multi-bin computed tomography approach combined with photon-counting detectors is useful for material decomposition, especially in the pre-reconstruction space. RGB encoding can then be used for volumes of the various energy channels to form a colored volume in which different materials can be represented by different colors. In this work, we have succeeded in resolving the materials of an electronic device, a tracking device, using large-area Si photon counting detector. However, this approach can be extended to a wide range of objects, especially when performed with photon counting detectors with sensors of higher detection efficiency. Currently, large-area CdTe photon counting detectors are available, but their spectral performance is compromised due to polarization and charge sharing, so they are not a good choice for these applications despite their higher detection efficiency.

The second and most important part of this work was devoted to the development of an advanced imaging method, the DMCT (Data Fusion of Multipositional Computed Tomography) method, which has proven to be a useful tool for correcting the severe metal artifacts caused by highly attenuated metals. The application of such method opens the door to defect inspection for numerous applications that cannot be performed using the standard CT method.

In this work, it has been shown that DMCT can be effectively used to visualize low attenuation materials perturbed by the presence of metal artifacts. For this purpose, the sample can be scanned in different orientations, and the reconstructed volumes are then combined into a final reconstructed volume that suppress the perturbed data from all volumes. CT scans of the same object acquired at different orientations contain complementary information as far as metal artifacts are concerned. Therefore, combining these volumes results in a fused volume with corrected artifacts and lower noise.



The method has shown the importance of choosing the correct orientation of the object before the CT scan. The mounting position affects not only the position of the resulting artifacts, but also their intensity. Therefore, X-ray simulation is required to select the correct orientations that produce fewer artifacts.

The DFMCT method has been used for quality control of epoxy underfills for microelectronic devices that use ball grid arrays (BGA) as interconnects between ICs and PCBs. The epoxy underfill technique is widely used in microelectronics to increase the reliability of BGAs under mechanical and thermal stress. However, this technique is usually accompanied by defects, such as excess epoxy defects or partial filling. Therefore, a non-destructive method is needed to verify the success of the underfilling and to establish a correlation between the occurrence of the excess epoxy defects and the absence of underfilling between the spheres. Due to the high metal content in such components, photon-counting detectors are not a good choice, as high energy spectra are required to scan such samples.

The problem with scanning BGA samples is the creation of metal artifacts that affect the quality of the reconstruction. Therefore, we had to think about an approach that would allow us to compensate for the metal artifacts without compromising the quality of the reconstruction for the surrounding areas. We have shown that the classical methods for metal artifact correction are not suitable for correcting strong metal artifacts in such samples. We have discussed the advantages and disadvantages of metal artifact reduction algorithms, dual energy method CT and rotary computed laminography of classical CT setups. All the mentioned approaches did not help us to correct the artifacts and make the epoxy visible, while the DFMCT technique did. As such, the experimental results showed the possibility to overcome metal artifacts caused by high-attenuation materials, placing the X-ray technique as an option for defect detection in the microelectronic industry. In addition, a strong correlation was found between the underfilling process controlled by DFMCT and the optically observed epoxy on the sample surface, this provides us with tools for in-line manufacturing control. For other electronic devices, however, such a correlation needs to be confirmed using DFCMT.

With the DFMCT method, we have introduced a methodology for scanning complex objects that starts with an appropriate simulation to select the best alignments and then performs data fusion to the reconstructed data. Although the results were derived for a specific type of samples (BGA samples), the DFMCT method is optimal for most electronic devices that produces similar artifacts. Thus, the results and especially the methods have a more general validity, as they have been proven to solve problem related to industrial applications.

## **Author's publications**

### **Publications related to the topic of the thesis**

#### **Articles Published in Impacted Journals**

[1J] S. Hasn, M. Pichotka, K. Dusek, D. Vavrik, "Investigation of BGA Underfill Process Based on Multipositional Computed Tomography", *Journal of Instrumentation*, vol 17, no 06, p 06037, 2022, 10.1088/1748-0221/17/06/p06037.

[2J] S. Hasn, D. Vavrik, K. Dusek, M. Pichotka. "μ-CT investigation of tin whisker growth mechanisms", *Journal of Instrumentation*, vol. 15, no 02, p. 2043, 2020. DOI: 10.1088/1748-0221/15/02/c02043

[3J] S. Hasn, D. Vavrik, M. Pichotka, "improvement of Timepix energy resolution correcting threshold variations". *Journal of Instrumentation*, vol. 14, no 01, p. 1010, 2019. DOI: 10.1088/1748-0221/14/01/c01010

#### **Articles published on-line**

[4OL] S. Hasn, M. Pichotka, D. Vavrik. "Spectroscopic X-ray Tomography Based Hybrid Pixel Detectors", *NDT.net E-Journal*. Kirchwald: The e-Journal of Nondestructive Testing, www.ndt.net, 2018. ISSN 1435-4934.

### **Publications with author's contribution**

[5C] D. Vavrik, T. Fila, I. Kumpova, M. Vopalensky, S. Hasn, J. Zemlicka, "*Mobile CT scanner with XRF and K-edge imaging capability*", *NDT.net E-Journal*. Kirchwald: The e-Journal of Nondestructive Testing, www.ndt.net, 2018.

[6C] M. Pichotka, M. Weigt, S. Hasn, P. Meyer, D. Von Elverfeldt, M. Mix. "Hybrid-Pixel-Detektor Technologie für medizinische Bildgebung", *Nuklearmedizin*, vol. 59, 2020. DOI: 10.1055/s-0040-1708283.

[7C] M. Pichotka, K. Palma Alejandro, S. Hasn; J. Jakůbek, D. Vavřík, "Experimentally enhanced model-based deconvolution of propagation-based phase-contrast data". *Journal of Instrumentation*, vol. 11, P. 12037, 2016, DOI: 10.1088/1748-0221/11/12/c12037.

[8C] K.D. Palma, M. Pichotka, S. Hasn, C. Granja. "Table-top phase-contrast imaging employing photon-counting detectors towards mammographic applications", *Journal of Instrumentation*. 2017, vol. 12, DOI: 10.1088/1748-0221/12/02/c02032

## Citations

This Chapter includes publications which have cited the author's work according to Google Scholar excluding the self-citations.

[1\*] S, Procz et al., "X-ray and gamma imaging Medipix and Timepix detectors in medical reseadrch," *Radiation Measurements*, vol. 127, 2019.

This paper cites the journal paper [8C]

[2\*] A. Malliori et al., "Development of Physical Breast Phantoms for X-ray Imagung Employing 3D Printing Techniques," *The open Medical Imaging Journal*, vol. 12, 2020.

This paper cites the journal papers [7C] [8C]

[3\*] Navarrete Leónet , Carlos Felipe., Optimization of an X-ray system for fre-space propagation and single mask edge illumination phase contrast imaging, Uniandes, 2019.

This paper cites the journal paper [8C]

## References

- [1] "Center for Nondestructive evaluation," LOWA STATE UNIVERSITY, [Online]. Available: <https://www.nde-ed.org/>. [Accessed June 2022].
- [2] E. Harry E. Jr. Martz et al., X-ray Imaging, Fundamentals, Industrial Techniques, and Applications, USA: Taylor and Francis Group, 2017.
- [3] D. Vavrik, J. Jakubek, "Radiogram enhancement and linearization using the beam hardening correction method," *Nuclear Instruments and Methods in Physics Research Section A: Accelerators, Spectrometers, Detectors and Associated Equipment*, vol. 607, no. 1, 2009.
- [4] R. Ballabriga et al., "Photon Counting Detectors for X-ray Imaging with Emphasis on CT," *IEEE Transactions on Radiation and Plasma Medical Sciences*, vol. 5, no. 4, pp. 422-440, 2021.
- [5] S. Wood, D. Jena, Polarization Effects in Semiconductors, Springer New York, NY, 2008.
- [6] X. Llopert et al., "Timepix, a 65k programmable pixel readout chip for arrival time, energy and/or photon counting measurements," *Nuclear Instruments and Methods in Physics Research Section A: Accelerators, Spectrometers, Detectors and Associated Equipment*, vol. 581, no. 1-2, pp. 485-494, 2007.
- [7] G. A. Cervantes, "The basics of x-rays," in *Technical Fundamentals of Radiology and CT*, IOP Publishing, 2016, pp. 1-1 to 1-5.
- [8] G. Poludniowski et al., "SpekCalc: a program to calculate photon spectra from tungsten anode x-ray tubes," *Physics in Medicine and Biology*, vol. 54, no. 19, pp. 433-438, 2009.
- [9] A. Goel, D. Bell, "Photoelectric effect. Reference article, Radiopaedia.org.," June 2014. [Online]. Available: <https://doi.org/10.53347/rID-29684>. [Accessed May 2022].
- [10] Simone Carmignato et al., Industrial X-Ray Computed Tomography, Springer Cham, 2018.
- [11] "NIST,XCOM data base," [Online]. Available: <https://physics.nist.gov/PhysRefData/Xcom/html/xcom1.html>. [Accessed May 2022].
- [12] N. Rana et al., "Evaluation of external beam hardening filters on image quality of computed tomography and single photon emission computed tomography/computed tomography," *Journal of Medical Physics*, vol. 40, no. 4, pp. 198-206, 2015.

- [13] J. ZEMLIČKA, "X-Ray Radiography/Tomography combined with X-Ray Fluorescence Spectroscopy for Position Sensitive Elemental Analysis of studied objects," Ph.D Thesis, Czech Technical University in Prague, 2016.
- [14] E. J. Schioppa, "The color of X-rays, Spectral X-ray computed tomography using energy sensitive pixel detectors," Ph.D Thesis, National Institute for Subatomic Physics (Nikhef) in Amsterdam, 2014.
- [15] W. Orrison. William et al., "CHAPTER 3 - Clinical Brain Imaging: Computerized Axial Tomography and Magnetic Resonance Imaging," in *Functional Brain Imaging*, Mosby, 1995, pp. 97-144.
- [16] R. Popilock et al., "CT Artifact Recognition for the Nuclear Technologist," *Journal of Nuclear Medicine Technology*, vol. 36, no. 2, 2008.
- [17] J. Dudak, "Energy Sensitive X-ray Radiography and Tomography Optimized for Small Animal Imaging," Ph.D. Thesis, Czech Technical University in Prague, 2019.
- [18] B. Wiese, "The Effect of CaO on Magnesium and Magnesium Calcium Alloys," Ph.D. Thesis, Clausthal University of Technology, Germany, 2016.
- [19] R. Zhou R et al., "Study of the Microfocus X-Ray Tube Based on a Point-Like Target Used for Micro-Computed Tomography," *PLOS ONE*, vol. 11, no. 6, pp. 1-12, 2016.
- [20] J. Tous, J. Blazek, J. Zemlicka, J. Jakubek, "Evaluation of a YAG:CE scintillation crystal based CCD X-ray imaging detector with the Medipix2 detector," *JINST*, vol. 6, 2011.
- [21] J. Dudak, "Microtomography with photon counting detectors: improving the quality of tomographic reconstruction by voxel-space oversampling," *JINST*, vol. 12, 2018.
- [22] P Allé et al., "Comparison of CCD, CMOS and Hybrid Pixel x-ray detectors: detection principle and data quality," *Physica Scripta*, vol. 91, no. 6, 2016.
- [23] S. Schumacher et al., "Photon Counting and Energy Discriminating X-Ray Detectors - Benefits and Applications," in *19th World Conference on Non-Destructive Testing 2016*, Munich, 2016.
- [24] E. Grachev et al., "X-ray camera Based on CMOS Sensor," in *Mediterranean Conference on Embedded computing (MECO)*, Montenegro, 2019.
- [25] F. Ghelmansarai, "Flat panel detector technology," perkinElmer, 2009.
- [26] G. Zentai, "Comparision of CMOS and aSi flat panel images for X-ray imaging," in *IEEE, International Conference on Imaging System Techniques*, 2011.

- [27] "PerkinElmer, Dexela CMOS Flat Panel X-ray Detectors For NDT Applications," [Online]. Available: [https://resources.perkinelmer.com/lab-solutions/resources/docs/prd\\_cmos\\_ndt\\_pub\\_110\\_rev1.pdf](https://resources.perkinelmer.com/lab-solutions/resources/docs/prd_cmos_ndt_pub_110_rev1.pdf). [Accessed October 2020].
- [28] "VAREX IMAGING, Flat Panel Detectors," [Online]. Available: <https://www.vareximaging.com/solutions-security-industrial/>.
- [29] S. Miyao et al., "High -spatial-resolution X-ray Inspection by Pixelated Scintillator," *Transactions of The Japan Institute of Electronics Packaging*, vol. 11, 2018.
- [30] R. Ballabriga et al., "Review of hybrid pixel detector readout ASICS for spectroscopic X-ray imaging," *JINST*, vol. 11, 2016.
- [31] M. Platkeivč, „Signal Processing and Data Read-Out from Position sensitive Pixel Detectors,“ Ph.D Thesis, Czech Technical Univeristy In Prague, 2014.
- [32] A. Esquivel et al., "Photon-Counting Detector CT:Key Points Radiologist Should know," *Korean J Radiol*, p. 23:e57, 2022.
- [33] X. Llopart, "Medipix2: a 64-k pixel readout chip with 55  $\mu\text{m}$  square elements working in single photon counting mode," *Nucl. Instrum. Meth.*, vol. A 607.247: 5, 2009.
- [34] "CERN Acceleration science," medipix collaboration, [Online]. Available: <https://medipix.web.cern.ch/>. [Accessed January 2020].
- [35] D. Pennicard et al., "LAMBDA-large area Medipix3-Based Detector Array," *JINST*, vol. 7, 2012.
- [36] J. Jakubek et al., "Large area pixel detector WIDEPIX with full area sensitivity composed of 100 Timepix assemblies with edgeless sensors," *JINST*, vol. 9, 2014.
- [37] J. Jakubek, "Data processing and image reconstruction methods for pixel," *Nucl. Instr. Meth.*, Vols. A, 576, p. 23{234, 2007.
- [38] S. Hasn, D. Vavrik, M. Pichotka, "Improvement of Timepix energy resolution correcting threshold variations," *Journal of Instrumentation*, vol. 14, no. 01, p. 1010, 2019.
- [39] D. Turecek et al., "Pixelman: a multi-platform data acquisition and processing software package for Medipix2, Timepix and Medipix3 detectors," *JINST*, vol. 6, no. 01, 2011.
- [40] L. Tlustos et al., "Imaging properties of the Medipix2 system exploiting single and dual energy thresholds," in *IEEE Transactions on Nuclear Science*, 2006.

- [41] J. Jakubek, "Precise energy calibration of pixel detector working in time-over-threshold mode," *Nuclear Instruments and Methods in Physics Research Section A: Accelerators, Spectrometers, Detectors and Associated Equipment*, vol. 633, pp. s262-s266, 2011.
- [42] C. Ponchut, "Correction of the charge sharing in photon-counting pixel detector data," *Nuclear Instruments and Methods in Physics Research Section A: Accelerators, Spectrometers, Detectors and Associated Equipment*, vol. 591, no. 1, pp. 311-313, 2008.
- [43] H. Zeller et al., "Charge sharing between pixels in the spectral Medipix2 X-ray detector," in *24th International Conference Image and Vision Computing*, New Zealand, 2009.
- [44] S. Hasn, D. Vavrik, M. Pichotka, "Spectroscopic X-ray Tomography Based Hybrid Pixel Detectors," in *iCT2018*, Wels, Austria, 2018.
- [45] W. Zhou et al., "Comparison of a Photon-Counting-Detector CT with an Energy-Integrating-Detector CT for Temporal Bone Imaging: A Cadaveric Study," *AJNR*, vol. 39, no. 9, pp. 1733-1738, 2018.
- [46] M. Tortora et al., "Spectral Photon-Counting Computed Tomography: A Review on Technical Principles and Clinical Applications," *Journal of Imaging*, vol. 8, no. 112, 2022.
- [47] O. Grimm, M. Bednarzik, G. Birrer, V. Commichau, "Changes in detection characteristics of CdTe X-ray sensors by proton irradiation," *Nuclear Instruments and Methods in Physics Research Section A: Accelerators, Spectrometers, Detectors and Associated Equipment*, vol. 972, 2020.
- [48] "Apacer For Industrial, Underfill," [Online]. Available: <https://industrial.apacer.com/en-ww/Technology/Underfill->. [Accessed February 2022].
- [49] "Nordson," ELECTRONIC SOLUTIONS, [Online]. Available: <https://www.nordson.com/en/divisions/asymtek/your-process/fluid-types/underfill>. [Accessed 4 2022].
- [50] J. Perraud et al., "Control of the Underfill of Surface Mount Assemblies by Non-Destructive Techniques," in *IPC APEX EXPO Conference*, 2015.
- [51] S. Canumalla, P. Viswanadham, "Microelectronic Failure Analysis 5th Edition," in *Board level Failure Mechanisms and Analysis in Handheld Electronic Products*, ASM International, 2011, p. 22:32.
- [52] P. Aryan et. al., "An Overview of Non-Destructive Testing Methods for Integrated Circuit Packaging Inspection," *Sensors (Basel)*, vol. 18, no. 7, 2018.

- [53] R. Ghaffarian, "Defect Features Detected by Acoustic Emission for Flip-Chip CGA / FCBGA / PBGA / FPBGA Packages and Assemblies," in *Materials Science*, 2016.
- [54] "VOLUME GRAPHICS," [Online]. Available: <https://www.volumegraphics.com/en/products/vgsm.html>. [Accessed May 2022].
- [55] L. Gjestebj et al, "Metal Artifact Reduction in CT: Where Are We After Four Decades?," *IEEE Access*, vol. 4, p. 5826:5849, 2016.
- [56] M. Katsura et al., "Current and Novel Techniques for Metal Artifact Reduction at CT: Practical Guide for Radiologists," *RadioGraphics*, vol. 38, no. 2, pp. 450-461, 2018.
- [57] Y. B. Chang, D. Xu and A. A. Zamyatin, "Metal artifact reduction algorithm for single energy and dual energy CT scans," in *IEEE Nuclear Science Symposium and Medical Imaging Conference Record (NSS/MIC)*, 2012.
- [58] M. Axente et al., "Clinical evaluation of the iterative metal artifact reduction algorithm for CT simulation in radiotherapy," *Med Phys*, vol. 42, no. 3, 2015.
- [59] A.J. Vellarackal , A.H. Kaim, "Metal artefact reduction of different alloys with dual energy computed tomography (DECT)," *Sci Rep*, vol. 11, 2021.
- [60] J. Guhathakurta et al., "Reducing Computed Tomography Reconstruction and Beam Hardening Artifacts by Data Fusion," in *Digital Industrial Radiology and Computed Tomography (DIR 2015)*, Ghent, 2015.
- [61] H. Ballhausen et al., "Post-processing sets of tilted CT volumes as a method for metal artifact reduction," *Radiat Oncol*, vol. 9, no. 114, 2014.
- [62] J. Y. Vaishnav ET AL., "CT metal artifact reduction algorithms: Toward a framework for objective performance assessment," *MEDICAL PHYSICS*, vol. 47, no. 8, 2020.
- [63] S. Xie, Z. Song,, "Metal artifact correction in head computed tomography based on a homographic adaptation convolution neural network," *Multimed Tools Appl*, vol. 81, pp. 13045-13064, 2022.
- [64] E. Meyer et al., "Normalized metal artifact reduction (NMAR) in computed tomography," *Medical physics*, vol. 37, pp. 5482-5493, 2010.
- [65] Q. Wang et al., "A novel metal artifact reducing method for cone-beam CT based on three approximately orthogonal projections," *Phys Med Biol*, vol. 58, pp. 9155-9158, 2012.



- [66] P. Lim et al., "Evaluation of dual energy CT and iterative metal artefact reduction (iMAR) for artefact reduction in radiation therapy," *Australas Phys Eng Sci Med*, vol. 42, no. 4, pp. 1025-1032, 2019.
- [67] D. Vavrik et al., "Dual energy CT inspection of a carbon fibre reinforced plastic composite combined with metal components," *Case Studies in Nondestructive Testing and Evaluation*, vol. 6, pp. 47-55, 2016.
- [68] M. Mais, "Computed Laminography for X-ray Inspection of Lightweight Constructions," in *2nd Int. Symposium on NDT in Aerospace*, Hamburg, Germany, 2011.
- [69] NS. O'Brien et al., "Recent Advances in X-ray Cone-beam Computed Laminography," *J Xray Sci Technol*, vol. 24, no. 5, pp. 691-707, 2016.
- [70] Jian Fu et al., "Large field of view computed laminography with the asymmetric rotational scanning geometry," *Science China Technological Sciences*, vol. 53, pp. 2261-2271, 2010.
- [71] S L Fisher et al., "Laminography in the lab: imaging planar objects using a conventional x-ray CT scanner," *Measurement Science and Technology*, vol. 30, 2019.
- [72] Y. Zhao et al., "Edge Information Diffusion-Based Reconstruction for Cone Beam Computed Laminography," vol. 27, pp. 4663-4675, 2018.
- [73] "aRTist- Analytical RT Inspection Simulation Tool," BAM, [Online]. Available: <http://artist.bam.de/>. [Accessed March 2022].
- [74] S. Hasn, M. Pichotka, K. Dusek, D. Vavrik, "Investigation of BGA Underfill Process Based on Multipositional Computed Tomography," *Journal of Instrumentation*, vol. 17, no. 06, p. 06037, 2022.
- [75] C. Beelon et al., "Radiographic Simulator aRTist: Version 2," in *18th World Conference on Nondestructive Testing*, Durban, South Africa, 2012.
- [76] Ch. Gollwitzer et al., "On POD Estimations with Radiographic Simulator aRTist," in *International Symposium on Digital Industrial Radiology and Computed Tomography*, berlin, Germany, 2011.
- [77] Ch. Heinzl et al., "Fast Estimation of Optimal Specimen Placements in 3D X-ray Computed Tomography," in *International Symposium on Digital Industrial Radiology and Computed Tomography*, 2011.
- [78] H. Villarraga-Gómez, "Studies of Dimensional Metrology with X-ray CAT Scan," Ph.D Thesis, University of North Carolina, 2018.

[79] S. Ehn, "Photon-Counting Hybrid-Pixel Detectors For Spectral X-ray Imaging Applications,"  
PH.D Thesis, Technical University of Munich, 2017.